

Microstructure and coercivity relationship of  
hot-deformed Nd-Fe-B anisotropic magnets

Jun LIU

June 2015



Microstructure and coercivity relationship of  
hot-deformed Nd-Fe-B anisotropic magnets

Jun LIU

Doctoral Program in Materials Science and Engineering

Submitted to the Graduate School of

Pure and Applied Sciences

in Partial Fulfillment of the Requirements

for the Degree of Doctor of Philosophy in Engineering

at the

University of Tsukuba



# Table of Contents

<b>Chapter 1. Introduction</b> .....	1
1.1 Background .....	1
1.2 The development of the permanent magnets.....	3
1.3 Crystal structure and phases of Nd-Fe-B magnets.....	5
1.4 Methods to manufacture Nd-Fe-B permanent magnets.....	7
1.4.1 Sintered magnets .....	8
1.4.2 Hot-deformed Nd-Fe-B magnets.....	9
1.4.3 HDDR processed Nd-Fe-B magnets.....	10
1.4.4 Nd-Fe-B films .....	12
1.5 Coercivity mechanism of Nd-Fe-B magnets .....	12
1.5.1 Magnetization reversal.....	13
1.5.2 Micromagnetic model.....	14
1.5.3 Nucleation and pinning.....	14
1.5.4 Angular dependence of coercivity.....	16
1.5.5 Temperature dependence of coercivity.....	18
1.5.6 Global model.....	18
1.6 Strategies to improve the coercivity of Nd-Fe-B magnets.....	19
1.6.1 Additives.....	21
1.6.2 Grain boundary diffusion process (GBDP).....	21
1.6.3 Grain size.....	22
1.7 Motivation of this work and outline of this thesis.....	24
Reference .....	25
<b>Chapter 2. Experimental</b> .....	33
2.1 Scanning electron microscopy (SEM) .....	33
2.2 Transmission electron microscope (TEM).....	34
2.2.1 Bright field (BF) image .....	34

2.2.2 High resolution transmission electron microscopy (HRTEM).....	35
2.2.3 Electron energy loss spectroscopy (EELS).....	35
2.2.4 Lorentz TEM microscopy in Fresnel mode .....	35
2.3 Laser assisted three dimensional atom probe (3DAP).....	36
2.3.1 Atom probe specimen preparation .....	36
2.3.2 Laser assisted 3D atom probe .....	40
Reference .....	42

<b>Chapter 3. The effect of Nd content on the microstructure and coercivity of hot-deformed Nd-Fe-B magnet.....</b>	<b>43</b>
3.1 Introduction.....	43
3.2 Experiment .....	44
3.3 Results .....	45
3.4 Discussion.....	61
3.5 Summary .....	63
Reference .....	64

<b>Chapter 4. The grain size dependence of coercivity of hot-deformed Nd-Fe-B magnets .....</b>	<b>66</b>
4.1 Introduction.....	66
4.2 Experiment .....	67
4.3 Results .....	68
4.3.1 Magnetization behavior .....	68
4.3.2 Microstructure.....	69
4.3.3 Micromagnetic simulations .....	75
4.4 Discussion.....	78
4.5 Summary .....	81
Reference .....	83

<b>Chapter 5. The microstructure evolution of hot-deformed Nd-Fe-B magnets</b>	<b>85</b>
5.1 Introduction.....	85
5.2 Experiment .....	86
5.3 Results and Discussion.....	86
5.4 Summary .....	92
Reference .....	94
<b>Chapter 6. Microstructure study of Nd-Fe-B thin films with different levels of coercivity</b>	<b>95</b>
6.1 Introduction.....	95
6.2 Experiment .....	96
6.3 Results.....	97
6.4 Discussion.....	101
6.5 Summary .....	103
6.6 Extension.....	103
Reference .....	106
<b>Chapter 7. Summary of the thesis</b> .....	<b>107</b>
<b>Publications</b> .....	<b>108</b>
<b>Acknowledgments</b> .....	<b>109</b>

# Chapter 1. Introduction

## 1.1 Background

The civilizations and modernizations of the human society have caused a series of serious influences on the nature, in particular the depletion of the nonrenewable fossil fuels and the severe destruction of the natural environment. Global concerns about the energy conservation and the emission reduction have stimulated substantial researches on the development of new energy concepts to replace the dominant fossil fuels and new technology to convert energy more efficiently and environment-friendly.

From last century, the development of the human society was on the wheels and the driving force came from the electric power. According to a report on the International Energy Statistics from the U.S. Energy Information Administration, the world electric power generation was 21.5 trillion kilowatt hour in 2012, which was almost double compared with the value two decade ago, that is, 11.6 trillion kilowatt hour [1]. The huge cardinal number of the world electric power generation and its rapid growth has impelled researchers and engineers to design the motors, transformers, and generators innovatively in order to convert energy more efficiently. Minimization and lightweight of the motors, transformers, and generators with the required performance are appealing directions of device development, which is in the same trend with the development of the permanent magnets in the last century as shown in Figure 1.1 [2]. A good example is the application of the Nd-Fe-B magnets in the voice coil motor of the hard disk drive, not only minimizing the device size and improving the performance, but also reducing the cost. Another example is that the energy-efficient air conditioners with the inserted Nd-Fe-B permanent magnet compressors are approximately 30% better than that of induction motors [3]. On the other hand, if we have a look at the energy structure, it is astonished to find out that around 80% of energy supply is still from fossil fuels like oils, coals, and gases, even though the human society has already stepped into new century. To sustainable development, clean and renewable energy sources such as solar energies, winds, geothermal energies, etc. are received more attentions nowadays. The wind power is one of the fast growing renewable energy. The application of the Nd-Fe-B permanent magnet generators (PMGs) to the wind turbines is a relatively new and growing trend in the industry. Without gearboxes, the PMGs can be flexibly designed and easily maintained. Thanks to the magnetic field around the conducting coils created by the powerful Nd-Fe-B magnets, the PMGs are able to produce powers even at a single revolution per minute and the auxiliary consumption is drastically reduced [4-5]. The advantages of low cost, easy maintenance, reliable power output and high efficiency of the PMGs would make the wind power rapid

expansion in the near future. Another energy-related critical issue which has a close relationship with our dairy life is the vehicles. The electric vehicles (EV) and hybrid electric vehicles (HEV) are easy to see on the road nowadays and their market share has increased to 3% according to the statistics from U.S. Department of Energy in 2012 [6]. The motor of the HEV uses ~1.3 kg of the (Nd,Dy)-Fe-B permanent magnets with the benefit of small size, high efficiency, light weight, and high torque [7]. The amazing thing of HEV is that it can recapture significant amount of energy during braking by converting the kinetic energy into electricity while braking is normally wasted as heat in the internal combustion engine vehicles. The arrival of EV and HEV will infuse new vitality into the automotive industry. So far, we have seen the great contributions from the permanent magnets, especially Nd-Fe-B magnets, to reducing the volume and weight of the devices as well as improving the energy conversion efficient. Now let's talk about the Nd-Fe-B magnets on the aspects of the development, microstructure, manufacture, magnetic properties and limitations in the following parts.

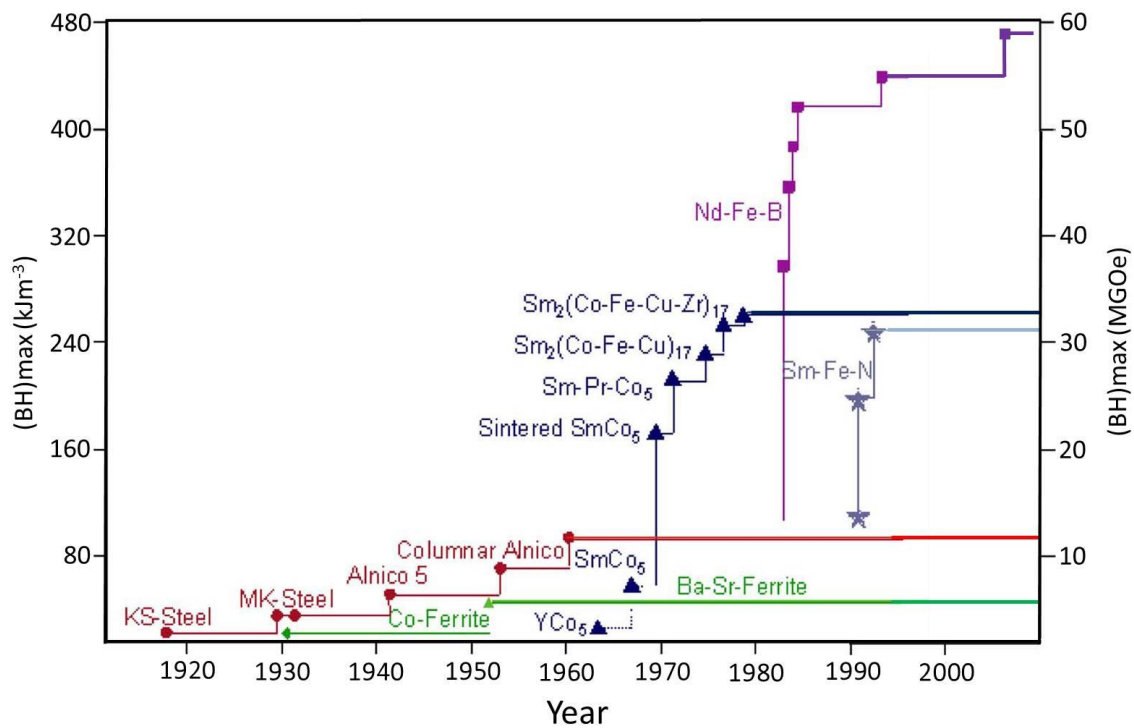


Figure 1.1 Improvement in the maximum energy product at room temperature of the permanent magnets in the 20th century and the presentation of different types of materials with comparable energy density [2].

## 1.2 The development of the permanent magnets

A permanent magnet is a magnetized object and creates its own persistent magnetic field. Last century witnessed to the leaps and bounds of the permanent magnets. The maximum energy product ((BH)max) is a commonly used term to describe the maximum amount of the magnetic energy stored in a magnet. In a hysteresis loop with the magnetization remains saturated fully into the second quadrant, the BH can be deduced from the following formula.

$$BH = \mu_0(H + M)H, \quad (1.1)$$

$$H = -NM, \quad (1.2)$$

$$\text{So, } BH = \mu_0(1 - N)NM_s^2, \quad (1.3)$$

where N is the demagnetizing factor.  $N = 1/2$  gives the maximum value of BH.

$$(BH)_{\text{max}} = 1/4\mu_0M_s^2, \quad (1.4)$$

To achieve the maximum energy product, the minimum requirement is that the coercivity should be larger than half of the magnetization, that is,  $H_c > 1/2M_s$ . In the last century the value of (BH)max almost doubled every 14 years with the invention of the innovated magnetic materials as shown in Figure 1.1 [2].

In the history of the permanent magnets, the discovery of the MK Steel (Fe-Al-Ni) which was later improved and became Alnico (Fe-Al-Ni-Co) in U.S. was the first improvement over steels, and the composition and processing of the Alnico alloys were developed and eventually the (BH)max was improved to  $\sim 80 \text{ kJm}^{-3}$ . Alnico alloys have a large spontaneous magnetization of  $\sim 1.1 \text{ MA m}^{-1}$  as well as a high Curie temperature of  $\sim 850 \text{ }^\circ\text{C}$  and consequently can be used for high temperature applications. However, the low intrinsic coercivity deriving from the shape anisotropy generated by a fine needle-shaped ferromagnetic phase in a nonmagnetic matrix limited the shape of magnets in the form of bar or horseshoes.

The improvement in the magnetic property of ferrite in the 1950s broke the shape barrier and henceforth the magnets could be desired in any shape. Till now, ferrite still occupies the largest market share of the permanent magnets due to the advantage of extremely low cost. Unfortunately, the low remanence led to a low (BH)max of  $\sim 40 \text{ kJm}^{-3}$ .

The advent of the rare earth (RE)-transition metal (TM) permanent magnet drastically improved the maximum energy product. The exceptional magnetic properties of RE-TM permanent magnets results from the exchange interactions between 4f electrons of RE elements and 3d electrons of TM elements. According to the Hund's rules, the incomplete filling of 4f shell can contain up to seven unpaired electrons with aligned spins. The electrons in the 4f orbitals are strongly localized and both spin and orbital motions contribute to the magnetic moment, which leads to the uniaxial magnetocrystalline

anisotropy. The 3d TM element provides high magnetization and high Curie temperature. Therefore, the compound of 4f RE element and 3d TM element possesses excellent intrinsic properties [8]. Three families of rare earth permanent magnets are currently in commercial production. They are  $\text{SmCo}_5$ ,  $\text{Sm}_2\text{Co}_{17}$  and  $\text{Nd}_2\text{Fe}_{14}\text{B}$ .

The discovery of  $\text{YCo}_5$  which had the largest magnetic anisotropy constant then triggered researchers' great interest in the rare earth permanent magnets in 1966 [9]. The extension of this research led to the emergence of the first generation of rare earth permanent magnets  $\text{SmCo}_5$ , which shows a maximum energy product of up to  $\sim 160 \text{ kJm}^{-3}$  and a high coercivity to resist thermal and field demagnetization and a high Curie temperature as well as excellent corrosion resistance [10-13].

$\text{Sm}_2\text{Co}_{17}$  type rare earth permanent magnets were derived from  $\text{SmCo}_5$  and developed in the 1970s. The substitution of Co for Sm atoms gives a higher saturation magnetization as well as a higher Curie temperature at the cost of anisotropy field when compared to  $\text{SmCo}_5$  type permanent magnets. Substantial efforts have been made to increase the coercive field by optimizing the microstructure. By partial substitution Co by Fe, Cu, and Zr and appropriate aging treatment, the commercial  $\text{Sm}_2\text{Co}_{17}$  permanent magnets usually have a cellular microstructure where the high magnetization  $\text{Sm}_2\text{Co}_{17}$  cell phase was surrounded by the high magnetic hardness  $\text{SmCo}_5$  boundary phase [14-15]. Iron has been used to improve the saturation magnetization of the  $\text{Sm}_2\text{Co}_{17}$  magnets. Cu improves the coercivity by a large domain wall energy gradient across the cell boundaries [14,16]. Zr enriches a platelet phase, also called Z phase, which is thought to stabilize the cellular structure and provides diffusion paths for Cu, Fe and Co [17]. The maximum energy product of  $\text{Sm}(\text{Co,Fe,Cu,Zr})_{7.0-8.5}$  permanent magnets was increased to  $\sim 240 \text{ kJm}^{-3}$ , which led to the commercial success of the second generation of rare earth magnets [18]. The  $\text{Sm}_2\text{Co}_{17}$  type permanent magnets are widely used in the microwave tubes, gyroscopes and accelerometers where high-energy density magnets with magnetic fields stable over a variety of environmental conditions and wide temperature ranges are required [13].

However, the drawbacks of SmCo-based permanent magnets were the complex heat treatment procedure and the high cost of Sm and Co, which impeded the widespread adoption of them. Considerable research was done from the late 1970s to early 1980s to obtain a better rare earth permanent magnet by replacing Sm with other cheaper elements, such as Nd and Pr, and replacing Co with Fe, and adding B to stabilize the R-Fe alloys [19-21]. These efforts eventually led to the discovery of third generation of rare earth permanent magnets. The researchers from two different groups developed Nd-Fe-B magnets independently. Croat et al produced nanocrystalline Nd-Fe-B magnets named as MAGNEQUENCH by using the melt spinning technique [22-23], and Sagawa et al used powder metallurgy method to obtain sintered Nd-Fe-B magnets named as NEOMAX [24]. The main component

of Nd-Fe-B magnets is Fe, which is very cheap with a large ferromagnetic moment. A small amount of a relative abundant light rare earth element Nd provides much of anisotropy. Occupying just 2% of the volume of the unit cell, B effectively stabilizes the tetragonal crystal structure. Intensive investigations were attracted on the development of Nd-Fe-B magnets, eventually leading to realize the commercial products with  $(BH)_{\max}$  over  $\sim 450 \text{ kJm}^{-3}$ , and a record value of  $\sim 480 \text{ kJm}^{-3}$  for a laboratory magnets [25].

### 1.3 Crystal structure and phases of Nd-Fe-B magnets

The  $\text{Nd}_2\text{Fe}_{14}\text{B}$  phase has a tetragonal crystal structure belonging to the space group  $P4_2/mnm$  with crystal parameter  $a = 0.88 \text{ nm}$  and  $c = 1.21 \text{ nm}$  as shown in Figure 1.2 [8,26]. This  $\text{Nd}_2\text{Fe}_{14}\text{B}$  compound shows a [001] easy-axis anisotropy at room temperature.

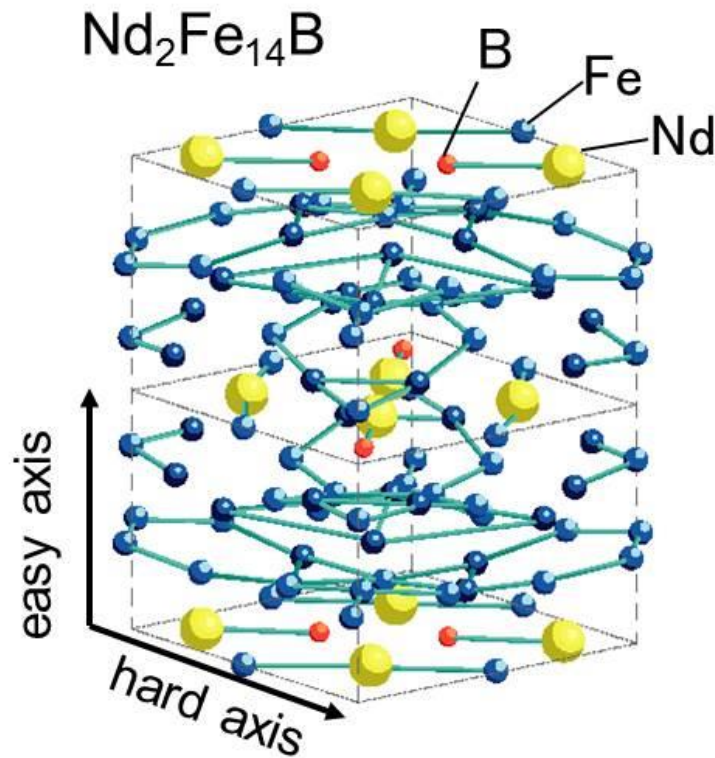


Figure 1.2 Crystal structure of the  $\text{Nd}_2\text{Fe}_{14}\text{B}$  phase (tetragonal,  $P4_2/mnm$ ) [8].

A typical microstructure of Nd-Fe-B magnets consists of hard magnetic  $\text{Nd}_2\text{Fe}_{14}\text{B}$  grains separated by nonmagnetic Nd-rich grain boundary phases (GB) as shown in Figure 1.3. The  $\text{Nd}_2\text{Fe}_{14}\text{B}$  phase has a high anisotropy field of  $\sim 7.5$  T and saturation magnetization of  $\sim 1.6$  T [27-28]. Even though it has excellent intrinsic properties, the coercive field of the Nd-Fe-B magnets is only less than 15% of the anisotropy field of the  $\text{Nd}_2\text{Fe}_{14}\text{B}$  phase. This is because that the coercivity is not only dependent on the intrinsic properties, but also sensitive to the microstructural features, such as GB, secondary phases, and grain size. The coercivity mechanism of the Nd-Fe-B permanent magnets will be given in detail in Chapter 1.5. The starting material to produce the Nd-Fe-B magnets usually has excess of Nd compared to the stoichiometry of the  $\text{Nd}_2\text{Fe}_{14}\text{B}$  phase. This is because the Nd becomes liquid at the temperature above  $650$  °C, which improves the densification of the magnets during the processing. In addition, the presence of the liquid Nd-rich phase during the hot-deformation process is essential to align the crystallographic c-axis texture of the  $\text{Nd}_2\text{Fe}_{14}\text{B}$  grains parallel to the pressing direction for the hot-deformed Nd-Fe-B magnets. The liquid Nd forms Nd-rich phase at the triple junctions and along the GBs after cooling, which isolate the  $\text{Nd}_2\text{Fe}_{14}\text{B}$  grains and result in an increased coercivity. However, Nd-rich phase is very easy to oxidize. There are several different types of Nd-rich phases existed in the Nd-Fe-B sintered magnets. The crystal structure of the Nd-rich phase closely relates to the O content. With the increase of O content, the crystal structure of the Nd-rich phase changes from metallic, close-packed double hexagonal (dhcp), face-centered cubic (fcc), to close-packed hexagonal (hcp) [29-30]. It is known that a certain proportion of the metallic Nd-rich phase is beneficial to the formation of the uniform GBs. Therefore, the careful control of the Nd-oxide phases during the processing is important to achieve a high coercivity. The Nd-rich GB phase is amorphous when the thickness is less than 1 nm and crystalline at larger thickness [31]. The optimized heat treatment on the sintered Nd-Fe-B magnets is known to introduce smooth and continuous GB layers by dissolving the small irregularities at the interface and consequently lead to a high coercivity value [32].

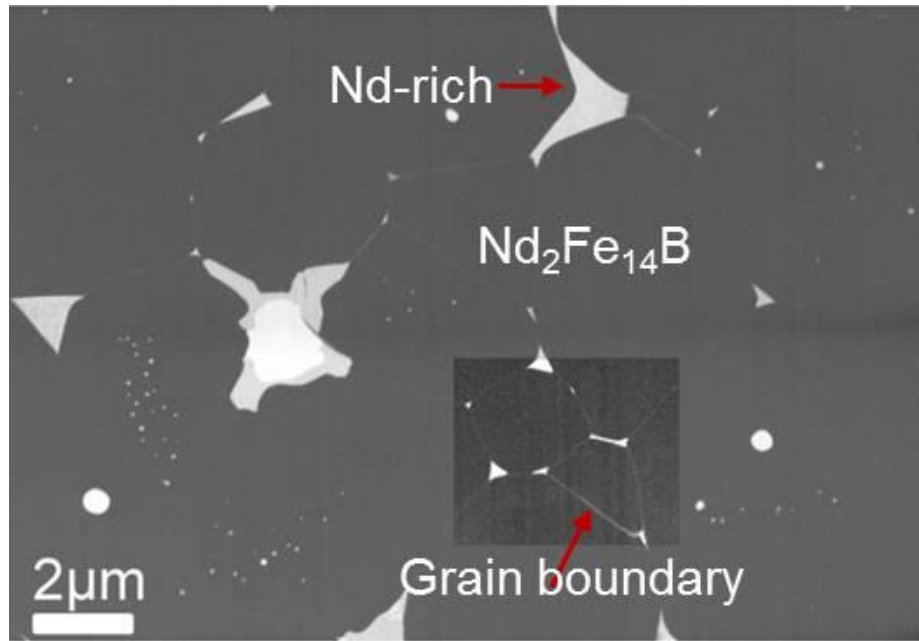


Figure 1.3 Typical microstructure of the sintered Nd-Fe-B magnets.

Generally, the microstructure of the Nd-Fe-B magnets strongly depends on the processing routes. For example, the B-rich phase  $\text{Nd}_{1+x}\text{Fe}_4\text{B}_4$  ( $P4_2/ncm$ ,  $tP328$ ,  $a = 0.7117\text{nm}$ ,  $c = 3.507\text{ nm}$ ) forms in the sintered Nd-Fe-B magnets and it seriously degrades the hard magnetic properties by causing strong internal demagnetizing fields and reducing the remanence [8]. Different from sintered ones, the Nd-rich phases at the triple junctions and GBs are free of Oxygen in the hot-deformed Nd-Fe-B magnets [33-35].

#### 1.4 Methods to manufacture Nd-Fe-B permanent magnets

Two well-established methods are commercially used to manufacture the Nd-Fe-B permanent magnets: the powder metallurgy and the rapid solidification by melt-spinning. The former technique is used to produce fully dense anisotropic sintered Nd-Fe-B magnets, while the latter one is employed to obtain isotropic Nd-Fe-B flakes, which are used to fabricate the bonded Nd-Fe-B magnets by blending the flakes with resins, or used as the precursor to prepare full dense anisotropic hot-deformed Nd-Fe-B magnets by introducing hot-pressed and subsequently hot-deformed process.

### 1.4.1 Sintered magnets

Most of the Nd-Fe-B magnets are produced by powder metallurgy sintering method. In industry, the starting Nd-Fe-B ingots slightly rich in Nd and poor in Fe are prepared during the strip casting (SC) process, which allows one to move the composition near to the stoichiometry without precipitations of Fe phase. In the following coarse grinding process of Nd-Fe-B ingots, a hydrogen decrepitation (HD) is used to reduce the alloys into friable powders and the HD method is easier than pulverizing the ingots mechanically [36]. Cracks are intentionally introduced between the Nd-rich phase and the  $\text{Nd}_2\text{Fe}_{14}\text{B}$  grains during HD process. A jet milling process has been widely introduced to fabricate the fine powders. It has two advantages: one aspect is that it can grind the friable powders to  $3 \sim 5 \mu\text{m}$  with a narrow powder size range; the other is that by compressing inert gas and feeding the materials into the vortex, the jet-milled powders are free from contamination and oxidation, which would deteriorate the magnetic properties of the powders. The alignment of the magnetic particles is achieved in an external pulsed magnetic field prior to the sintering process at a temperature around  $1100 \text{ }^\circ\text{C}$  for the densification. Thereafter, a post-annealing at the temperature around  $500 \sim 600 \text{ }^\circ\text{C}$  for 1 hour is essential to optimize the microstructure and magnetic properties of the magnets. The schematic illustration of the sintering process of the Nd-Fe-B magnets is shown in Figure 1.4 [37].

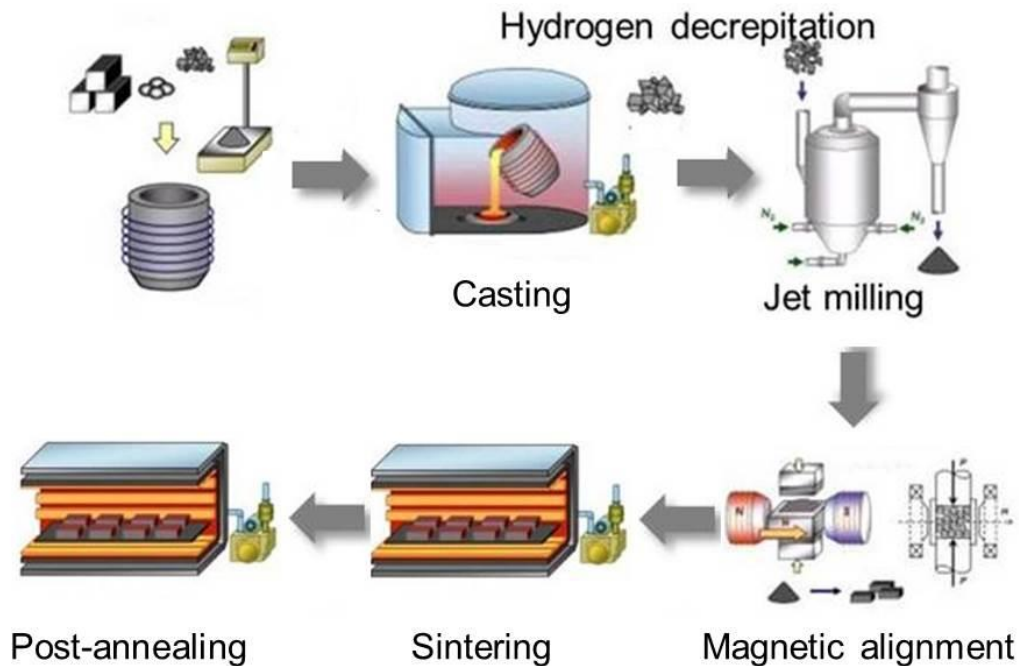


Figure 1.4 The schematic illustration of the sintering process of Nd-Fe-B magnets [37].

The Nd-rich phase which becomes a liquid phase when the temperature is above 650 °C is very important to achieve the full densification of the magnets during the sintering process. However, this phase is also highly reactive with oxygen and the formation of the Nd-oxide phase deteriorates the magnetic property seriously. Recently, a helium jet milling method to reduce the powder size to less than 2 μm and an innovative magnetic powder compaction method called pressless process (PLP) were developed to simplify the manufacture and decrease the oxygen absorption in the powders [38-39]. The advantage of small-sized grains as well as significant reduced Nd-oxide phases leads to a remarkable coercivity of ~2.0 T and (BH)<sub>max</sub> of ~400 kJm<sup>-3</sup>.

#### 1.4.2 Hot-deformed Nd-Fe-B magnets

The hot-deformation process of the rapidly solidified Nd-Fe-B ribbons developed by Lee et al. is a well-known method to produce anisotropic magnets with an ultrafine grain size of nearly a single domain size of ~250 nm [40-42]. The hot-deformed process is shown schematically in Figure 1.5. The process is composed of four steps: melt spinning, cold pressing, hot pressing, and hot deformation. The starting alloy with a Nd rich composition is melt and chilled onto a fast rotating Cu wheel surface in an inert atmosphere, so that nanocrystalline or amorphous ribbons with size around 150 μm can be obtained. Inside of the ribbon, there are ultrafine crystal grains around 50 nm, and easy axes of them are randomly distributed. So the powders of such nanocrystalline ribbons have isotropic structures. This microstructure effectively suppresses the oxidation of the metallic Nd-rich phase during the hot-deformation process. Then the powders are cold-pressed with height reduction of ~85% under modest pressures of 600-700 MPa [40]. Fully dense isotropic precursors are produced by hot pressing in vacuum at the temperature of around 750~800 °C and 150 MPa. A slight alignment of the easy axes ~10% was introduced by the hot-pressing step. During hot-deformation procedure at about 750~850 °C, the equiaxed grains can be modified to anisotropic plate-like structures. The easy axes of the grains are aligned parallel to the pressing direction, due to the combination of the grain boundary sliding and anisotropic grain growth [43]. So, the remanent magnetization is significantly improved. The anisotropic hot-deformed Nd-Fe-B magnets show magnetic properties of 1.15-1.4 T for the remanence, 1.2-1.8 T for the coercivity, and 250-340 kJm<sup>-3</sup> for the maximum energy density [44].

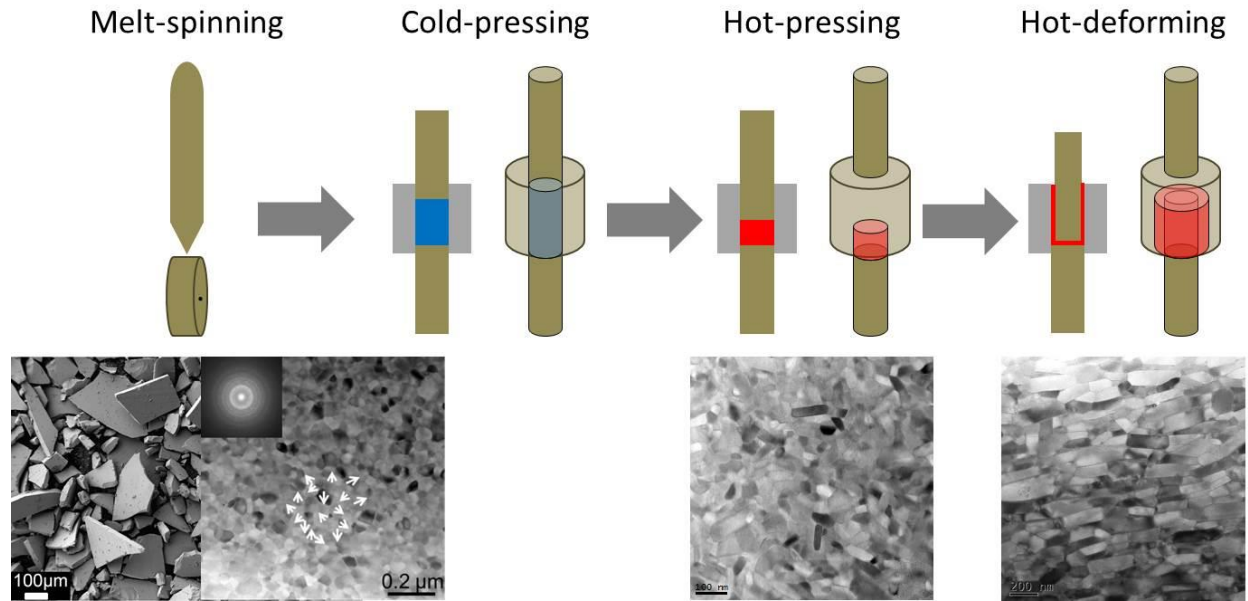


Figure 1.5 The schematic illustration of the hot-deformation of Nd-Fe-B magnets.

It is known that the presence of the liquid Nd-rich intergranular phase during the hot-deformation process is essential for the formation of the crystallographic c-axis texture. There have been many reports on the evolution process of the c-axis texture by hot-deformation. Grünberger et al. proposed a model of interface-controlled solution-precipitation creep to explain the formation of the texture [45]. Mishra et al. reported that the alignment of  $\text{Nd}_2\text{Fe}_{14}\text{B}$  grains results from a combination of plastic deformation, grain boundary migration, and grain boundary sliding [43,46]. In addition, the Nd-rich intergranular phase also makes an important role in the coercivity of hot-deformed Nd-Fe-B magnets. The Nd-rich intergranular phase was reported to work as pinning sites against magnetic domain wall motion [47-48]. Lewis et al. found high amount of Fe existing at the intergranular phase and suggested that the dominant coercivity mechanism is the nucleation of reversed domains in the Fe-rich intergranular region of reduced anisotropy [49-50].

### 1.4.3 HDDR processed Nd-Fe-B magnets

The hydrogenation disproportionation desorption recombination (HDDR) process developed by Takeshita and Nakayama and McGuinness is another method to produce high coercivity Nd-Fe-B magnets with single domain sized  $\text{Nd}_2\text{Fe}_{14}\text{B}$  grains [51-52]. The schematic illustration of HDDR process and HDDR reactions are shown in Figure 1.6 and Equation (1.5), respectively [42]. The  $\text{Nd}_2\text{Fe}_{14}\text{B}$  phase disproportionates into  $\text{NdH}_2$ , Fe, and  $\text{Fe}_2\text{B}$  when heat-treated at  $\sim 750\text{-}900$  °C in hydrogen. Subsequent

heat treatment in vacuum removes hydrogen from  $\text{NdH}_2$  and the remained Nd, Fe and  $\text{Fe}_2\text{B}$  recombine into very fine  $\text{Nd}_2\text{Fe}_{14}\text{B}$  grains. The alignment of  $\text{Nd}_2\text{Fe}_{14}\text{B}$  grains in the HDDR-processed powders is generated by some additives or controlling the temperature and hydrogen pressure during HDDR process [51,53-54]. It is also reported that the intermediate phase  $\text{Fe}_3\text{B}$  formed during HD process shows an orientation relationship with initial  $\text{Nd}_2\text{Fe}_{14}\text{B}$  phase and later serves as memory sites for the recombined  $\text{Nd}_2\text{Fe}_{14}\text{B}$  phase during the DR process [55-56]. Since the  $\text{Fe}_3\text{B}$  is a metastable phase during the processing, recently studies suggest that the  $\text{Fe}_2\text{B}$  phase acts as the texture memory sites [57-62]. The HDDR powders can be used to produce bonded magnet by mixing with resin and a  $(\text{BH})_{\text{max}}$  value of  $\sim 200 \text{ kJm}^{-3}$  can be achieved. Recently, a spark plasma sintering method was employed to consolidate HDDR magnet with  $(\text{BH})_{\text{max}}$  of  $\sim 210 \text{ kJm}^{-3}$  [63]. To improve the coercivity, a so-called grain boundary diffusion process was proposed and employed on the HDDR-processed magnets [64-65]. When the mixture of HDDR powders and the Nd-transmission metal eutectic alloy was annealed at  $\sim 700 \text{ }^\circ\text{C}$ , the alloys melt and diffuse into the powders through the GBs, resulting in a better isolation of the  $\text{Nd}_2\text{Fe}_{14}\text{B}$  grains, and consequently the coercivity was increased to  $\sim 2.0 \text{ T}$ .

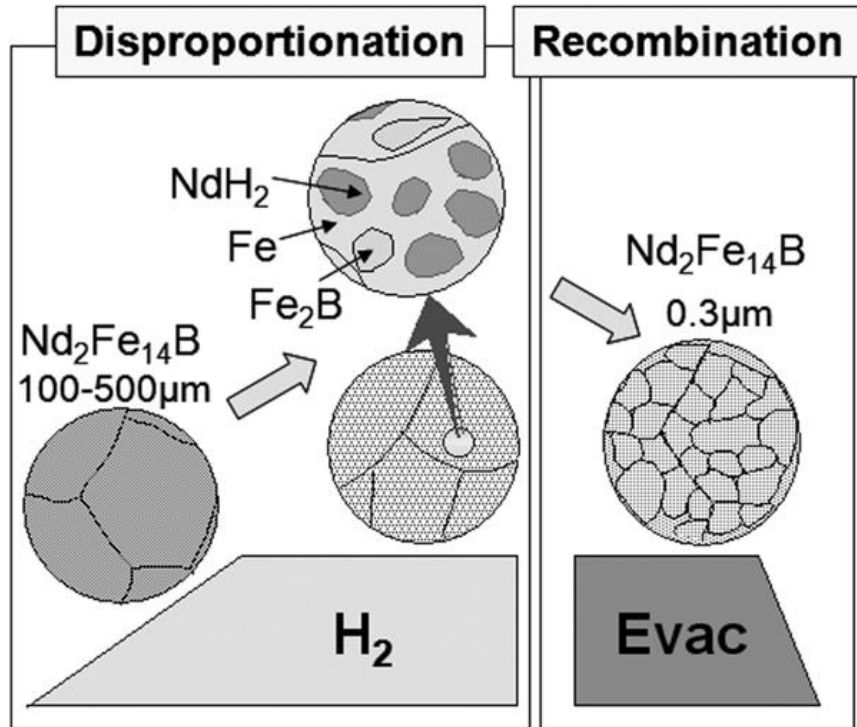
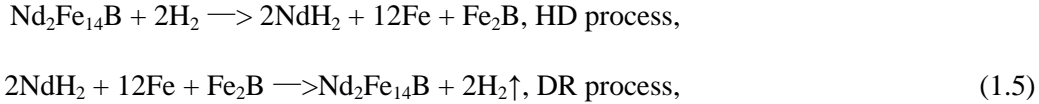


Figure 1.6 The schematic illustration of the HDDR process [42].



#### 1.4.4 Nd-Fe-B films

The hard magnetic films have potential to be applied in the microelectromagnetic systems, such as microactuators and micromotors [66-67]. The films are also very useful to clarify the coercivity mechanism by fabricating an ideal modeled microstructure. A well-textured Nd-Fe-B film with high coercivity was successfully fabricated by Cadieu et al [68]. The orientation of the Nd<sub>2</sub>Fe<sub>14</sub>B grains was aligned by the epitaxial growth on a strongly textured buffer layer or a single crystal substrate. The coercivity improvement can be realized by the increase in the Nd content or the deposition of a Nd-Cu or Nd-Ag layer [69-71]. Cui et al. reported a record coercivity value ~2.95 T in the Nd-Ag diffused Nd-Fe-B thin films [71]. A high coercivity ~2.7 T was also reported in the 3 μm Nd-Fe-B thick films by using a relative high ratio of Nd element and adding Cu to lower the melting temperature of Nd-rich phase and facilitate its redistribution [70]. This research group also succeeded in developing 5 μm Nd-Fe-B thick films with high performance of coercivity ~1.6 T and (BH)<sub>max</sub> ~400 kJm<sup>-3</sup> [72].

### 1.5 Coercivity mechanism of Nd-Fe-B magnets

The coercivity ( $H_c$ ) is a term used to characterize the ability of the hard magnetic materials to resist the external magnetic fields without the magnetization reversal. An energy barrier provided by the magnetocrystalline anisotropy ( $K$ ) has to be overcome to reverse the magnetization of a magnet by the external magnetic fields or the thermal fluctuations. The discovery of the new magnetic materials with a large value of the magnetocrystalline anisotropy contributed to the development of the permanent magnets as shown in Figure 1.1. But the investigations on the coercivity mechanism of the permanent magnets are quite complex, because the coercivity is closely related to the microstructure of the magnets, which is dependent on the composition, manufacturing, and post-annealing process. In addition, the magnetic dipolar interactions and the exchanging interactions between the neighboring magnetic grains make the analysis of the coercivity mechanism much more complicated.

### 1.5.1 Magnetization reversal

The coercivity of a magnet is determined by the easiest path of the magnetization reversal process. The magnetization reversal can occur either continuously through a coherent or incoherent rotation, or discontinuously through a dynamic domain motion. Impeding the magnetization rotation by magnetocrystalline anisotropy and impeding the nucleation and propagation of the reverse domain, a high coercivity can be achieved [73].

The well-known Stoner-Wohlfarth model is the simplest model of the magnetization reversal, assuming a coherent rotation mode of the magnetization reversal process in a single domain particle [74]. It assumes a tiny ellipsoid with a uniform magnetization is in a magnetic field at an angle to the anisotropy axis. Such condition results in a switching from the metastable state to the stable one to minimize the energy density, which needs to jump an energy barrier. In such a case the coercivity is given by

$$H_c = 2K_1/\mu_0M_s - NM_s, \quad (1.6) [75-76]$$

where  $K_1$  is the magnetocrystalline anisotropy constant,  $M_s$  is the saturation magnetization of the hard phase, and  $N$  is the demagnetization factor. When the Stoner-Wohlfarth particle is sphere with  $N=0$ , using the  $K_1$  and  $M_s$  value of the  $Nd_2Fe_{14}B$ , the theoretic coercive field equals to the anisotropy field  $\sim 7.5$  T, which gives the upper bound of the coercivity.

However, the coherent rotation mode is so restrictive and unrealistic. An incoherent rotation mode, called curling mode, describes the magnetization reversal via several collective processes. The curling mode introduces the exchange energy. In such case not all the spins need to overcome the magnetocrystalline anisotropy simultaneously, making the hurdle much lower, which leads to the coercivity inferior to the anisotropy field. The nucleation field for the curling mode is given by

$$H_n = 2K_1/\mu_0M_s - NM_s + 2A/\mu_0M_s*[1.84/R]^2, \quad (1.7) [77]$$

where  $A$  is the exchange stiffness. Equation (1.7) contains a term from the exchange energy of the incoherent magnetization which decreases following a  $1/R^2$  law.

In the real permanent magnets with large magnetocrystalline anisotropy, the curling mode explains only very small corrections to the theoretic coercivity value and there is still large discrepancy between the observed coercivity and the theoretic coercivity, which is known as Brown's Paradox [75]. It indicates that the coercivity is not a property of the homogeneous magnetic materials and it is necessary to consider the structural inhomogeneities. The defects existed at the main phase usually reduce the local magnetocrystalline anisotropy. The magnetization reverses easily in such defects where the anisotropy energy barrier is low under the effect of an inverse external field. And then the domain walls propagate

from the defects to the whole grain, and the magnetization of the whole magnets was reversed cooperatively due to the additional demagnetization field and exchange coupling. The structural inhomogeneities also provide some pinning sites against the domain wall motion. The pinning force of the domain walls comes from the energy difference of the inhomogeneities. The pinning is either repulsive type where the inhomogeneities have higher anisotropy energy than that of the main phase and consequently the propagation of the domain walls is energetically unfavorable to the high anisotropy regions or attractive type where the domain walls are captured in the low anisotropy regions.

### 1.5.2 Micromagnetic model

The micromagnetic model is used to analyze the external magnetic field or temperature required to reverse the magnetization. For simplification it is assumed that the nucleation occurs at the first local departure from the saturation. This model considers an inhomogeneous microstructure with the low-anisotropy grain boundary regions. Also the misaligned grain, the exchange energy and the demagnetizing field from the surface and volume charges are included in this model. The nucleation field at the external magnetic field under an angle  $\psi_0$  to the easy direction of the magnetization is expressed by the well-known Kronmüller equation as [77-79]:

$$Hc = 2K_1/M_s * \alpha_K \alpha_\psi - N_{\text{eff}} M_s, \quad (1.8)$$

where the microstructural parameter  $\alpha_K$  describes the reduction in the anisotropy field due to the presence of the deteriorated grain boundaries, the angular microcrystalline parameter  $\alpha_\psi$  describes the reduction in the anisotropy field due to the misalignment of the grains, and  $N_{\text{eff}}$  is the effective demagnetization factor accounting for the dipolar interactions and local demagnetization fields.

### 1.5.3 Nucleation and pinning

The value of parameter  $\alpha_K$  depends on the types and dimensions of the defects. Supposing a planar inhomogeneity with thickness of  $r_0$ ,

$$\alpha_K^{\text{nuc}} = 1 - \delta_B^2 / 4\pi^2 r_0^2 * [-1 + (1 + 4\Delta K r_0^2 / A)^{1/2}]^2, \quad (1.9)$$

where  $\delta_B = \pi(A/K_1)^2$  is the domain wall width. Three approximate expressions for the  $\alpha_K^{\text{nuc}}$  can be derived as following [77]:

- a. Narrow inhomogeneities  $r_0 < \delta_B$ :  $\alpha_K^{\text{nuc}} \approx 1 - r_0^2 / \delta_B^2$ .
- b. Inhomogeneity with average thickness  $2\pi r_0 > \delta_B$ :  $\alpha_K^{\text{nuc}} \approx \delta_B / \pi r_0$ .
- c. Extended inhomogeneity  $2r_0 \gg \delta_B$ :  $\alpha_K^{\text{nuc}} \approx 1 - \Delta K / K_1(\infty)$ .

In the case a, the nucleation field is not influenced by the reduced anisotropy regions since the exchange energy can average over the narrow inhomogeneities; in the case b, the nucleation field obeys a  $1/r_0$  law; in the case c, the nucleation field is determined by the minimum value of  $(K_1(\infty) - \Delta K)$  [83].

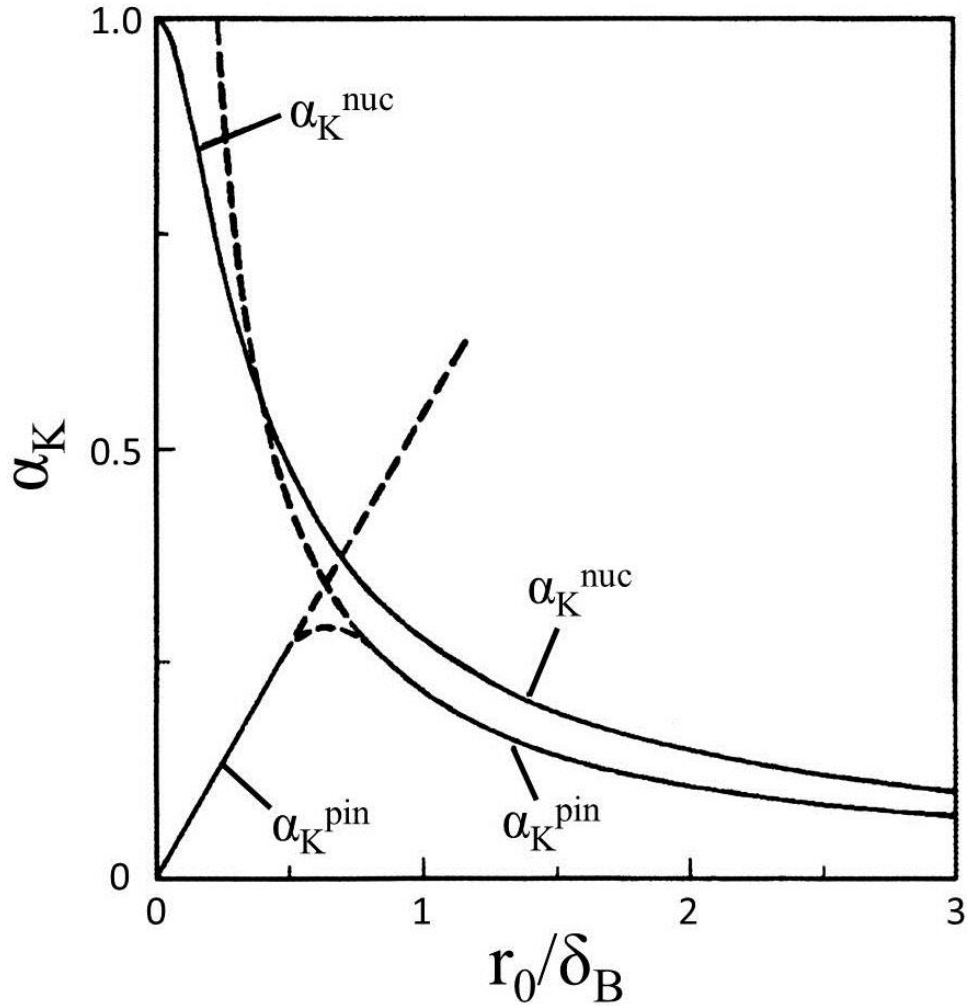


Figure 1.7 The parameter  $\alpha_K$  for the pinning and nucleation in planar perturbations of width  $r_0$  as a function of  $r_0/\delta_B$  [79].

In the pinning-controlled mechanism, the point defects and dislocations may improve the coercive fields whereas the planar inhomogeneities like grain boundaries which have different magnetic properties with the main phase act as effective pinning sites [80-82]. In the case of pinning of the domain walls by planar inhomogeneities,  $\alpha_K^{\text{pin}}$  is given by [77,83-84]

$$\alpha_K^{\text{pin}} = \pi r_0 / 27^{1/2} \delta_B * (A/A' - K_1^2/K_1) \text{ for narrow planar inhomogeneities } r_0 < \delta_B, \quad (1.10)$$

and

$$\alpha_K^{\text{pin}} = 2\delta_B/3\pi r_0 \text{ for extended planar inhomogeneities } r_0 > \delta_B, \quad (1.11)$$

where  $K$  and  $K'$  are the magnetocrystalline anisotropies of the main phase and the planar inhomogeneity, respectively,  $A$  and  $A'$  are the exchange energy of the main phase and the planar inhomogeneity, respectively. The  $\alpha_K^{\text{pin}}$  holds for the conditions of  $r_0 < \delta_B$  and  $r_0 < \delta_B$ . The determination of  $\alpha_K^{\text{pin}}$  at the crossover point of these two regions, that is  $r_0 = \delta_B$ , gives the maximum coercivity value achievable by pinning-controlled mechanism. In such case, a maximum value  $\sim 0.3$  is obtained for  $\alpha_K^{\text{pin}}$ . The pinning-controlled mechanism is used to analyze the coercivity of the melt-spun, hot-deformed, and HDDR-processed Nd-Fe-B magnets [85-88]. The Lorentz microscopy is often used to observe the interactions between the domain walls and the grain boundaries.

Figure 1.7 shows parameter  $\alpha_K$  for the pinning and nucleation in planar perturbations of width  $r_0$  as a function of  $r_0/\delta_B$  [79]. The comparison of  $\alpha_K^{\text{nuc}}$  and  $\alpha_K^{\text{pin}}$  can classify whether the coercivity is determined by nucleation-controlled mechanism or pinning-controlled mechanism.  $\alpha_K^{\text{nuc}}$  decreases approximately following a  $1/r_0$  law while  $\alpha_K^{\text{pin}}$  increases linearly with  $r_0$ .  $\alpha_K^{\text{pin}}$  also follows the  $1/r_0$  law if the domain wall bowing is possible, but lies below  $\alpha_K^{\text{nuc}}$ . According to Figure 1.7, when  $\alpha > 0.3$ , the coercivity mechanism is only compatible with the nucleation-controlled type, while in the case of  $\alpha < 0.3$ , both the pinning-controlled as well as the nucleation-controlled mechanisms are involved. This figure indicates that the pinning field is always smaller than the nucleation field at the inhomogeneity. When the reversed domain propagates from other defects with much lower nucleation field, the pinning is the only mechanism that can prevent the wall from passing over the inhomogeneity.

#### 1.5.4 Angular dependence of coercivity

An applied magnetic field antiparallel to the magnetization direction of a magnet is used when we measure the coercive field. If there is an angle  $\psi_0$  between the field and easy axis, the measured coercivity value will change. First, there is a reduction of the coupling energy by a factor of  $\cos\psi_0$  between the magnetization and the applied magnetic field; secondly, the noncolinearity between the magnetization and the applied magnetic fields induces a torque to rotate the magnetization moments to the field direction [89-90]. Thus, in the real magnets we have to take into account the misalignment of the grains, which is reflected by  $\alpha_\psi$  in Equation (1.8). The  $\alpha_\psi$  is given by [77]

$$\alpha_\psi^{\text{nuc}} = 1/\cos\psi_0 * 1/[1 + (\tan\psi_0)^{2/3}]^{3/2} * \{1 + 2K_2/K_1 * (\tan\psi_0)^{2/3}/[1 + (\tan\psi_0)^{2/3}]\}, \quad (1.12)$$

$$\alpha_\psi^{\text{pin}} = 1/\cos\psi_0, \quad (1.13)$$

where  $\psi_0$  is the angle between the applied field and the negative easy direction of the magnetization. In the case of the nucleation-controlled mechanism where the coherent rotation of the Stoner-Wohlfarth model takes place in the defects and the angular dependence of coercivity decreases from 1 for a small  $\psi_0$  and shows a minimum value at  $\psi_0 = \pi/4$  and then increases again for a large  $\psi_0$ , whereas the pinning coercive fields increase with the misalignments of the grains as shown in Figure 1.8 [79]. Equation (1.12) includes the higher order anisotropy constant  $K_2$  at the case of low temperature, because the reversible rotation process is strongly affected by  $K_2$  with decreasing temperature.

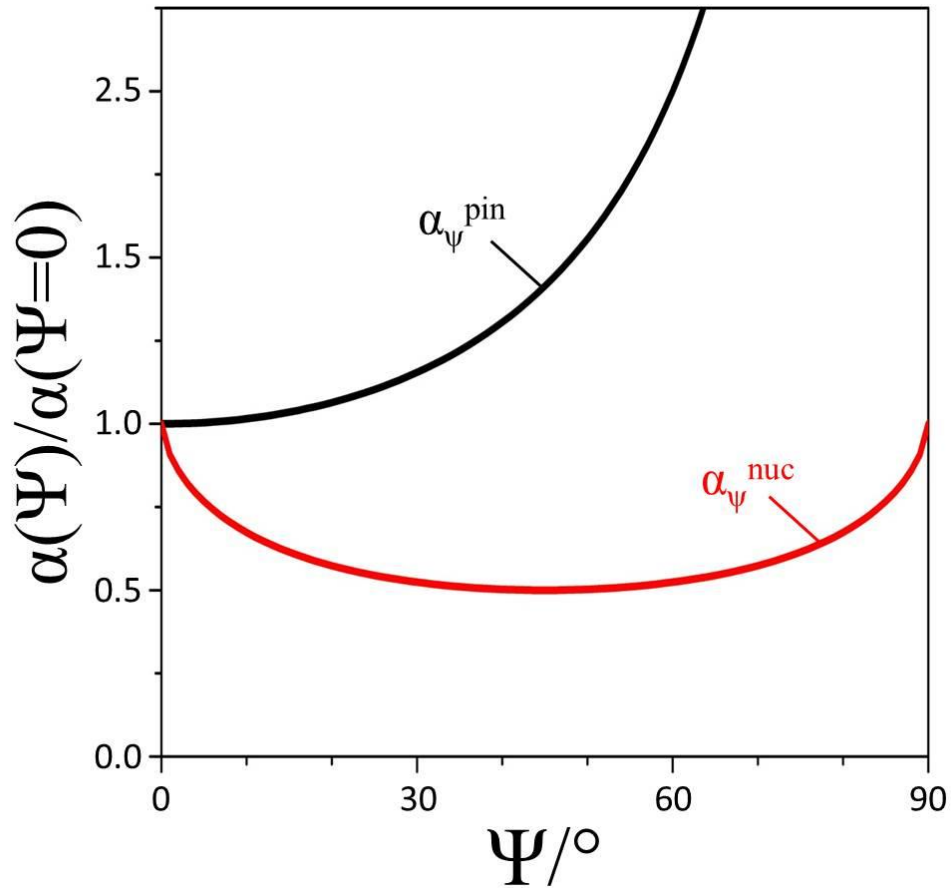


Figure 1.8 Angular dependence of the theoretical  $\alpha_{\psi}$  for the nucleation and pinning [79].

### 1.5.5 Temperature dependence of coercivity

The coercivity of the Nd-Fe-B magnets is very sensitive to the temperature and they exhibit a monotonous decrease of coercivity with the temperature. However, the temperature dependence of the coercivity shows characteristic differences in the high and low temperature range.

Equation (1.8) is derived from a single particle. Considering the coercivity is determined by the lowest nucleation field, for an ensemble of grains a minimum value of  $\alpha_\psi$ , that is  $\alpha_{\psi,\min} = \alpha_\psi(\pi/4)$ , is chosen to calculate the minimum coercive field  $H_N^{\min}$ . Thus, the Equation (1.8) can be rewritten as [77,79,91]

$$H_c = 2K_1/M_s * \alpha_K \alpha_\psi^{\min} - N_{\text{eff}} M_s, \quad (1.14)$$

$$H_c = \alpha_K H_N^{\min} - N_{\text{eff}} M_s, \quad (1.15)$$

$$H_c/M_s = \alpha_K H_N^{\min}/M_s - N_{\text{eff}}, \quad (1.16)$$

A linear relation is observed by plotting  $H_c/M_s$  vs  $H_N^{\min}/M_s$  within a large temperature range. But the deviations are found at low and high temperature range. At the low temperature range, the influence of the second order anisotropy constant  $K_2$  becomes significant due to the spin reorientation of  $\text{Nd}_2\text{Fe}_{14}\text{B}$  [92]. At the high temperature, one interpretation of the derivation is due to the coercivity mechanism transfers from nucleation to pinning type [77,79]. Another reasonable explanation is that the grain boundary inhomogeneity becomes paramagnetic at such a high temperature. If without the nonferromagnetic grains, the two-phase Nd-Fe-B magnets show a better temperature dependence of coercivity [93]. This is because the anisotropy field and the saturation magnetization decrease at different rate with increasing temperature and the stray field term  $N_{\text{eff}} M_s$  is less dependent than  $\alpha_K H_N^{\min}$  [79,94]. Thus, the term  $N_{\text{eff}} M_s$  compensates the term  $\alpha_K H_N^{\min}$  at the elevated temperature. The better temperature dependence of the coercivity is an important character for the permanent magnets potential to be used at the high operating temperature.

### 1.5.6 Global model

The global model, also called nucleation expansion model, is an energetic approach to analyze the coercivity mechanism of the Nd-Fe-B magnets [95]. This model assumes the preformed nucleus expands via a thermally activated process within the lifetime,  $\tau$ , of the reversed nucleus following the an Arrhenius law, that is  $\tau = \tau_0 \exp(-\Delta E/kT)$  [95-99].  $\Delta E$  denotes the activation enthalpy required to expand the nucleus and  $\Delta E = kT \ln(t/\tau_0) \approx 25kT$ .  $\tau_0$  is the time of the origin when measuring the magnetic aftereffect. The activation energy includes the domain wall energy, the magnetostatic energy of the external field and the demagnetization field. Therefore,

$$s\gamma_B - \mu_0 M_s H_c v - \mu_0 N_{\text{eff}} M_s^2 v = 25kT, \quad (1.17)$$

Since the nucleus is formed in a defect, the domain wall energy  $\gamma_B' = \alpha_B \gamma_B = \alpha_B * 4(AK_1)^{1/2}$ , where  $\alpha_B$  is the microstructural parameter. The nucleus surface  $s$  is related to the volume by  $s = \alpha_s v^{2/3}$ ,  $\alpha_s$  is a geometrical parameter. The coercive field in the global model then can be derived from Equation (1.17) as following:

$$H_c = 2\alpha_s \alpha_B / \pi \alpha_v * 2K_1 / \mu_0 M_s - N_{\text{eff}} M_s - 25kT / \mu_0 v M_s, \quad (1.18)$$

Even though the physics basics are different, the coercivity field described in the global model is similar as the micromagnetic model except the term on the thermal fluctuation field  $25kT / \mu_0 v M_s$ , which is neglected in the micromagnetic model since it only corresponds to 5~10% of the coercive field [77]. The percentage will become larger if the value determined by the first two items in Equation (1.18) becomes small, which is the realistic case. The global model is often used to study the temperature dependence of coercivity in the Nd-Fe-B magnets [100-102].

## 1.6 Strategies to improve the coercivity of Nd-Fe-B magnets

The very good magnetic properties of the Nd-Fe-B permanent magnets have significant contributions on the miniaturization of the device and the improvement of the performance characteristics. As mentioned at the beginning of this chapter, the applications of the Nd-Fe-B magnets in the air conditioner compressor motors, wind power generators, traction motors of hybrid electric vehicles (HEV), electric power steering motors (EPS), etc have increased remarkably and captured one of the biggest market shares now. The production of the Nd-Fe-B sintered magnets has steadily increased from 6 000 tons in 1996 to 63 000 tons in 2008 [103], and a forecast on the world demand for the Nd-Fe-B sintered magnets saying that the production will reach to 160 000 tons in 2020 [104]. However, the operating temperature of these applications is typically ~200 °C and the coercivity of the Nd-Fe-B magnets reduces to a very low value due to the thermal demagnetization. A coercivity of ~0.8 T at ~200 °C or ~2.5 T at room temperature is required to satisfy these applications. Although the theoretic coercive value of the Nd<sub>2</sub>Fe<sub>14</sub>B phase is ~7.5 T, the demagnetizing fields as well as the defects with low magnetocrystalline anisotropy field in the magnets lead to a reduction in the coercivity to a value of ~1.2 T, which is only 15% of the anisotropy field of Nd<sub>2</sub>Fe<sub>14</sub>B phase. One easy way to increase the coercivity is to increase the magnetocrystalline anisotropy of the Nd<sub>2</sub>Fe<sub>14</sub>B phase by substituting Nd by Dy due to a much higher magnetocrystalline anisotropy field of Dy<sub>2</sub>Fe<sub>14</sub>B, ~15.0 T. Figure 1.9 shows the (BH)<sub>max</sub> and coercivity of the commercial sintered magnets and their compositions [105]. The ratio of Dy to Nd increases to as

high as 0.4 as the operating temperature of the application increases. However, the natural abundance of Dy is less than 10% of Nd. It means there is a potential supply crisis of the raw materials if the Dy-free or Dy-saving Nd-Fe-B magnets were not developed. In addition, the antiparallel couple of Dy magnetic moments and Fe moments leads to a reduction in the remanence, and consequently in  $(BH)_{max}$ . Therefore, many investigations have been carried out to improve the coercivity of the Nd-Fe-B magnets without reliance on the heavy rare earth elements. According to Equation (1.8), it can be known that the coercivity can be improved by the optimization of the intrinsic and extrinsic parameters.

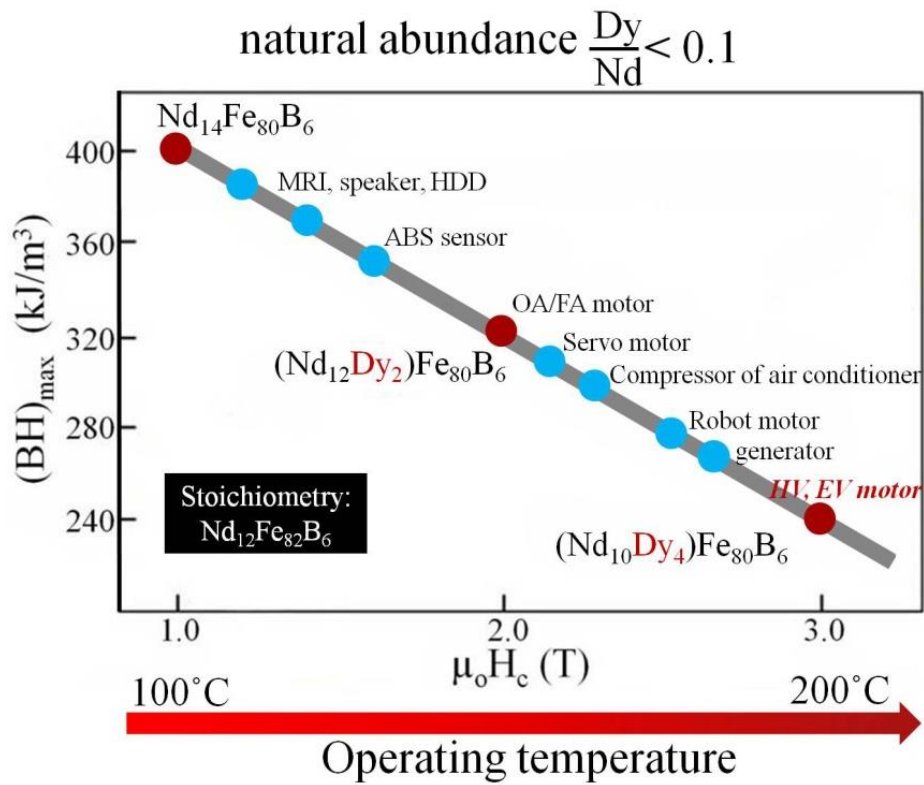


Figure 1.9 Maximum energy product  $(BH)_{max}$  and coercivity of the commercial sintered magnets and their compositions [105].

### 1.6.1 Additives

The microstructure and intrinsic properties of the Nd-Fe-B magnets are sensitive to the additives. According to the solubility within the  $\text{Nd}_2\text{Fe}_{14}\text{B}$  phase, the additives are sorted as the substituent and dopant elements. The substitute elements replace Nd atoms or/and Fe atoms in the  $\text{Nd}_2\text{Fe}_{14}\text{B}$  phase, therefore, change the intrinsic properties, such as the magnetocrystalline anisotropy field, the saturation magnetization, and the Curie temperature. Partially substituting Nd by the heavy rare earth element Dy or Tb substantially increases the anisotropy field and consequently the coercivity [106]. So, Dy is usually added to the commercial sintered Nd-Fe-B magnets to enhance the coercivity to a level of 3.0 T. But the saturation magnetization decreases due to the antiparallel coupling of Dy and Fe. Another common substituent element used in the commercial Nd-Fe-B magnets is Co and it increases the Curie temperature and decreases the temperature dependence of coercivity, leading to a better thermal stability [24]. But the formation of the Laves-type soft magnetic Nd-(Fe,Co) phase deteriorates the coercivity [107-109]. As for the dopant elements, Fidler et al reported that two different types can be distinguished regardless of the processing routes [110]. The representative elements of type I dopants are low-melting metals like Al, Ga, Cu, which can be found in the commercial Nd-Fe-B magnets with very small amount. They affect the wetting ability of the liquid phase during the processing and form Nd-type I dopants intergranular phases after cooling, which better isolate the  $\text{Nd}_2\text{Fe}_{14}\text{B}$  grains [111-116]. Therefore, the lattice distortions are reduced and the grain boundaries become smooth. The type II dopants have a low solubility within the  $\text{Nd}_2\text{Fe}_{14}\text{B}$  phase and form the high-melting intergranular borides and precipitates within the grains (Ti, V, Mo, W, Nb). Small amount of Ti was found to be effective in increasing the coercivity and thermal stability of the Nd-Fe-B magnets by the formation of the precipitates  $\text{TiB}_2$  [117-118]. V was formed the  $\text{V}_2\text{FeB}_2$  phase, inhibiting the grain growth [119-120]. In the real magnets, it is common to combine different types of additives to achieve high performance magnets.

### 1.6.2 Grain boundary diffusion process (GBDP)

The well-known grain boundary diffusion process was reported by H. Nakamura et al. in 2005 [121-122]. The magnets were coated with Dy or Tb oxide or fluoride powders and subsequently heat-treated at the temperature 900-1000 °C under an Ar atmosphere. The heavy rare earth elements diffused into the magnets via the grain boundaries and Dy- or Tb-rich shells were formed near the grain boundaries of the  $\text{Nd}_2\text{Fe}_{14}\text{B}$  phase by replacing Nd during the heat treatment. The coercivity of the magnets was significantly improved while the remanence was almost the same. The substitution of Dy or Tb for Nd changes the intrinsic properties of  $\text{Nd}_2\text{Fe}_{14}\text{B}$  phase. The Dy- or Tb- shells substantially improve the magnetocrystalline anisotropy near the grain boundaries where the defects often exist. The little use of

Dy or Tb is also effective to avoid the reduction of the remanent magnetization. This is a heavy rare earth saving technique to improve the coercivity of the Nd-Fe-B magnets.

Based on the previous work, a modified grain boundary diffusion process by introducing the Nd-transmission metal eutectic alloy into the grain boundary layer was proposed and initially employed on the HDDR processed magnets [64-65]. When the mixture of the HDDR powders and the diffused alloys was annealed at  $\sim 700$  °C, the Nd-transmission metal eutectic alloys melted and diffused into the powders through the grain boundaries. As a result, the thickness of the grain boundary increased and the microstructural isolation of the  $\text{Nd}_2\text{Fe}_{14}\text{B}$  phase became better and consequently the coercivity was reported to be increased to  $\sim 2.0$  T. This approach was successfully extended to the hot-deformed Nd-Fe-B magnets, meanwhile the diffusion sources were extended to Pr, Nd-transmission metal alloy, and the coercivity was improved to 2.6 T in the diffused hot-deformed Nd-Fe-B magnets [123-124]. However, the remanent magnetization dropped a lot due to the hard magnetic  $\text{Nd}_2\text{Fe}_{14}\text{B}$  phase was diluted by introducing substantial non-ferromagnetic elements and an expansion along the c-axis direction was also observed in the diffused hot-deformed Nd-Fe-B magnets [124]. To solve this problem, a so-called Nd-Cu eutectic diffusion process under expansion constraint was developed to minimize the loss of the remanent magnetization [125]. This diffused magnets exhibit a coercivity of  $\sim 2.0$  T, remanence of  $\sim 1.36$  T, and (BH)max of  $\sim 358$   $\text{kJm}^{-3}$  at room temperature. Encouragingly, taking advantaging of the ultrafine grain size this magnets exhibit a (BH)max value of  $\sim 191$   $\text{kJm}^{-3}$  at 200 °C, which is superior to the 4% Dy-containing sintered magnets.

### 1.6.3 Grain size

One effective approach to improve the coercivity of the Nd-Fe-B permanent magnets is to refine the grain size of the  $\text{Nd}_2\text{Fe}_{14}\text{B}$  phase while retain a thin continuous Nd-rich GB phase [126-130]. It is predicted that the coercivity follows  $\ln(D/L)$  by assuming that the magnetization reversal process occurs by the nucleation of the reverse domain from the grain boundaries of magnetically isolated grains as the dotted line in Figure 1.8 [105,131-132].  $L$  is a characteristic length scale to make the inside of  $\ln$  dimensionless and it can be a domain wall exchange length parameter. It is reported that the decrease in the grain size leads to a reductions in the number density of defects on the grain size [132-133] and the local demagnetization field [94, 134]. However, since the grains size is strongly dependent on the mean particle size, when the grain size becomes less than 3  $\mu\text{m}$ , the coercivity of the sintered Nd-Fe-B magnets starts to deteriorate [127-129]. Li et al. reported that the Nd-rich phase is oxidized seriously in the fine powders with grain size of less than 3  $\mu\text{m}$  while a certain fraction of the metallic Nd which is necessary to form thin grain boundary layers is present in the relatively larger grain-sized sintered magnets [135].

Recently, a helium jet milling and pressless sintering process was developed to control the oxygen impurities when the grain size was reduced to  $\sim 1 \mu\text{m}$  and the coercivity was successfully leveled up to 2 T in the fine-grained Nd-Fe-B sintered magnets [38-39]. The initial magnetization curve of the fine-grained magnets shows a two-step behavior, which is a common feature in the rapidly solidified and hot-deformed magnets, whose grain size is near the single domain size [136]. The domain walls displace within the grains and then get pinned at the grain boundaries. So, the susceptibility is high initially and subsequently becomes low. Then a magnetic field higher than the pinning field is required to reverse the single domain grains. To realize the coercivity exceeding 2.5 T, Sagawa proposed a further reduction of the grain size to  $\sim 0.5 \mu\text{m}$  using the pressless sintering process [137]. In such case, the powder size must be  $\sim 0.3 \mu\text{m}$ , which would be challenging in industrial mass production system because of the explosive nature of such fine rare earth alloy powders.

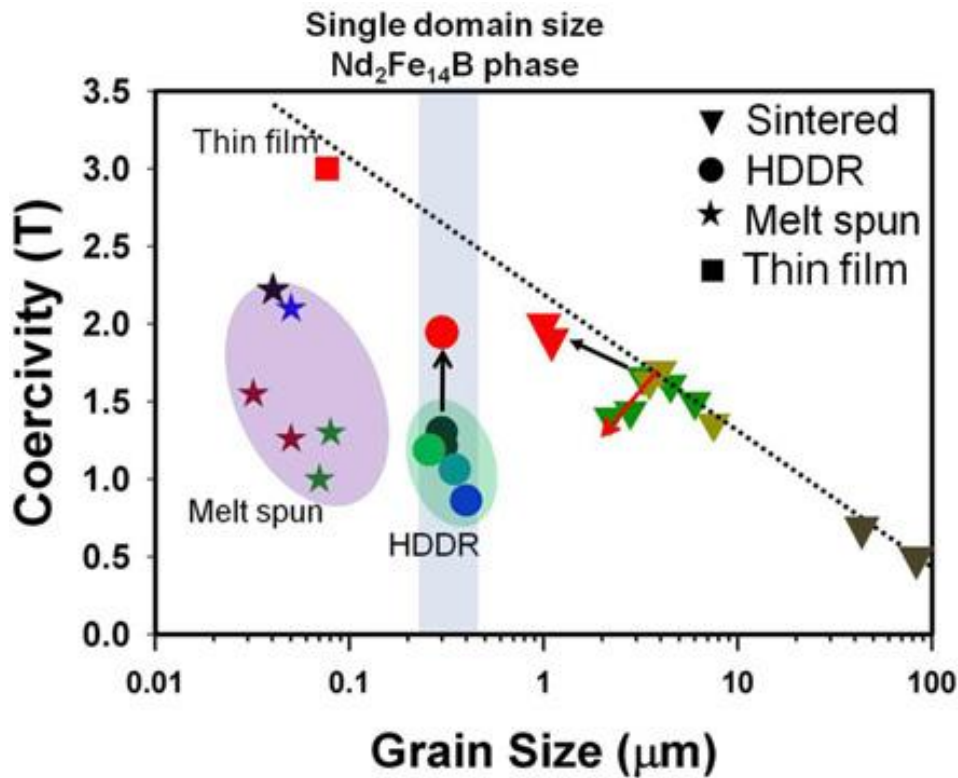


Figure 1.8 Coercivity vs. grain size for sintered magnets, HDDR powders, melt-spun ribbons and thin films [105].

The hot-deformed Nd-Fe-B magnets consist of the anisotropic Nd<sub>2</sub>Fe<sub>14</sub>B grains with an ultrafine grain structure of nearly a single domain size [40-41]. Since the size of the flakes produced by crushing the rapidly solidified melt-spun ribbons is  $\sim 150 \mu\text{m}$ , which is one orders of magnitude larger than those of

jet-milled powders for the sintered magnets, the oxidation of the metallic Nd-rich phase can be effectively suppressed in the hot-deformed Nd-Fe-B magnets. The isotropically oriented nanocrystals in rapidly solidified powders develop to be laterally elongated grains with a strong c-axis texture parallel to the pressing direction during the hot-deformation process, which gives rise to high remanence comparable to that of sintered magnet. A recent work has shown that a maximum energy product of the hot-deformed Nd-Fe-B magnets comparable to that of sintered magnets with a slightly higher coercivity can be achieved [138].

## 1.7 Motivation of this work and outline of this thesis

Even though the hot-deformed Nd-Fe-B magnets have advantages over sintered ones on the aspect of much smaller grains and free of the Nd-oxide phases, their coercivity is disappointingly low for the single-domain-sized grains and the value is only comparable to that of the sintered magnets with the grain size of  $\sim 5 \mu\text{m}$ . The motivation of this work is to investigate the microstructure and coercivity relationship of the hot-deformed anisotropic Nd-Fe-B magnets and provide some clues to improve the coercivity further.

This thesis is divided into 7 chapters. Chapter 1 gives a general introduction and literature review of the Nd-Fe-B magnets. Chapter 2 generally describes the experiment procedure and multiscale characterization techniques employed in the experiment. Chapter 3 discusses the effect of the Nd content on the microstructure and coercivity of the hot-deformed Nd-Fe-B magnets. Chapter 4 talks about the grain size dependence of coercivity of the hot-deformed Nd-Fe-B magnets. Chapter 5 illustrates the microstructure evolution of the hot-deformed Nd-Fe-B magnets. Chapter 6 presents the modeled microstructures by using the thin film fabrication technique to establish the microstructure features required for a coercivity of 3.0 T in the real bulk Nd-Fe-B magnets. Chapter 7 is the summary this work.

## Reference

- [1] International Energy Statistics, U.S. Energy Information Administration.
- [2] J.M.D. Coey, IEEE Transactions on Magnetics, 47, 4671 (2011).
- [3] Neodymium Rare Earth Permanent Magnet, HITACHI, [www.hitachi.com](http://www.hitachi.com).
- [4] Low RPM Generators, PMGL, [www.pmgenerators.com](http://www.pmgenerators.com).
- [5] E. de Vries, “The application of permanent magnet generators is gaining ground in the wind turbine industry”, renewable energy network, April 2010.
- [6] Alternative Fuels Data Center, U.S. Department of Energy.
- [7] Toyota Motor Corporation, “Toyota hybrid system”, May 2003.
- [8] J. Fidler, D. Suess, T. Schrefl, “Rare-earth Intermetallics for Permanent Magnet Applications”, Handbook of Magnetism and Advanced Magnetic Materials, John Wiley & Sons, Ltd., 2007.
- [9] G. Hoffer, K.J. Strnat, IEEE Transactions on Magnetics, 2, 487 (1966).
- [10] K.J. Strnat, G. Hoffer, J. Olson, W. Ostertag, J. Becher, Journal of Applied Physics, 38, 1001 (1967).
- [11] F.F. Westendorp, K.H.J. Buschow, Solid State Communications, 7, 639 (1969).
- [12] K.H.J. Buschow, P.A. Naastepad, F.F. Westendorp, Journal of Applied Physics, 40, 4029 (1969).
- [13] O. Gutfleisch, “High-temperature samarium cobalt permanent magnets”, Nanoscale Magnetic Materials and Applications, Springer, 337 (2009).
- [14] J.D. Livingston, D.L. Martin, Journal of Applied Physics, 48, 1350 (1977).
- [15] R.K. Mishra, G. Thomas, T. Yoneyama, A. Fukuno, T. Ojima, Journal of Applied Physics, 52, 2517 (1981).
- [16] H. Nagel, Journal of Applied Physics, 50, 1026 (1979).
- [17] L. Rabenberg, R. Mishra, G. Thomas, Journal of Applied Physics, 53, 2389 (1982).
- [18] A.E. Ray, S. Liu, Journal of Materials Engineering and Performance, 1, 183 (1992).
- [19] J.J. Croat, Applied Physics Letters, 39, 357 (1981).
- [20] J.J. Croat, Journal of Applied Physics, 53, 3161 (1982).
- [21] N.C. Koon, B.N. Das, Applied Physics Letters, 39, 840 (1981).

- [22] J.J. Croat, J.F. Herbst, R.W. Lee, and F.E. Pinkerton, *Journal of Applied Physics*, 55, 2078 (1984).
- [23] J.J. Croat, J.F. Herbst, R.W. Lee, and F.E. Pinkerton, *Applied Physics Letters*, 44, 148 (1984).
- [24] M. Sagawa, S. Fujimura, N. Togawa, H. Yamamoto, Y. Matsuura, *Journal of Applied Physics*, 55, 2083 (1984).
- [25] Y. Matsuura, *Journal of Magnetism and Magnetic Materials*, 303, 344 (2006).
- [26] J.F. Herbst, J.J. Croat, W.B. Yelon, *Journal of Applied Physics*, 57, 4086 (1985).
- [27] M. Sagawa, S. Fujimura, H. Yamamoto, Y. Matsuura, S. Hirosawa, *Journal of Applied Physics*, 57, 4094 (1985).
- [28] S. Hirosawa, Y. Matsuura, H. Yamamoto, S. Fujimura, M. Sagawa, H. Yamauchi, *Journal of Applied Physics*, 59, 873 (1986).
- [29] W. Mo, L. Zhang, Q. Liu, A. Shan, J. Wu, M Komuro, *Scripta Materialia*, 59, 179 (2008).
- [30] T.T. Sasaki, T. Ohkubo, K. Hono, Y. Une, M. Sagawa, *Ultramicroscopy*, 132, 222 (2013).
- [31] Y. Shinba, T.J. Konno, K. Ishikawa, K. Hiraga, M. Sagawa, *Journal of Applied Physics*, 97, 053504 (2005).
- [32] F. Vial, F. Joly, E. Nevalaien, M. Sagawa, K. Hiraga, K.T. Park, *Journal of Magnetism and Magnetic Materials*, 242, 1329 (2002).
- [33] R.K. Mishra, *Journal of Applied Physics*, 62, 967 (1987).
- [34] J. Liu, H. Sepehri-Amin, T. Ohkubo, K. Hioki, A. Hattori, T. Schrefl, K. Hono, *Acta Materialia*, 61, 5387 (2013).
- [35] H. Sepehri-Amin, J. Liu, T. Ohkubo, K. Hioki, A. Hattori, T. Schrefl, K. Hono, *Scripta Materialia*, 69, 647 (2013).
- [36] I.R. Harris, C. Noble, T. Bailey, *Journal of the Less Common Metals*, 106, L1 (1985).
- [37] ShinEtsu Rare Earth Magnets, <http://www.shinetsu-rare-earth-magnet.jp/masspro/index.html>.
- [38] Y. Une, M. Sagawa, Paper presented at the 21<sup>st</sup> International Workshop on Rare Earth Permanent Magnets and Their Applications, Bled, Slovenia, 2010.
- [39] H. Sepehri-Amin, Y. Une, T. Ohkubo, K. Hono, M. Sagawa, *Scripta Mater.* 65, 396 (2011).
- [40] R.W. Lee, *Applied Physics Letter*, 46, 790 (1985).

- [41] R.W. Lee, E.G. Brewer, N.A. Schaffel, IEEE Transactions on Magnetics, MAG-21, 1958 (1985).
- [42] S. Sugimoto, Journal of Physics D: Applied Physics, 44, 064004 (2011).
- [43] R.K. Mishra, J. Mater. Eng. 11, 87 (1989).
- [44] H. Kronmüller, and S. Parkin, “Handbook of Magnetism and Advanced Magnetic Materials”, Wiley-Interscience, 2007.
- [45] W. Grünberger, D. Hinz, A. Kirchner, K.H. Müller, and L. Schultz, Journal of Alloys and Compounds, 257, 293 (1997).
- [46] R.K. Mishra, and T.Y. Chu, L.K. Rabenberg, Journal of Magnetism and Magnetic Materials, 84, 88 (1990).
- [47] R.K. Mishra, and R.W. Lee, Applied Physics Letter, 48, 733 (1986).
- [48] V.V. Volkov, and Y. Zhu, Journal of Applied Physics, 85, 3254 (1999).
- [49] L.H. Lewis, Y. Zhu, and D.O. Welch, Journal of Applied Physics, 76, 6235 (1994).
- [50] T.D. Nguyen, K.M. Krishnan, L.H. Lewis, Y. Zhu, and D.O. Welch, Journal of Applied Physics, 79, 4848 (1996).
- [51] T. Takeshita, R. Nakayama, Proceedings of the 11th International Workshop on Rare Earth Permanent Magnets and Their Applications, Pittsburgh, U.S., (1990).
- [52] P.J. McGuinness, X.J. Zhang, X.J. Yin, I.R. Harris, Journal of the Less Common Metals, 158, 359 (1990).
- [53] R. Nakayama, T. Takeshita, Journal of Alloys and Compounds, 193, 259 (1993).
- [54] T. Tomida, R. Choi, Y. Maehara, M. Uehara, H. Tomizawa, S. Hirosawa, Journal of Alloys and Compounds, 242, 129 (1996).
- [55] O. Gutfleisch, B. Gebel, N. Mattern, Journal of Magnetism and Magnetic Materials, 210, 5 (2000).
- [56] T. Tomida, N. Sano, K. Hanafusa, H. Tomizawa, S. Hirosawa, Acta Materialia, 47 875 (1999).
- [57] O. Gutfleisch, N. Martinez, M. Verdier, I.R. Harris, Journal of Alloys and Compounds, 204, L21 (1994).
- [58] S. Sugimoto, O. Gutfleisch, I.R. Harris, Journal of Alloys and Compounds, 260, 284 (1997).

- [59] O. Gutfleisch, G. Drazic, C. Mishima, Y. Honkura, *IEEE Transactions on Magnetics*, 38, 2958 (2002).
- [60] O. Gutfleisch, K. Khlopkov, A. Teresiak, K.H. Muller, G. Drazic, C. Mishima, Y. Honkura, *IEEE Transactions on Magnetics*, 39, 2926 (2003).
- [61] Y. Honkura, C. Mishima, N. Hamada, G. Drazic, O. Gutfleisch, *Journal of Magnetism and Magnetic Materials*, 290, 1282 (2005).
- [62] H. Sepehri-Amin, T. Ohkubo, K. Hono, K. Güth, O. Gutfleisch, *Acta Materialia*, 85, 42 (2015).
- [63] K. Suresh, T. Ohkubo, Y.K. Takahashi, K. Oh-ishi, R. Gopalan, K. Hono, T. Nishuchi, N. Nozawa, S. Hirosawa, *Journal of Magnetism and Magnetic Materials*, 321, 3681 (2009).
- [64] H. Sepehri-Amin, T. Ohkubo, T. Nishiuchi, S. Hirosawa, K. Hono, *Scripta Materialia*, 63, 1124 (2010).
- [65] C. Mishima, K. Noguchi, M. Yamazaki, H. Mitrai, Y. Honkura, *Proceedings of the 21th International Workshop on Rare Earth Permanent Magnets and Their Applications*, Bled, Slovenia, 2010.
- [66] S. Yamashita, J. Yamasaki, M. Ikeda, N. Iwabuchi, *Journal of Applied Physics*, 70, 6627 (1991).
- [67] H. Lemke, T. Lang, T. Göddenhenrich, C. Heiden, *Journal of Magnetism and Magnetic Materials*, 148, 426 (1995).
- [68] F.J. Cadieu, T.D. Cheung, L. Wickramasekara, *Journal of Magnetism and Magnetic Materials*, 535, 54 (1986).
- [69] N.M. Dempsey, *Presentation in the 2nd international Symposium on the Advanced Magnetic Materials and Applications*, Sendai, Japan, 2010.
- [70] N.M. Dempsey, T.G. Woodcock, H. Sepehri-Amin, Y. Zhang, H. Kennedy, D. Givord, K. Hono, O. Gutfleisch, *Acta Materialia*, 61, 4920 (2013).
- [71] W.B. Cui, Y.K. Takahashi, K. Hono, *Acta Materialia*, 59, 7768 (2011).
- [72] N.M. Dempsey, A. Walther, F. May, D. Givord, K. Khlopkov, O. Gutfleisch, *Applied Physics Letters*, 90, 092509 (2007).
- [73] J.D. Livingston, *Journal of Applied Physics*, 52 2544 (1981).
- [74] E.C. Stoner, E.P. Wohlfarth, *Philosophical Transactions of the Royal Society of London*, 240, 599 (1948).

- [75] W.F. Brown, *Reviews of Modern Physics*, 17, 15 (1945).
- [76] W.F. Brown, *Journal of Applied Physics*, 30, 1305 (1959).
- [77] H. Kronmüller, M. Fähnle, “*Micromagnetism and the Microstructure of Ferromagnetic Solids*”, Cambridge University Press, 2003.
- [78] H. Kronmüller, *Physics Status Solidi B: Basic Research*, 144, 385 (1987).
- [79] H. Kronmüller, K.D. Durst, M. Sagawa, *Journal of Magnetism and Magnetic Materials*, 74, 291 (1988).
- [80] H. Nagel, *Journal of Applied Physics*, 50, 1026 (1979).
- [81] H. Kronmüller, K.D. Durst, W. Ervens, W. Fernengel, *IEEE Transactions on Magnetics*, MAG-20, 1569 (1984).
- [82] G.C. Hadjipanayis, R.C. Hazzelton, K.R. Lawless, L.S. Horon, *IEEE Transactions on Magnetics*, MAG-18, 1460 (1982).
- [83] H. Kronmüller, *Journal of Magnetism and Magnetic Materials*, 7, 341 (1978).
- [84] R. Friedberg, D.J. Paul, *Physical Review Letters*, 34, 1234 (1975).
- [85] D. Li, K.J. Strnat, *Journal of Applied Physics*, 57, 4143 (1985).
- [86] G.C. Hadjipanayis, A. Kim, *Journal of Applied Physics*, 63 3310 (1988).
- [87] R.K Mishra, *Journal of Magnetism and Magnetic Materials*, 54, 450 (1986).
- [88] F. Von Staa, K.A. Hempel, H. Artz, *Journal of Magnetism and Magnetic Materials*, 157, 25 (1996).
- [89] D. Givord, M. Rossignol, D. Taylor. *Journal de Physique IV*, 02, C3 (1992).
- [90] H. Kronmüller, K.D. Durst, G. Martinek, *Journal of Magnetism and Magnetic Materials*, 69, 149, (1987).
- [91] G. Martinek, H. Kronmüller, *Journal of Magnetism and Magnetic Materials*, 86, 177 (1990).
- [92] S. Hirosawa, K. Tokuhara, Y. Matsuura, H. Yamamoto, S. Fujimura, M. Sagawa, *Journal of Magnetism and Magnetic Materials*, 61, 363 (1986).
- [93] H. Kronmüller, *Supermagnets* (Dordrecht: Kluwer Academic), pp 461, 1991.
- [94] H. Sepehri-Amin, T. Ohkubo, M. Gruber, T. Schrefl, K. Hono, *Scripta Materialia*, 89, 29 (2014).

- [95] D. Givord, P. Tenaud, T. Vaidieu, *IEEE Transactions on Magnetics*, 24, 1921 (1988).
- [96] D. Givord, A. Lienard, P. Tenaud, T. Viadieu, *Journal of Magnetism and Magnetic Materials*, 67, L281 (1987).
- [97] J.M. Gonzalez, A.K. Giri, C. De Julian, M. Veley, J.L. Vicent, *Europhysics Letters*, 28, 143 (1994).
- [98] L. Néel, *Journal de Physique et Le Radium*, 12, 339 (1951).
- [99] D.W. Taylor, V. Villas-Boas, Q. Lu, M.F. Rossignol, F.P. Missell, D. Givord, S. Hirosawa, *Journal of Magnetism and Magnetic Materials*, 130, 225, 1994.
- [100] H. Miyajima, T. Yamamoto, Y. Otani, *Journal of Magnetism and Magnetic Materials*, 104, 1117, (1992).
- [101] J.C. Martinez, F.P. Missell, *Journal of Applied Physics*, 64, 5726, (1988).
- [102] C. De Julian, J.M. Gonzalez, *Journal of Magnetism and Magnetic Materials*, 140, 1055 (1995).
- [103] Y. Luo, *Proceedings of the 20th International Workshop on Rare Earth Permanent Magnets and Their Applications*, Crete, Greece, 2008.
- [104] M. Sagawa, *Proceedings of the 21th International Workshop on Rare Earth Permanent Magnets and Their Applications*, Bled, Slovenia, 2010.
- [105] K. Hono, H. Sepehri-Amin, *Scripta Materialia*, 67, 530 (2012).
- [106] M. Sagawa, G. Fujimura, H. Yamamoto, Y. Matsuura, K. Hiraga, *IEEE Transactions on Magnetics*, 20, 1584 (1984).
- [107] T. Mizoguchi, I. Sakai, H. Niu, K. Inomata, *IEEE Transactions on Magnetics*, 23, 2281 (1987).
- [108] C.J. Yang, S.D. Choi, W.Y. Li, *Journal of Applied Physics*, 69, 5524 (1991).
- [109] H. Yamamoto, S. Hirosawa, S. Fujimura, K. Tokuhara, H. Nagata, M. Sagawa, *IEEE Transactions on Magnetics*, 23, 2100 (1987).
- [110] J. Fidler, T. Schrefl, *Journal of Applied Physics*, 79(8), 5029 (1996).
- [111] E. Burzo, A.T. Pedziwiatr, W.E. Wallace, *Solid State Communications*, 61, 57 (1987).
- [112] K.D. Durst, H. Kronmüller, *Journal of Magnetism and Magnetic Materials*, 68, 63 (1987).
- [113] W. Tang, S. Zhou, R. Wang, *Journal of Applied Physics*, 65, 3142 (1989).
- [114] M. Endoh, M. Tokunaga, H. Harada, *IEEE Transactions on Magnetics*, 23, 2290 (1987).

- [115] B. Grieb, C. Pithan, E. Henig, G. Petzow, *Journal of Applied Physics*, 70, 6354 (1991).
- [116] J. Fidler, J. Bernardi, *Journal of Applied Physics*, 70, 6456 (1991).
- [117] Y. Kitano, J. Shimomura, M. Shimotomai, Y. Fukuda, A. Fujita, Y. Ozaki, *Journal of Alloys and Compounds*, 193, 245 (1993).
- [118] T.S. Chin, C.H. Lin, Y.H. Huang, J.M. Yau, S.J. Heh, F.D King, *IEEE Transactions on Magnetics*, 29, 2788 (1993).
- [119] S. Hirosawa, H. Tomizawa, S. Mino, Hamamura, *IEEE Transactions on Magnetics*, 26, 1960 (1990).
- [120] X.J. Yin, I.P. Jones, I.R. Harris, *Journal of Magnetism and Magnetic Materials*, 116, L325 (1992).
- [121] H. Nakamura, K. Hirota, M. Shima, T. Minowa, M. Honshima, *IEEE Transactions on Magnetics*, 41, 3844 (2005).
- [122] K. Hirota, H. Nakamura, T. Minowa, M. Honshima, *IEEE Transactions on Magnetics*, 42, 2909 (2006).
- [123] H. Sepehri-Amin, T. Ohkubo, S. Nagashima, M. Yano, T. Shoji, A. Kato, T. Schrefl, K. Hono, *Acta Materialia*, 61, 6622 (2013).
- [124] T. Akiya, J. Liu, H. Sepehri-Amin, T. Ohkubo, K. Hioki, A. Hattori, K. Hono, *Journal of Applied Physics*, 115, 17A766 (2014).
- [125] T. Akiya, J. Liu, H. Sepehri-Amin, T. Ohkubo, K. Hioki, A. Hattori, K. Hono, *Scripta Materialia*, 81, 48 (2014).
- [126] S. Hirosawa, *IEEE Transactions on Magnetics*, 25, 3437 (1989).
- [127] P. Nothnagel, K.H. Müller, D. Echert, A. Handstein, *Journal of Magnetism and Magnetic Materials*, 101, 379 (1991).
- [128] C.N. Christodoulou, J. Schlup, G.C. Hadjipanayis, *Journal of Applied Physics*, 61, 3760 (1987).
- [129] B.M. Ma, *Materials Research Society Symposium Proceedings*, 96, 143 (1987).
- [130] K. Uestuener, M. Katter, W. Rodewald, *IEEE Transactions on Magnetics*, 42, 2897 (2006).
- [131] R. Ramesh, K. Srikrishna, *Journal of Applied Physics*, 64, 6406, (1988).
- [132] R. Ramesh, G. Thomas, B.M. Ma, *Journal of Applied Physics*, 64, 6416 (1988).
- [133] Z. Chen, F. Xie, Z. Shi, L. Wang, H. Fu, *Journal of Applied Physics*, 70, 1 (1991).

- [134] W. Tang, S. Zhou, B. Hu, *Journal of Magnetism and Magnetic Materials*, 94, 67 (1991).
- [135] W.F. Li, T. Ohkubo, K. Hono, M. Sagawa, *Journal of Magnetism and Magnetic Materials*, 321, 1100 (2009).
- [136] K. Hioki, Y. Kojima, T. Morita, A. Hattori, Paper presented at International Magnetism Conference, Intermag'12, Vancouver, Canada, 2012.
- [137] M. Sagawa, Paper presented at the 22nd International Workshop on Rare-Earth Permanent Magnets and Their Applications, Nagasaki, Japan (2012).
- [138] H. Haizuka, A. Hattori, *Denki Seiko*, 82, 85 (2011).

## Chapter 2. Experiment

As we have already known that the coercivity of the Nd-Fe-B magnets is strongly related to the microstructure and chemical composition of the grain boundaries whose thickness is less than 3 nm, a comprehensive multi-scale structural characterization is required to figure out the feature of the grain boundary phase and understand the coercivity mechanism of the Nd-Fe-B permanent magnets. Electron microscopes, including scanning electron microscope (SEM) and transmission electron microscope (TEM), are used to provide the information about morphology, phase distribution, elemental mapping, and so on. To analyze the chemistry of the grain boundary, a laser assisted wide angle three dimensional atom probe (3DAP) is a good and reliable instrument. This chapter gives a brief explanation about these characterization techniques.

### 2.1 Scanning electron microscopy (SEM)

The hot-deformed Nd-Fe-B magnets were polished by using 500, 1000, 2400, and 4000 grit SiC papers to smooth the surface before SEM observation. The ethanol was used as the lubricant and cooling liquid during the mechanical polishing.

SEM is a characterization instrument that images a specimen by scanning it with a beam of electrons to get information at or near the surface of the specimen. The electrons interact with the atoms in the specimen generating signals that contain information about its surface topography, composition, phase distribution, and so on. The main signals are secondary electrons, backscattered electrons (BSE), X-rays, and cathodoluminescence, which are shown schematically in Figure 2.1. Secondary electrons can be used to make secondary electron image to reveal the details of sample surface. BSE are a beam of electrons that are reflected from the sample by elastic scattering. Since the contrast of the BSE image depends on the atomic number of each element, BSE SEM images can provide information about the distribution of different elements in the sample. In this study, Carl Zeiss CrossBeam 1540 EsB instrument was used for the SEM observations and the surface of the samples was cleaned by using the focused ion beam (FIB).

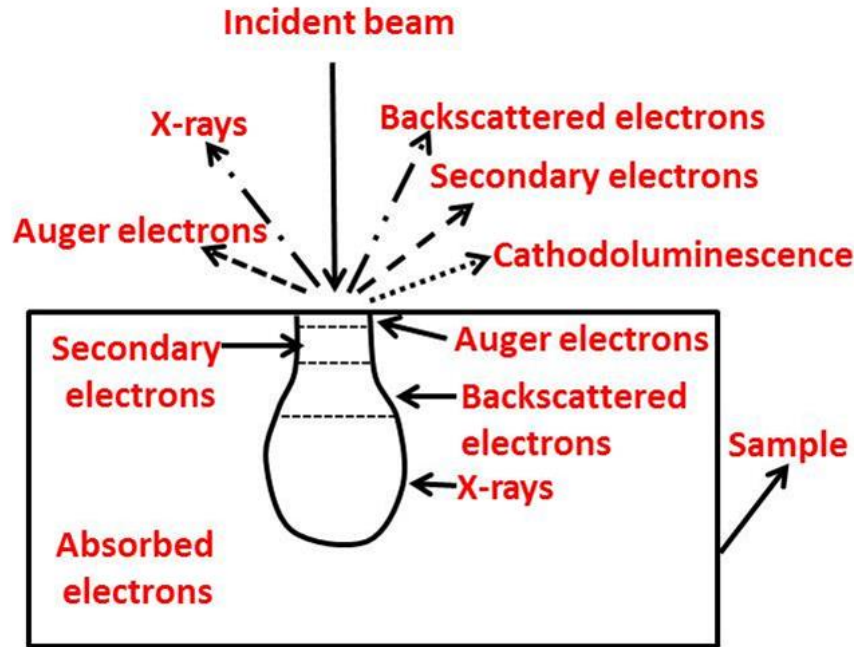


Figure 2.1 Interaction between electron beam and sample in SEM instrument.

## 2.2 Transmission electron microscopy (TEM)

TEM is a type of electron microscopy where a beam of electrons transmits through an ultra-thin specimen, interacting with it as the beam passes through. An image is formed from the interaction of the electrons transmitted through the specimen, and the image is magnified by a series of magnetic lenses and focused onto an image device or detected by a sensor such as a CCD camera [1]. In this study, FEI F30 and FEI Titan G2 80-200 TEM were employed for the TEM observations. Different imaging techniques used in this study are explained below:

### 2.2.1 Bright field (BF) image

The bright field imaging mode is the most common mode in the TEM operations. With use of an objective aperture, undiffracted electrons can be selected to form a bright field image, which gives information about how the materials structure looks like, especially the grain structure and the morphology of the interfacial phases.

### **2.2.2 High resolution transmission electron microscopy (HRTEM)**

HRTEM provides images of crystallographic structure of the sample at an atomic scale. Because of its high resolution, it is a valuable tool to study the nanoscale properties of the crystalline materials. In this study, we use HRTEM technique to observe the microstructure of the grain boundary phase and the Nd-rich phase in the hot-deformed Nd-Fe-B magnets.

### **2.2.3 Electron energy loss spectroscopy (EELS)**

In EELS, a material is exposed to a beam of electrons with a known and narrow range of kinetic energies. Some of the electrons which are scattered inelastically have lost certain amount of energy due to the interaction with the electrons of the elements they encounter. The amount of energy loss can be measured via an electron spectrometer, giving information about existing elements in the specimen and the element distribution.

### **2.2.4 Lorentz TEM microscopy in Fresnel mode**

The Lorentz TEM microscopy is used to investigate the relationship between the magnetic structure and crystal structure as well as the magnetic domain wall movement. Based on TEM instrument, the Lorentz TEM microscopy provides a very high spatial resolution of ~10 nm and is highly sensitive to the small change of the local magnetic domains. The lens Lorentz microscopy offsets the magnetic field from the objective lens. Therefore magnetic structure, i.e. the magnetic domains, under thermally demagnetized state can be observed. In addition, the external field generating device enables us to observe the dynamic motion of the magnetic domain walls.

Figure 2.2 illustrates the principle of the Lorentz TEM microscopy in Fresnel mode [2]. The incident electron beam is deflected by Lorentz force due to the opposite in-plane magnetization in the neighboring domains. This causes variation of electron density at domain walls. So, the domain walls are visible by the dark lines and bright lines.

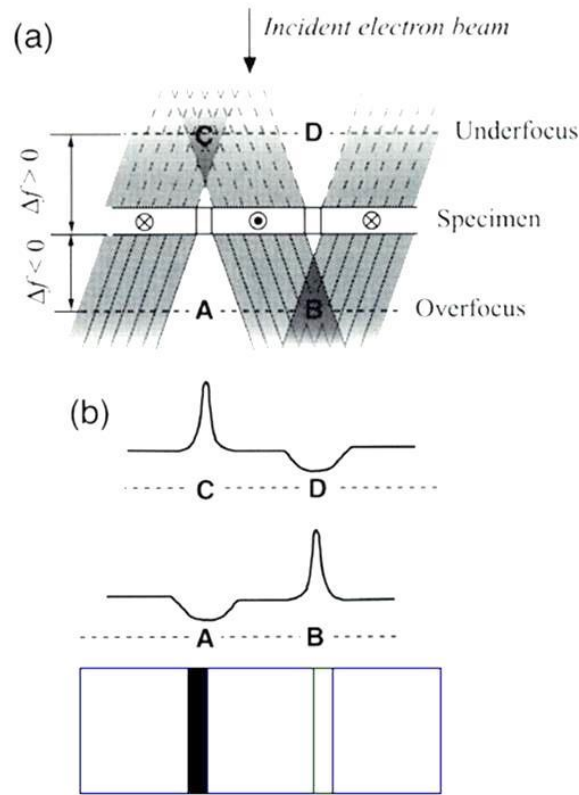


Figure 2.2 Schematic illustration of principle of Lorentz TEM microscopy in Fresnel mode [2].

## 2.3 Laser assisted three dimensional atom probe (3DAP)

### 2.3.1 Atom probe specimen preparation

In order to obtain an electrical field high enough to field-evaporate atoms, the specimen for 3D atom probe analysis must be a very sharp needle. Typically, the tip should have an apex diameter of less than 100 nm. The preparation of the atom probe tip is the most difficult part of the atom probe experiment. In this study, the specimens for atom probe analysis were prepared by a focused ion beam (FIB) system in order to observe the location of the grain boundaries.

FIB instruments have been employed for the sample preparation for transmission electron microscopy and 3DAP studies. In the FIB system of this study (Hitachi FB-2100 and FEI Helios NanoLab™ 650), the Ga ions are extracted from a liquid metal ion source unit and accelerated through a column with specific accelerating voltage between 1-30 keV. Due to hitting the surface of sample with Ga

ion beam, the surface of the sample is sputtered. The secondary electrons and ions are produced after collision with sample, which can be used for generating FIB image via an imaging detector. Moreover, by using the ion beam assisted chemical vapor deposition, metals like W can be deposited on the surface of the sample to avoid the surface damage from the ion beam or bond the specimen with a tip holder or fill the gap [3].

Generally, the preparation of a 3DAP tip involves in a two-step process which is lift-out method and annular Ga ion beam milling [4]. To protect the sample from the irradiation damage by the Ga ion beam, a Ni layer with ~200 nm and a W layer with ~500 nm were deposited by the plasma sputtering coating and ion beam deposition, respectively, as a capping layer. A block was extracted from the bulk matrix with a micromanipulator equipped with a sharp W probe as shown in Figure 2.3(a)-(d). Then, a separately prepared W needle was set up as a tip holder, and the apex of the needle was cut off to make a flat surface for mounting a part of the block. After one part of the block was bonded to the prepared W tip, the other part of the block was removed to leave a square rod (Figure 2.4(c)), and the gap between the rod and the W tip was filled by W deposition (Figure 2.4(f)). Finally, the specimen was milled to a sharp needle with annular Ga ion beam milling by a dual-beam (SEM/FIB) system (Carl Zeiss CrossBeam 1540 EsB). In this stage the Ga ion beam was applied to the atom probe probing region. The sample thickness was decreased to around 1  $\mu\text{m}$  first by 30 kV ion beam milling. Thereafter, the diameter of sample was decreased by a finer milling to around 200 nm using annular milling. The final tip with apex diameter less than 100 nm was prepared with 3 kV Ga ion beam milling. Generally, the usage of the first two steps is good enough to make a nice shape needle specimen, and the third step using a filled circle milling instead of the annular milling allows us to bring a specific interesting region into the analyzable range for atom probe tomography. The schematic of tip sharpening process by dual-beam system is shown in Figure 2.5 [5].

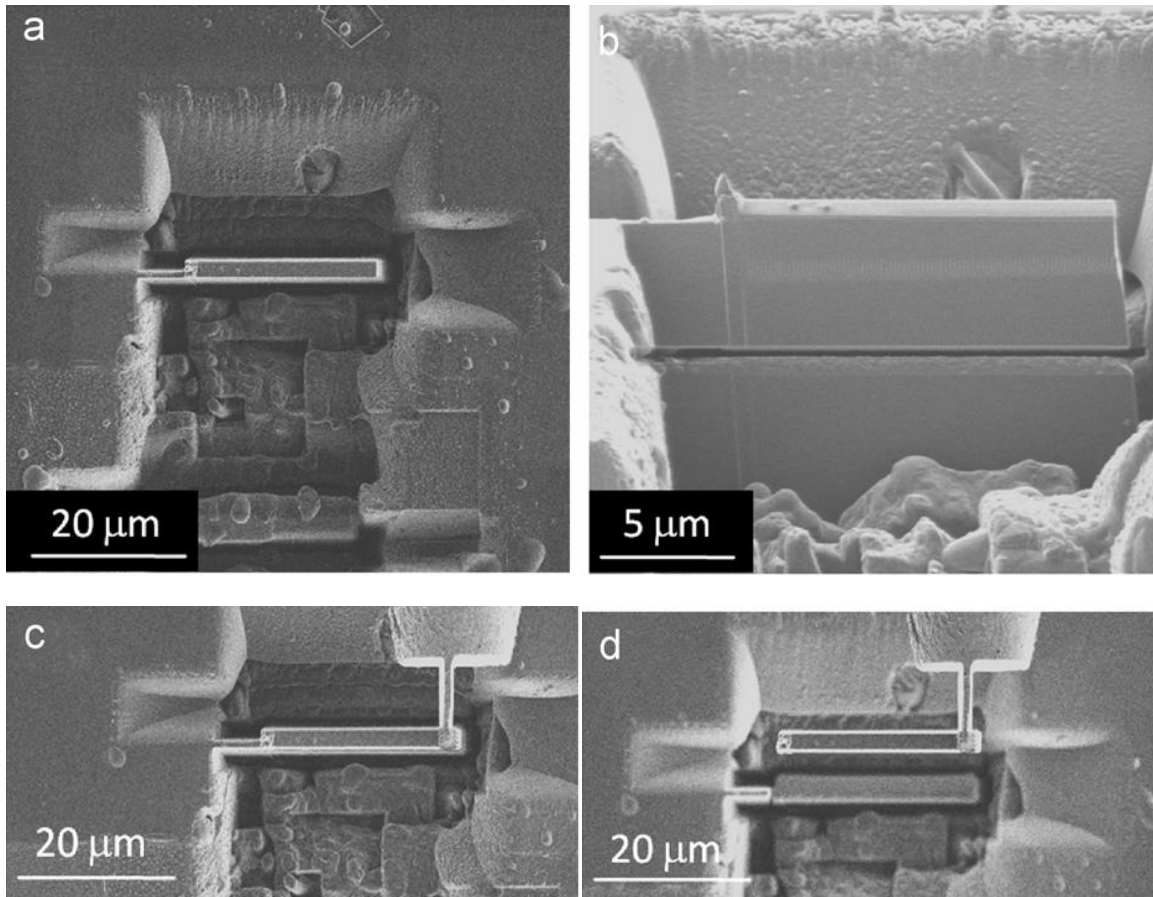


Figure 2.3 (a) Trenching mill around the deposited capping layer at a stage tilt of  $0^\circ$ , (b) bottom mill at a stage tilt of  $60^\circ$ , (c) micromanipulator bonded to the block using W deposition, (d) a block was extracted from the bulk sample and lifted out by the micromanipulator [4].

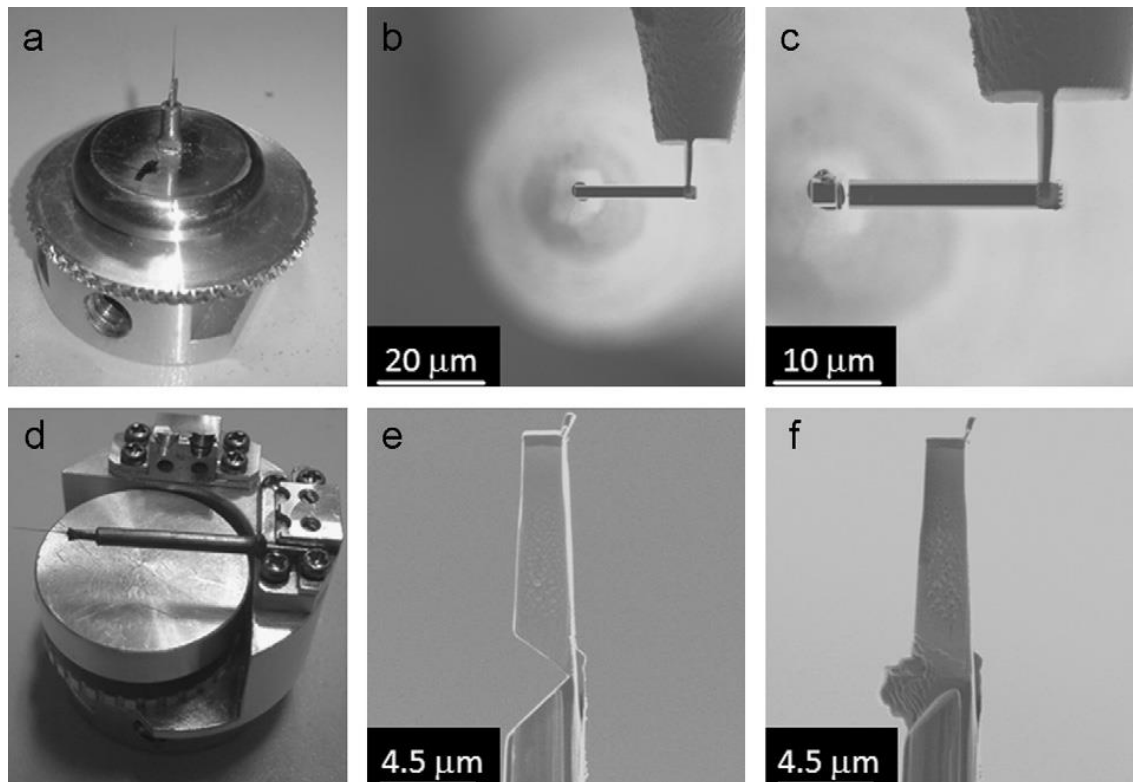


Figure 2.4 (a) Tungsten needle and specimen holder for the attaching process, (b) block attached to the prepared W tip holder, (c) block bonded to the W tip holder and slicing into two parts, (d) specimen holder for gap filling, (e) the side view of a part of the block sitting on the W tip holder, (f) the filled gap [4].

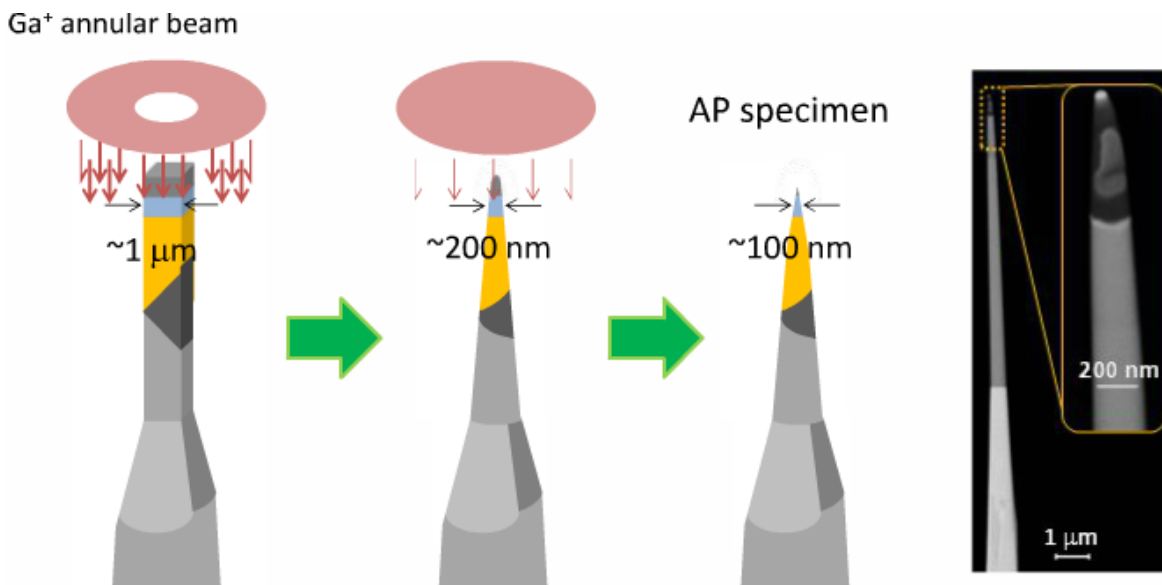


Figure 2.5 Schematic illustration of the tip sharpening process by a dual-beam system (SEM/FIB) [5].

### 2.3.2 Laser assisted 3D atom probe

Three dimensional atom probe is a strong instrument for the analysis of the local chemistry and structure of materials at atomic scale. Ultrahigh resolution of this technique which is less than 0.5 nm makes it superior to the other characterization techniques. 3DAP can provide information about the distribution of different elements in three dimensions, and it is capable of quantitatively analysis even for light elements such as H and Li [6].

The instrument consists of three ultra-high vacuum (UHV) chambers: air lock, specimen storage and analysis chamber. Specimens are put into the specimen storage chamber through the air lock chamber. Before 3DAP analysis, usually we do the field ion microscopy (FIM) observation by introducing the imaging gases of He, Ne and H<sub>2</sub>. After obtaining FIM images, the imaging gases are pumped away, and the atom probe analysis is performed in the analysis chamber in an UHV and a very low temperature. A DC voltage is applied on the sample, and using a femto second pulse laser, the atoms on the apex of sample are ionized and fly to a delay line detector. Afterwards, according to the time of flight of each individual ionized atom, using the positive sensitive detector (PSD), two dimensional atomic distributions can be identified. With continuing the atom probe analysis and ionization of atoms layer by layer, three dimensional elemental map can be reconstructed afterwards (Figure 2.6). The acquired data are analyzed by Tap3Ddata analysis software, PoSAP analysis software (Oxford nanoScience version 1.70), and CAMECA integrated visualization and analysis software (CAMECA IVAS version 3.6.0). Using these softwares, the atomic distribution of different elements and chemical composition of different phases can be determined from the reconstructed data.

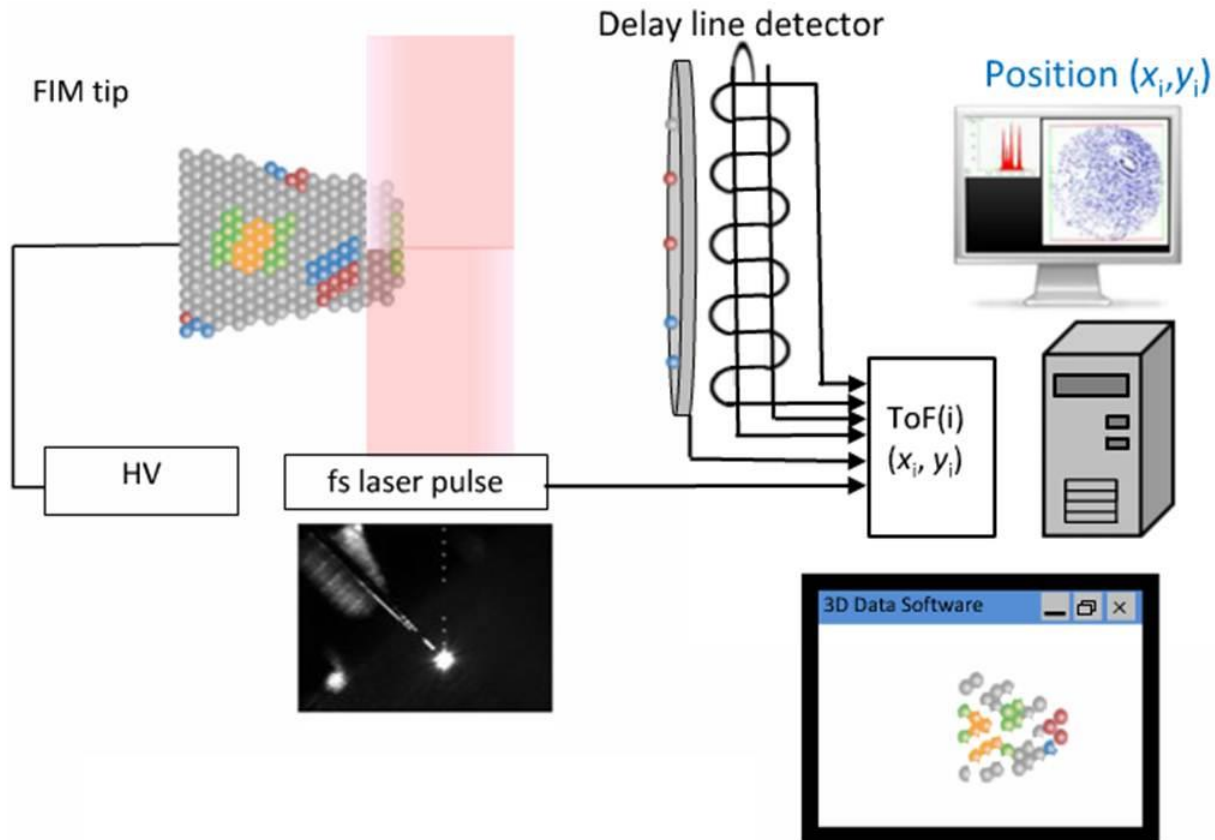


Figure 2.6 Schematic illustration of laser assisted 3D atom probe [7].

The atom probe analysis in this study was conducted with a locally built laser assisted 3D atom probe equipped with CAMECA's advanced delay line detector [8]. The distance between the tip and the detector was ~120 mm and the acceptance angle of the detector was about 0.32 sr. A femto second laser (Amplitude systems s-Pulse HR, wavelength: 1030nm, maximum pulse energy: 10 mJ/pulse, pulse width: 400 fs) was used to irradiate the specimen apex to assist field evaporation. Second and third harmonic generation (Amplitude SHG-THG) unit were used to convert the wavelength to 343 nm (UV). The laser was focused to 150  $\mu\text{m}$  diameter at the specimen apex by two focusing lenses and the position was adjusted by moving a mirror located in the front of the final lens with a two-axis stage controller (SIGMA KOKI, Stepping Motor Drive SHOT-102) to maximize the acquisition flux. All the measurements were conducted under UHV  $< 10^{-8}$  Pa at base temperature of ~25 K in flux range 0.003-0.01 atom/pulse with laser energy of ~12 mW.

## Reference

- [1] D.B Williams, C.B. Carter, “Transmission Electron Microscopy-A Textbook for Materials Science”, Springer US, 2009.
- [2] <http://www.nims.go.jp/AEMG/recent/Lorentz/Lorentz-e.html>.
- [3] L.A. Giannuzzi, F.A. Stevie, “Introduction to focused ion beams, Instrumentation, Theory, Techniques and Practice”, Springer Science, 2005.
- [4] M. Kodzuka, T. Ohkubo, K. Hono, F. Matsukura, H. Ohno, Ultramicroscopy, 109, 644 (2009).
- [5] <http://www.nims.go.jp/apfim/SpecimenPrepFIB.html>.
- [6] H. Sepehri-Amin, T. Ohkubo, K. Hono, K. Güth, O. Gutfleisch, Acta Materialia, 85, 42 (2015).
- [7] [http://www.nims.go.jp/apfim/LaserAP\\_e.html](http://www.nims.go.jp/apfim/LaserAP_e.html).
- [8] G.D. Costa, F. Vurpillot, A. Bostel, M. Bouet, B. Deconihout, Review of Scientific Instruments, 76, 013304 (2005).

## Chapter 3. The effect of Nd content on the microstructure and coercivity of hot-deformed Nd-Fe-B magnets

### 3.1 Introduction

The hot-deformed Nd-Fe-B magnets produced from the polycrystalline isotropic rapidly solidified Nd-Fe-B ribbons with average size  $\sim 150 \mu\text{m}$  have an ultrafine anisotropic grain structure of near a single domain size, typically 70-100 nm thick and 200-300 nm wide [1-4]. This microstructure effectively suppresses the oxidation of the metallic Nd-rich phase during the hot-deformation process. The strong c-axis texture is introduced by the development of the isotropically oriented nanocrystals in the rapidly solidified powder into the laterally elongated grains during the hot-deformation process [5-7]. A remanence value of  $\sim 1.4 \text{ T}$  can be achieved in the hot-deformed Nd-Fe-B magnets, which is comparable to that of the commercial sintered ones. However, the highest coercivity value reported for the hot-deformed Nd-Fe-B magnets is only  $\sim 1.8 \text{ T}$  [8], which is much lower than what we can expect from single domain grains. The relatively low coercivity suggests that the magnetic isolation of the hard grain phase is not sufficient. Therefore, the structural and chemical modification of the grain boundary (GB) in the hot-deformed magnets may lead to a further increase in the coercivity. Much effort has recently been made to correlate the GB structure/chemistry with the coercivity of the sintered [9-11], hot-deformed [12-15], hydrogenation–disproportionation–desorption–recombination (HDDR) processed Nd–Fe–B magnets [16-17] and Nd-Fe-B thin films [18]. A thin grain boundary phase enriched with Nd is already known to exist in all these magnets. In the hot-deformed magnets, the coercivity is sensitive to the overall Nd-concentration of the starting material, i.e., higher coercivity can be obtained in the samples with a higher Nd content, but its origin has not been understood. However, the remanent magnetization decreases as the overall Nd-content increases. Therefore, it is necessary to optimize the coercivity at as low Nd content as possible. Hence, the aim of this work is to understand the role of the overall Nd concentration in enhancing the coercivity of the hot-deformed Nd-Fe-B magnets by correlating the microstructure and coercivity using scanning electron microscope (SEM), transmission electron microscope (TEM), three dimensional atom probe (3DAP), and micromagnetic simulations.

## 3.2 Experiment

Alloys with nominal compositions of  $\text{Nd}_{12.7}(\text{Fe},\text{Co})_{\text{bal}}\text{B}_{5.5}\text{Ga}_{0.5}$ ,  $\text{Nd}_{13.0}(\text{Fe},\text{Co})_{\text{bal}}\text{B}_{5.6}\text{Ga}_{0.5}$ , and  $\text{Nd}_{14.0}(\text{Fe},\text{Co})_{\text{bal}}\text{B}_{5.6}\text{Ga}_{0.5}$  in atomic percent were melt-spun onto a rotating copper wheel. Hereafter, these samples are denoted as 12.7Nd, 13.0Nd, and 14.0Nd, respectively. Powders of around 150  $\mu\text{m}$  were produced by crushing the melt-spun ribbons. Then they were hot-pressed in vacuum at a temperature of around 750~800 °C to achieve a complete densification. The consolidated bulks were subsequently hot-deformed in an Ar atmosphere at about 750~850 °C with a strain rate of around 0.063  $\text{s}^{-1}$  to obtain the anisotropic platelet-like grains [1,19,20]. The hot-deformation was applied with a height reduction of 72%, which corresponded to the true strain,  $\epsilon=\ln(h_E/h_0)$ , of -1.3, where  $h_0$  is the starting height of the sample and  $h_E$  is the height after the deformation. The magnetic properties of the samples were measured by a pulsed high field magnetometer with a pulsed magnetic field of 7.5 T. Backscatter electron (BSE) scanning electron microscopy (SEM) observations were made on the bulk samples using a Carl Zeiss CrossBeam 1540EsB at the acceleration voltage of 2.0 kV. Transmission electron microscopy (TEM) observations were performed using a Tecnai G2 F30 TEM and Titan G2 80-200 TEM at the acceleration voltage of 300 kV and 200 kV, respectively. Three dimensional atom probe measurements were conducted under ultrahigh vacuum  $< 10^{-8}$  Pa at a base temperature of ~25 K in the flux range of 0.003-0.01 atom/pulse with an UV laser (343 nm) with energy of ~12 mW.

The effect of the GB phase magnetization on the magnetization reversal was studied using the micromagnetic simulations on a modeled sample with a dimension of  $400\times 400\times 400 \text{ nm}^3$ . The modeled sample consisted of cuboid shape  $\text{Nd}_2\text{Fe}_{14}\text{B}$  grains with a size of  $(125\pm 25)\times(200\pm 25)\times(100\pm 25) \text{ nm}^3$ . The grains were separated by a grain boundary phase with a thickness of 4 nm. The saturation magnetization ( $\mu_0M_s$ ), magnetocrystalline anisotropy ( $K_1$ ), and exchange stiffness (A) of the  $\text{Nd}_2\text{Fe}_{14}\text{B}$  phase were chosen to be 1.61 T, 4.5  $\text{MJ/m}^3$ , and 12  $\text{pJ/m}$ , respectively [21]. The magnetocrystalline anisotropy ( $K_1$ ) and the exchange stiffness (A) of the GB phase were chosen to be 0  $\text{MJ/m}^3$  and 8  $\text{pJ/m}$  and the saturation magnetization of the GB phase was varied from 1.2 T to 0.0 T. Tetrahedron meshes were applied with a size of 2.0 nm at the grain boundaries which grew to the inside of the  $\text{Nd}_2\text{Fe}_{14}\text{B}$  grains with a maximum size of 7 nm. The Landau-Lifshitz-Gilbert (LLG) equation at each node was solved using the FEMME software [22].

## 3.2 Results

Figure 3.1 shows the magnetization curves for the samples with different Nd content. By increasing the Nd content, the coercivity ( $\mu_0 H_c$ ) increases from 0.9, to 1.29 and 1.79 T. Note that the initial magnetization curves for the three samples are different. 12.7Nd magnetizes rapidly at a low magnetic field, while the other two samples reach the saturation magnetization through a two-step procedure. They start with a high susceptibility, and then change to a lower susceptibility, and after reaching a critical field, show a steep rise again. The critical field for 14.0Nd is much higher than that for 13.0Nd. The S-shape of the initial magnetization curve has also been observed in rapidly quenched Nd-Fe-B magnets, hot-pressed hydrogenation-disproportionation-desorption-recombination (HDDR) powders, and fine-grained sintered magnets [9,23,24]. There is a peak value  $\sim 1.44$  T of the remanence. Remanence follows the equation below:

$$B_r = J_s \cdot \frac{\rho}{\rho_0} \cdot V \cdot \cos\theta, \quad (3.1)$$

where  $J_s$  is the saturation magnetization of the hard magnetic phase,  $V$  is the volume fraction of the hard magnetic grains,  $\cos\theta$  is the degree of alignment of the hard magnetic grains,  $\rho$  is the practical density of the sample, and  $\rho_0$  is the theoretic density of the bonded magnets. It is known that the presence of the liquid Nd-rich intergranular phase during the hot-deformation process favors the formation of the crystallographic c-axis texture [19]. So, with the increase of the overall Nd content, the alignment of the  $\text{Nd}_2\text{Fe}_{14}\text{B}$  grains becomes better, consequently remanence increases. Further increase of Nd content dilutes the hard magnetic  $\text{Nd}_2\text{Fe}_{14}\text{B}$  phase. So, remanence reduces. Consequently, a peak value of the remanence appears in the sample with medium Nd content.

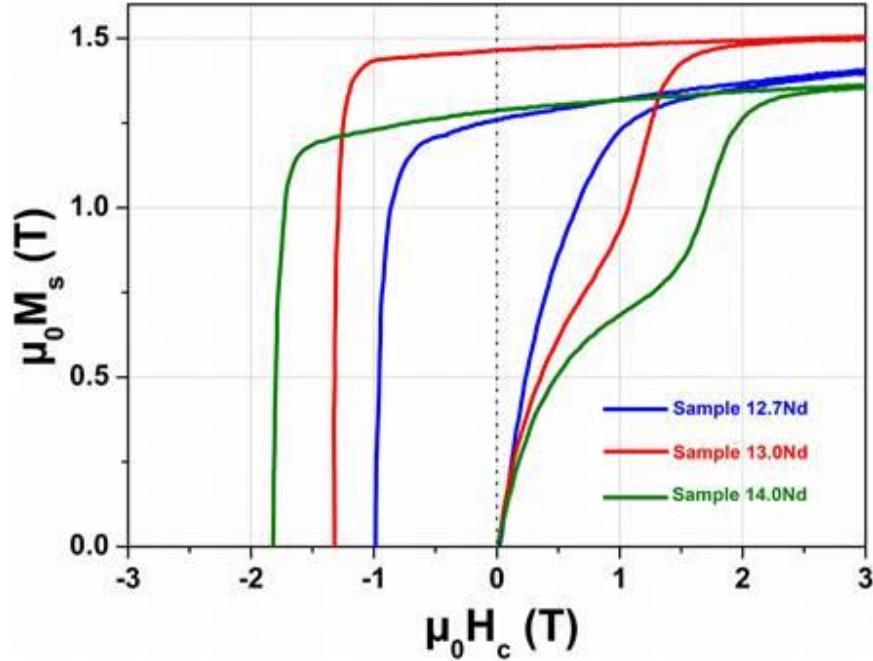


Figure 3.1 First and second quadrants of hysteresis loops for 12.7Nd, 13.0Nd, and 14.0Nd.

Figures 2.2a-c show the low magnification backscattered electron (BSE) scanning electron microscopy (SEM) images of (a) 12.7Nd, (b) 13.0Nd, and (c) 14.0Nd, respectively. C-axis is in-plane as the arrow indicates. The dark gray regions are the  $\text{Nd}_2\text{Fe}_{14}\text{B}$  phases, the small bright regions correspond to the Nd-rich phases, and the large bright regions result from the oxides that were present on the powder surface. By observing the contrast of the Nd-rich phase, we can determine its fraction to be quite low in 12.7Nd (Figure 2.2a); by increasing the concentration of the Nd element, the fraction of this phase increases (Figures 2.2b-c). The areal fraction of the Nd-rich phase can be estimated from the high magnification SEM images (Figures 2.2d-f). This value increases from 0.8% for 12.7Nd, to 2.2% for 13.0Nd, and reaches a maximum of around 8.8% for 14.0Nd. In addition, the contrast from the GB appears to be enhanced as the Nd content increases, and many thick grain boundaries can be seen in 14.0Nd. This suggests that a high content of the Nd element leads to the formation of continuous Nd-rich layers along the GBs. The average grain sizes of the samples are around 276 nm for 12.7Nd, 282 nm for 13.0Nd, and 191 nm for 14.0Nd. The different grain size is mainly because of the different hot-deformation temperature; i.e., 12.7Nd and 13.0Nd were hot-deformed at 850 °C while 14.0Nd was deformed at 775 °C. The lower deformation temperature suppressed material flow along GBs, thereby reducing the degree of (001) texture as shown in Figure 2.2f.

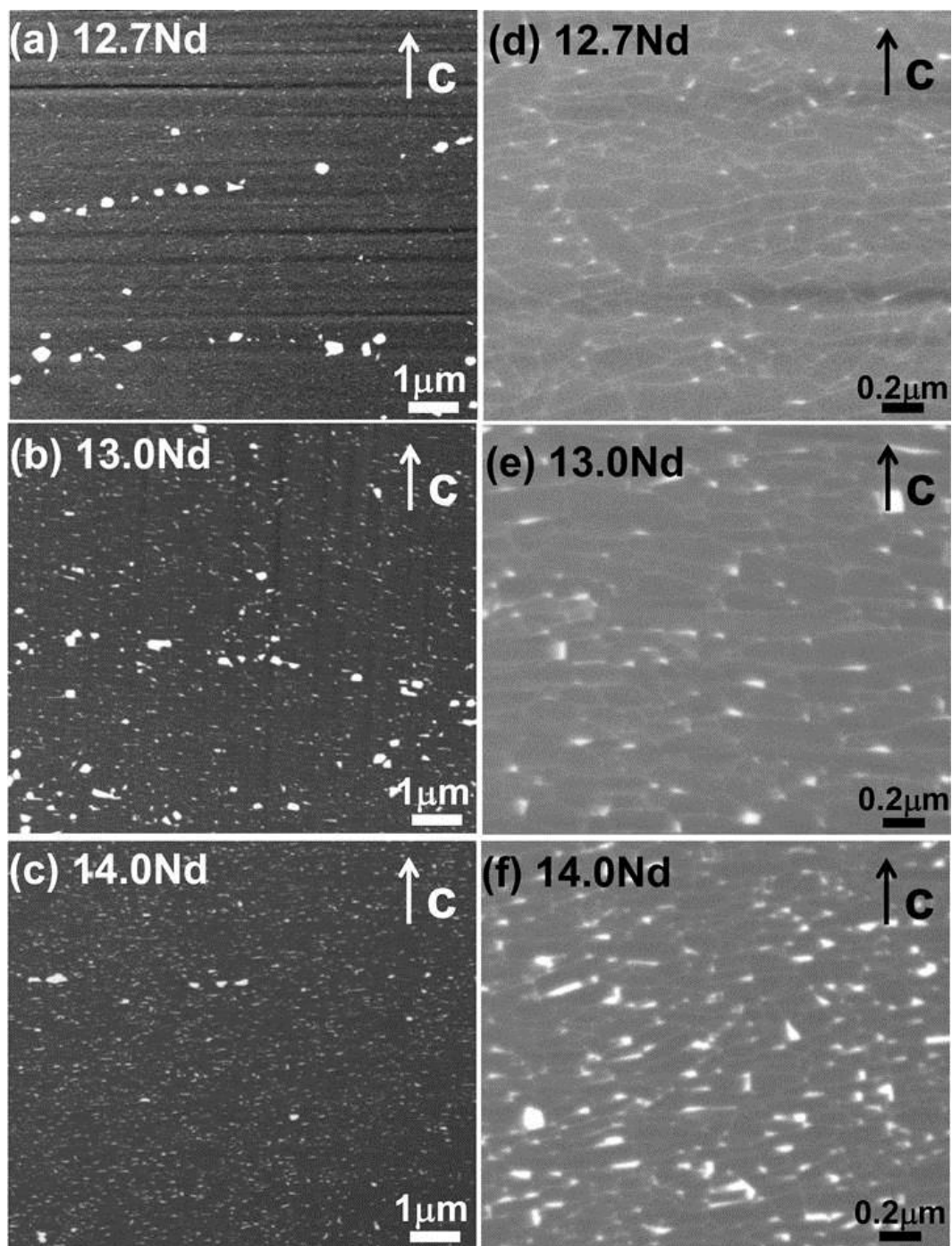


Figure 3.2 Low magnification cross-sectional BSE SEM images of (a) 12.7Nd, (b) 13.0Nd, and (c) 14.0Nd. High magnification cross-sectional BSE SEM images of (d) 12.7Nd, (e) 13.0Nd, and (f) 14.0Nd. C-axis is in-plane as the arrow indicates.

Figures 3.3a and b show the Lorentz TEM images of 12.7Nd and 14.0Nd in Fresnel mode in the thermally demagnetized state. The c-axis is out of plane, and the images are taken without applying magnetic fields. The maze structure can be seen in the Lorentz images of both samples. There is a bubble like domain structure in the larger  $\text{Nd}_2\text{Fe}_{14}\text{B}$  grains. Figures 3.3c and d show the Lorentz TEM images of 12.7Nd and 14.0Nd in which the c-axis is in-plane. The samples are in a thermally demagnetized state, and the Lorentz images are taken in the zero applied magnetic field. Stripe shaped domain walls can be seen in both figures and are marked with pairs of arrows in each figure. The dark and bright contrasts of the domain walls are produced by the opposite in-plane magnetization directions in neighboring domains. A comparison of in-plane and cross-sectional Lorentz images explains the status of the domain structure in the hot-deformed magnets in the thermally demagnetized state. The maze like domain structure in the c-plane and the stripe shaped pattern in the plane parallel to the c-axis can be seen in the anisotropic hot-deformed Nd-Fe-B magnets with large magnetocrystalline anisotropy. The maze like domain structure on the c-plane of the hot-deformed magnets is to minimize the internal stray field energy due to the demagnetization field. On the other hand, the stripe shaped domains lying parallel to the easy axis in the plane are due to the large magnetostatic interaction among  $\text{Nd}_2\text{Fe}_{14}\text{B}$  grains. Figure 3.3c shows that the stripe shaped domain walls cross the thin grain boundaries in 12.7Nd. However, there are some domain walls which are discontinuous across some grain boundaries in 14.0Nd. This suggests that the domain wall cannot exist in some grain boundaries of 14.0Nd which might be due to the existence of a non-magnetic grain boundary phase. These two features can be seen more clearly in the enlarged images displayed in the inset of Figures 3.3c and d. To study the influence of the grain boundary against domain wall motion, a magnetic field was applied to the samples with an in-plane c-axis. Figures 3.3e and f show the Lorentz TEM image of 12.7Nd and 14.0Nd with the same applied magnetic field of 0.1 T, respectively. A comparison of Figures 3.3c and e shows that by applying a 0.1 T magnetic field to 12.7Nd, the domain walls move easily and the shape of domain walls change from the parallel stripes to a zigzag shape. This is an indication that the magnetic domain walls are pinned at the GBs. However, by applying the same magnetic field to the TEM foil prepared from 14.0Nd, there is no significant movement of the domain walls (Figure 3.3f), which can be due to the stronger pinning strength of the GBs of 14.0Nd against the domain wall motion. The pinning field is apparently larger than 0.1 T.

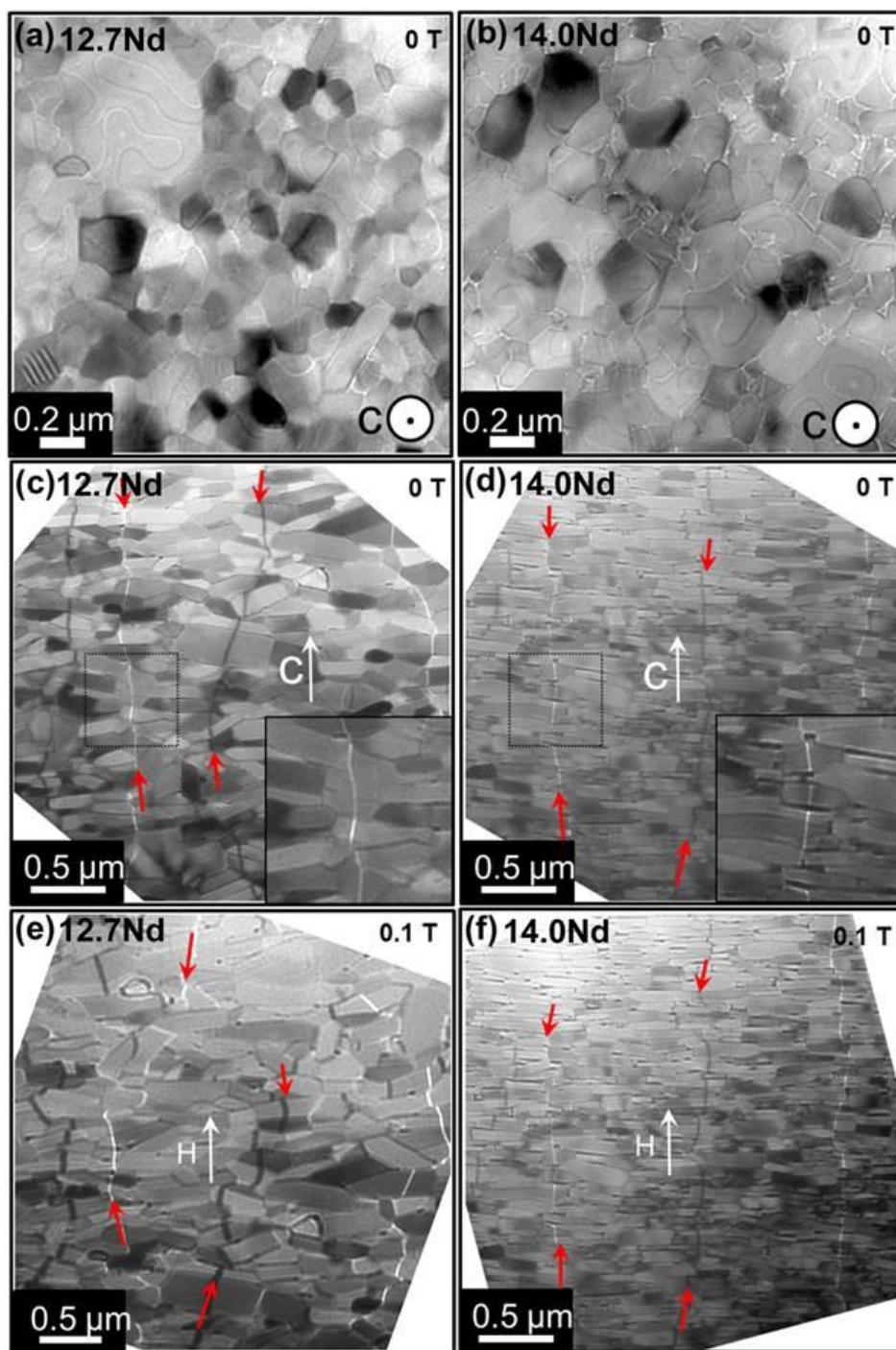


Figure 3.3 Plan view Lorentz TEM images in Fresnel mode of (a) 12.7Nd and (b) 14.0Nd in the 0 applied magnetic field. Cross-sectional view Lorentz TEM images of (c) 12.7Nd and (d) 14.0Nd in the 0 applied magnetic field. Cross-sectional view Lorentz TEM images of (e) 12.7Nd and (f) 14.0Nd in the applied magnetic field of 0.1 T from the same region as (c) and (d), respectively.

Figures 3.4 and 3.5 show the STEM-EDS analyses of 12.7Nd and 14.0Nd, respectively. In the HADDF images (Figures 3.4a and 3.5a), we can observe the plate like anisotropic grains with a size of around 300 nm in the lateral direction, which is very close to the single domain size of the  $\text{Nd}_2\text{Fe}_{14}\text{B}$  phase of around 250 nm [25]. Elemental mappings for Nd-L, Fe-K, and Ga-K taken from the same region in the two samples are shown in Figure 3.4b-d and Figures 3.5b-d, respectively. An appreciable difference can be seen between the two samples by comparing the Nd mapping (Figures 3.4b and 3.5b). In 12.7Nd, the GBs are so thin that they become invisible in some regions. Therefore, there is a direct contact between two neighboring  $\text{Nd}_2\text{Fe}_{14}\text{B}$  grains, which can cause an exchange coupling of the hard grains. However, the contrast of the GBs in 14.0Nd is much stronger, suggesting a larger enrichment of Nd at the GBs. Moreover, there are many thick GBs and triple junction regions, which improve the isolation of the hard magnetic grains. The Ga mapping (Figure 3.4d) shows the same distribution behavior as that of Nd. Ga has been reported to be an effective additive to enhance the coercivity due to the better isolation of the hard magnetic grains and the pinning effect of the Ga-rich phase [26-28]. Another clear difference is the alignment of the  $\text{Nd}_2\text{Fe}_{14}\text{B}$  grains. A much better alignment can be observed in 14.0Nd due to high Nd content.

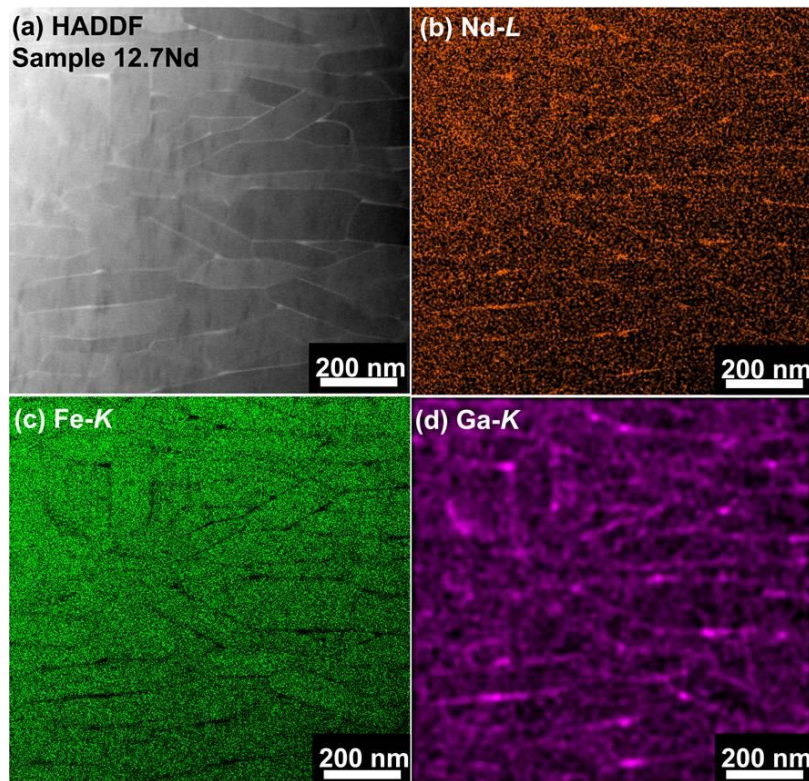


Figure 3.4 (a) HADDF image of 12.7Nd and STEM-EDS elemental mappings for (b) Nd-L, (c) Fe-K, and (d) Ga-K from the same region as (a).

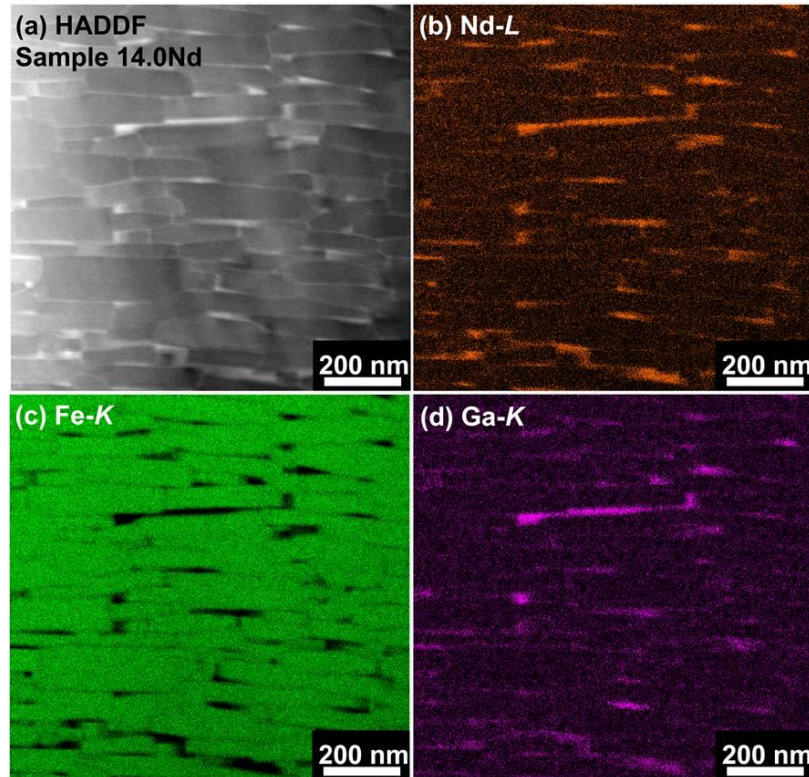


Figure 3.5 (a) HADDF image of 14.0Nd and STEM-EDS elemental mappings for (b) Nd-L, (c) Fe-K, and (d) Ga-K from the same region as (a).

Figures 3.6a-c show the typical high resolution TEM images of the grain boundaries of (a) 12.7Nd, (b) 13.0Nd, and (c) 14.0Nd, respectively. An Nd-rich phase with a thickness of  $\sim 0.8$  nm appears at the GB in 12.7Nd (Figure 3.6a). However, in some regions, there is no clear contrast of this phase from the GBs, and the lattice fringes from the two grains become diffused near the GB as shown in Figure 3.6d. Due to the lack of Nd, clear GBs cannot form in these regions, which causes exchange coupling between the grains. By increasing the Nd content, the GB thickness increases to  $\sim 1.4$  nm for 13.0Nd, and  $\sim 3.7$  nm for 14.0Nd (Figures 3.6b-c). The thickening of the GB phase is considered to be attributed to the excess Nd with respect to the stoichiometry composition of the  $\text{Nd}_2\text{Fe}_{14}\text{B}$  phase and has no correlations with the GB angle. The only possible place that the excess Nd can go to is the GBs or the triple junctions. Therefore, the thickening of the GB phase occurs. This thick GB phase can decouple the hard grains, which is essential for the coercivity enhancement [29,30]. However, note that such distinct GB phases are not observed in all the GBs, some are the same as those in 12.7Nd. Figures 3.6e-f show the HRTEM images of the triple junctions in 13.0Nd and 14.0Nd, respectively. The chemical composition of this phase is found to be  $\text{Nd}_{78.0}(\text{Fe}+\text{Co})_{20.6}\text{B}_{0.1}\text{Ga}_{1.3}$  by the three dimensional atom probe (3DAP) analysis.

Unlike sintered magnets [31], no oxygen is detected in this phase. The crystal structure of the Nd-rich triple junction phase is found to be a face-centered cubic with a lattice parameter of  $\sim 5.3 \text{ \AA}$  as shown in the inset figure of Figure 3.6e. Mishra also reported the same crystal structure phase with a similar composition [32]. As shown in the EDS mapping of 12.7Nd (Figure 3.4), we did not observe clear Nd-rich triple junctions in this sample due to the lean Nd content.

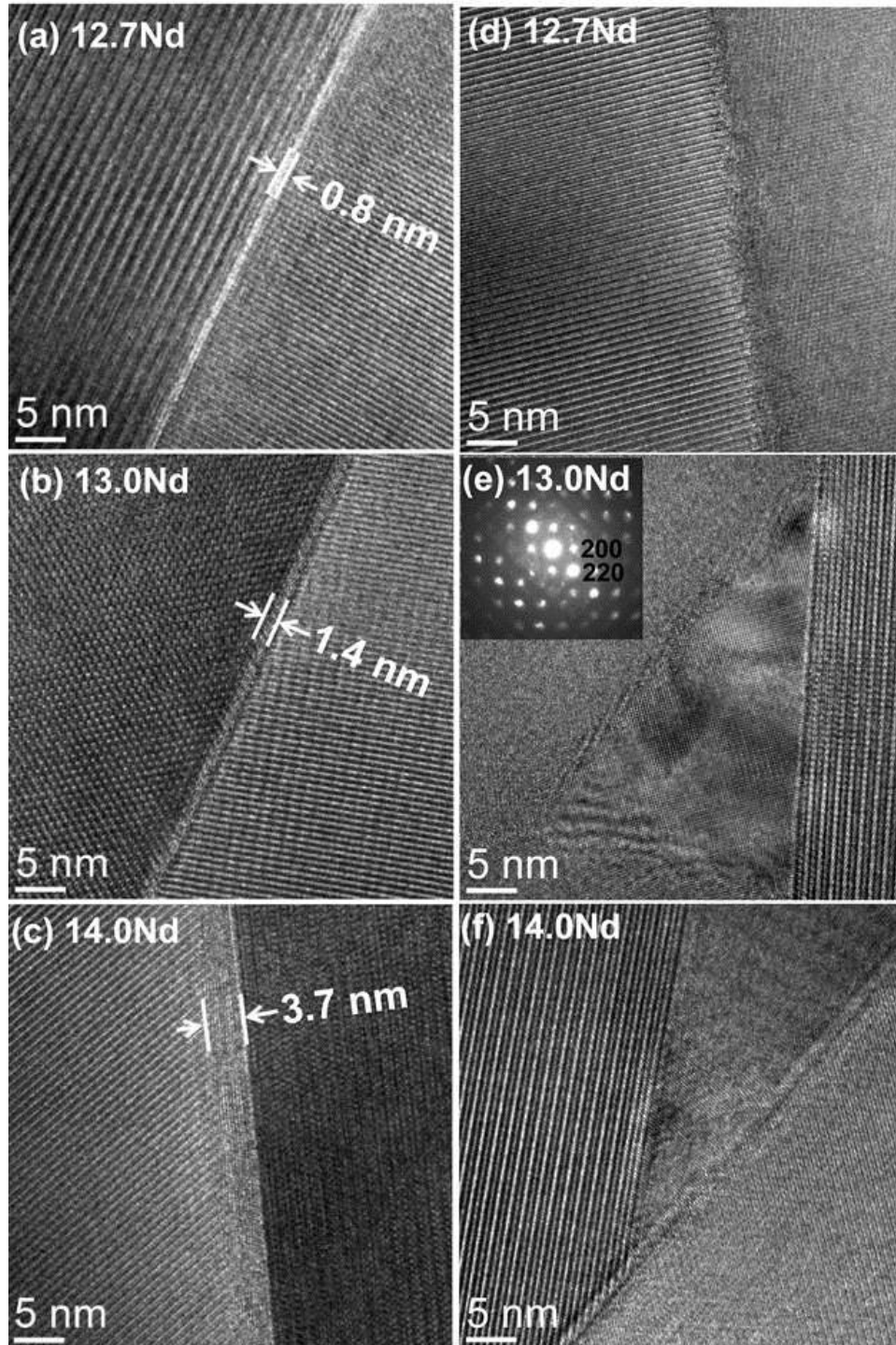


Figure 3. HRTEM images of the GBs from (a) 12.7Nd, (b) 13.0Nd, and (c) 14.0Nd. (d) HRTEM image of GB taken from 12.7Nd shows the lattice fringes from the two grains diffuses near the GB. HRTEM images of the triple junctions from (e) 13.0Nd, and (f) 14.0Nd. The Nanobeam diffraction pattern from the triple junction of 13.0Nd is shown as an inset figure in (e).

The lateral spatial resolution of three dimensional atom probe analysis is influenced by the trajectory aberration. When the GBs which lie nearly perpendicular to the probe direction were selected for quantitative analysis of the concentration profiles, the spatial resolution in the depth direction does not exceed two monoatomic layers. Using this technique, the chemical composition of the GB phase can be estimated. Figure 3.7 shows the 3DAP maps of Nd and Ga obtained from  $^{127}\text{Nd}$ . The grain boundaries can be distinguished in the atom probe tomography since Nd and Ga are both enriched at the grain boundaries. The atom maps within the inset volume perpendicular to GB A are shown in Figure 3.7b and the composition profiles calculated from the selected volume are shown in Figure 3.7c. The chemical composition of the  $\text{Nd}_2\text{Fe}_{14}\text{B}$  grain is measured to be  $\text{Nd}_{12.3}(\text{Fe}+\text{Co})_{81.9}\text{B}_{5.8}$  and shows good agreement with the stoichiometric composition of the  $\text{Nd}_2\text{Fe}_{14}\text{B}$  phase,  $\text{Nd}_{11.8}\text{Fe}_{82.4}\text{B}_{5.8}$ , suggesting that the atom probe analysis provides quantitative results. The compositions of the GBs marked as A, B, C, and D in Figure 3.7a are summarized in Table 3.1. The average amount of Nd and (Fe+Co) at the GB is around 22.6 at.% and 70.8 at.%, respectively. A depletion of Fe can be seen at the GB. However, there is a uniform distribution of Co across the GB, meaning that the distribution of Fe and Co is not always the same. Note that no oxygen is detected from the GB, suggesting that the GB phase is an oxygen-free metallic Nd-rich phase with a substantial amount of ferromagnetic elements (Fe +Co).

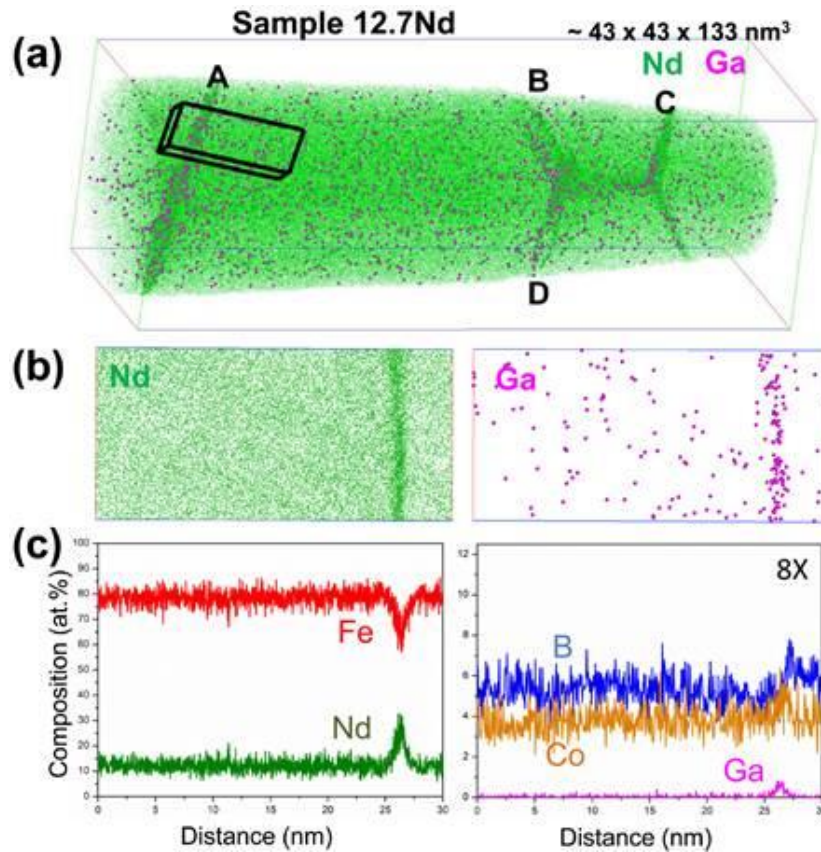


Figure 3.7 (a) 3DAP maps of Nd and Ga of 12.7Nd, and the grain boundaries are marked as A, B, C, and D respectively, (b) atom probe maps of Nd, and Ga of selected volume perpendicular to GB A, (c) concentration depth profiles for Fe, Nd, B, Co, and Ga determined from 3DAP analysis shown in (b).

Table 3.1. Chemical compositions of the different grain boundaries of Figure 3.7 from 12.7Nd.

GB	Chemical composition
A	$\text{Nd}_{25.6}(\text{Fe}+\text{Co})_{70.0}\text{B}_{3.8}\text{Ga}_{0.6}$
B	$\text{Nd}_{20.7}(\text{Fe}+\text{Co})_{73.6}\text{B}_{5.5}\text{Ga}_{0.2}$
C	$\text{Nd}_{21.0}(\text{Fe}+\text{Co})_{70.1}\text{B}_{8.7}\text{Ga}_{0.2}$
D	$\text{Nd}_{23.6}(\text{Fe}+\text{Co})_{69.5}\text{B}_{6.7}\text{Ga}_{0.2}$

Atom probe tomography taken from 13.0Nd is shown in Figure 3.8a. Figure 3.8b shows the Nd and Ga maps within the inset volume perpendicular to GB B. The composition profiles are calculated from the inset box and the results are shown in Figure 3.8c. The Nd element is enriched to around 30 at.%

at the GB phase, and the concentration of ferromagnetic elements (Fe+Co) is around 61 at.%. The chemical compositions of GBs A, B, C, and D in Figure 3.8a are summarized in Table 3.2. The Nd concentration varies from 21.1 to 30.0 at.% in different GBs, and the average value is higher than that of 12.7Nd.

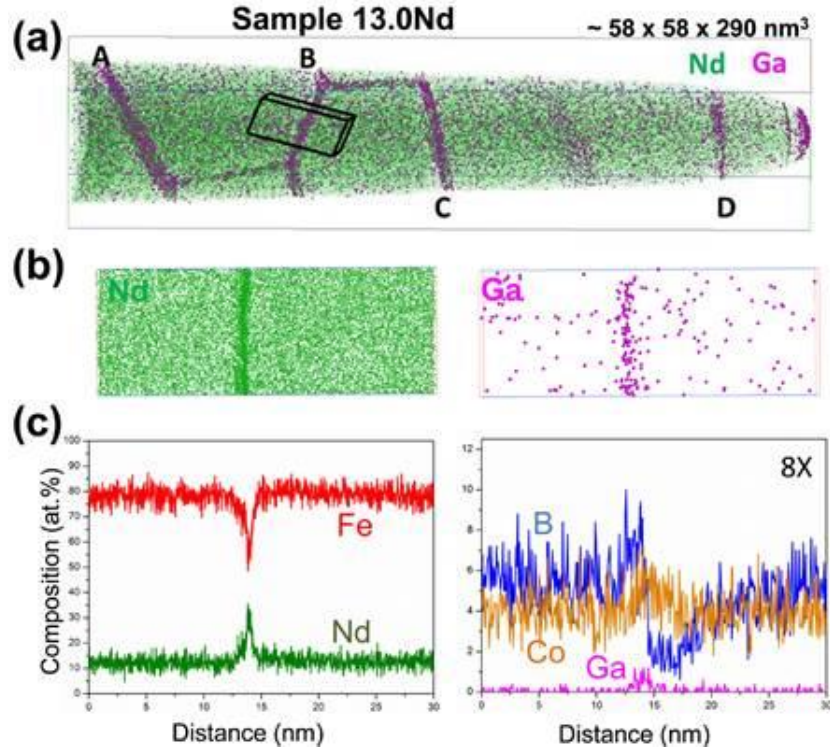


Figure 3.8 (a) 3DAP maps of Nd and Ga of 13.0Nd, and the grain boundaries are marked as A, B, C, and D respectively, (b) atom probe maps of Nd, and Ga of selected volume perpendicular to GB B, (c) concentration depth profiles for Fe, Nd, B, Co, and Ga determined from 3DAP analysis shown in (b).

Table 3.2 Chemical compositions of the different grain boundaries of Figure 3.8 from 13.0Nd.

GB	Chemical composition
A	$\text{Nd}_{24.6}(\text{Fe}+\text{Co})_{68.9}\text{B}_{6.1}\text{Ga}_{0.4}$
B	$\text{Nd}_{30.0}(\text{Fe}+\text{Co})_{61.1}\text{B}_{8.1}\text{Ga}_{0.8}$
C	$\text{Nd}_{21.1}(\text{Fe}+\text{Co})_{70.9}\text{B}_{7.6}\text{Ga}_{0.4}$
D	$\text{Nd}_{28.7}(\text{Fe}+\text{Co})_{64.0}\text{B}_{6.6}\text{Ga}_{0.7}$

Figure 3.9 shows the atom probe tomography obtained from 14.0Nd. The amount of Nd at the GB is around 51 at.%, which is substantially higher than that of a typical sintered Nd-Fe-B magnet of around 30 at.% [33]. The concentration of the ferromagnetic elements (Fe+Co) in the GB decreases dramatically. Therefore, the GB may become non-ferromagnetic. The compositions of the GBs marked as A, B, and C in Figure 3.9a are summarized in Table 3.3. The average concentration of Nd is around 46 at.% at the GB, which is much higher than that of the first two samples. On the other hand, the enrichment of Ga can be found at the GB. This improves the isolation of the grains and enhances the pinning force [26-28].

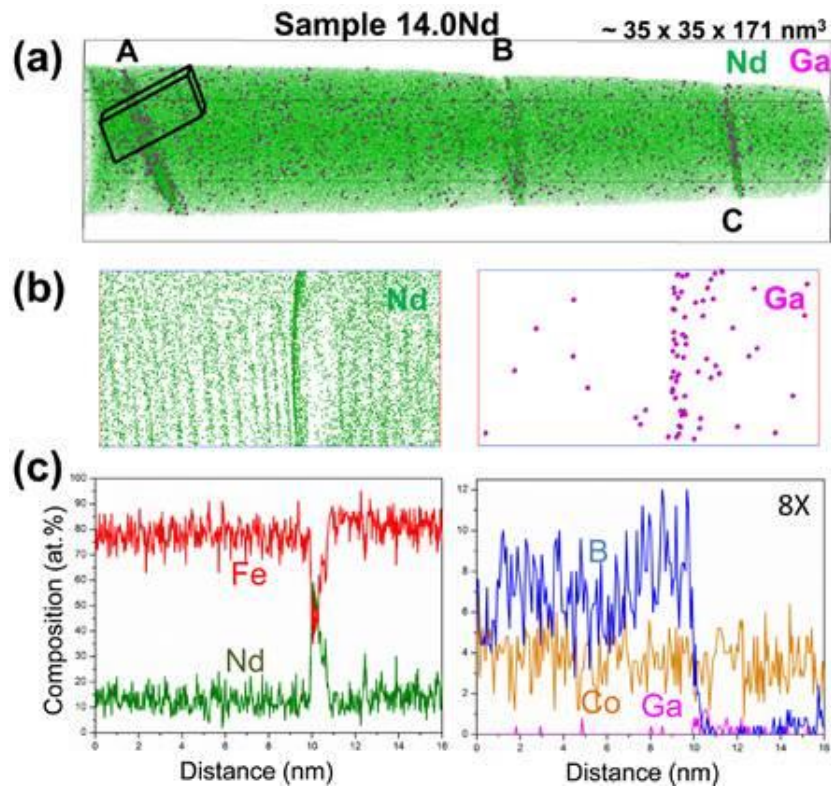


Figure 3.9 (a) 3DAP maps of Nd and Ga of 14.0Nd, and the grain boundaries are marked as A, B, and C respectively, (b) atom probe maps of Nd, and Ga of selected volume perpendicular to GB A, (c) concentration depth profiles for Fe, Nd, B, Co, and Ga determined from 3DAP analysis shown in (b).

Table 3.3 Chemical compositions of different grain boundaries of Figure 3.9 from 14.0Nd.

GB	Chemical composition
A	$\text{Nd}_{51.1}(\text{Fe}+\text{Co})_{45.3}\text{B}_{2.2}\text{Ga}_{1.4}$
B	$\text{Nd}_{43.2}(\text{Fe}+\text{Co})_{54.1}\text{B}_{2.0}\text{Ga}_{0.7}$
C	$\text{Nd}_{43.8}(\text{Fe}+\text{Co})_{48.1}\text{B}_{6.8}\text{Ga}_{1.3}$

According to the 3DAP measurements, we summarize the average Nd content of the three samples at the GB and correlates it with the coercivity as shown in Figure 3.10. There is a clear correlation between the Nd content at the grain boundaries and the coercivity. Since the magnetization of the GB phase is expected to decrease as the Nd concentration increases as shown in Figure 3.11, Figure 3.10 also indicates that the coercivity increases as the magnetization of the GB phase decreases.

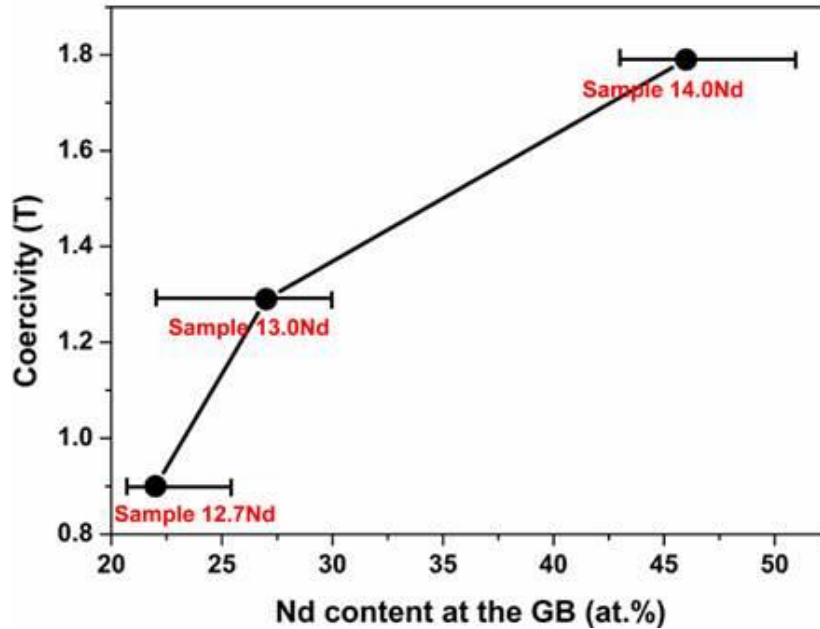


Figure 3.10. Correlation between the Nd content at the GB calculated from 3DAP measurements and coercivity.

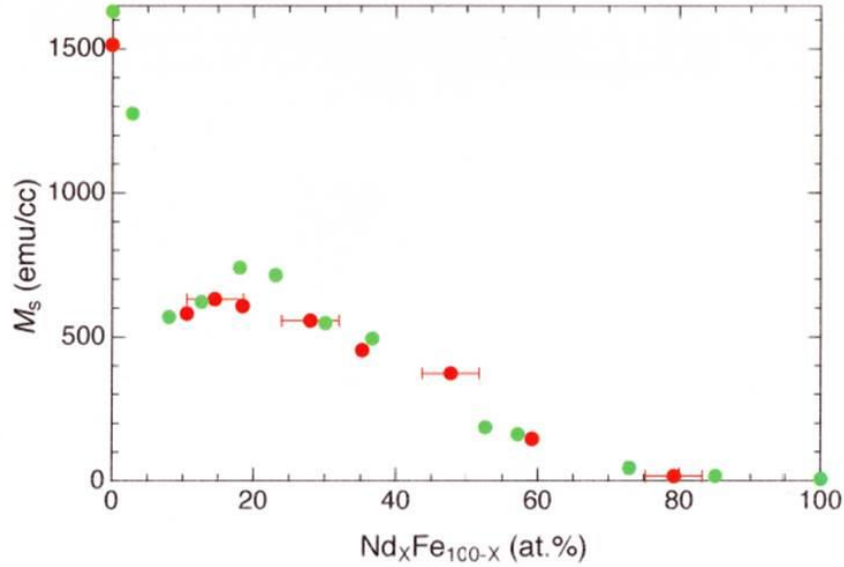


Figure 3.11 Magnetization of  $\text{Nd}_x\text{Fe}_{100-x}$  (Courtesy of Professor T. Shima)

Figure 3.12a shows the finite element model with the cuboid shaped  $\text{Nd}_2\text{Fe}_{14}\text{B}$  grains and the applied meshes. The easy axis for the  $\text{Nd}_2\text{Fe}_{14}\text{B}$  grains are parallel to the Z direction with a random deviation between 0 and  $\pm 15^\circ$  in the simplified model based on the present microstructure study. The external magnetic field is applied parallel to the Z axis. The atom probe results show that the chemistry of the Nd-rich grain boundary phase changes from  $\sim 20$  at.% Nd for 12.7Nd to  $\sim 50$  at.% Nd for 14.0Nd. Hence, we can assume that with the enrichment of Nd at the (Fe+Co) based GB phase, the magnetization of this phase becomes lower than that of pure Fe. Therefore, we change the magnetization of the grain boundary phase from 1.2 T to 0.0 T to examine the influence of the GB phase magnetization on the magnetization reversal process. Figure 3.12b shows the demagnetization curves from the modeled samples with the GB phase magnetization of 0.0, 0.4, 0.8, and 1.2 T. By reducing the magnetization of the GB phase from 1.2 T to 0.8, 0.4, and 0.0 T, the coercivity value increases, suggesting that the magnetization of the GB phase has a strong influence on the coercivity. Figures 3.12c and d show the magnetization configuration of the modeled samples with the GB magnetization of 1.2 T and 0.0 T during the demagnetization process at  $\mu_0 H_{\text{ext}} = 2.65$  T and 3.75 T, which are the nucleation fields for both samples. This result shows that for the sample containing the ferromagnetic GB phase, nucleation starts in a much lower magnetic field than the sample containing a non-magnetic GB phase. In these two figures, the red and blue contrasts indicate the direction of the magnetization in the +Z and -Z directions. Figure 3.11c shows that the nucleation starts at the triple junction of the sample containing the ferromagnetic GB phase and can propagate to the neighboring grains as nucleation starts. However, for the sample

containing a non-magnetic grain boundary phase (Figure 3.11d), the nucleation starts at the triple junction of the  $\text{Nd}_2\text{Fe}_{14}\text{B}$  grain, at the interface of the GB phase with  $\text{Nd}_2\text{Fe}_{14}\text{B}$  grains. However, the existence of a non-magnetic GB phase can hinder the propagation of a reversed domain to the neighboring grain, which is the main reason for achieving a higher coercivity than that of the sample with a ferromagnetic GB phase.

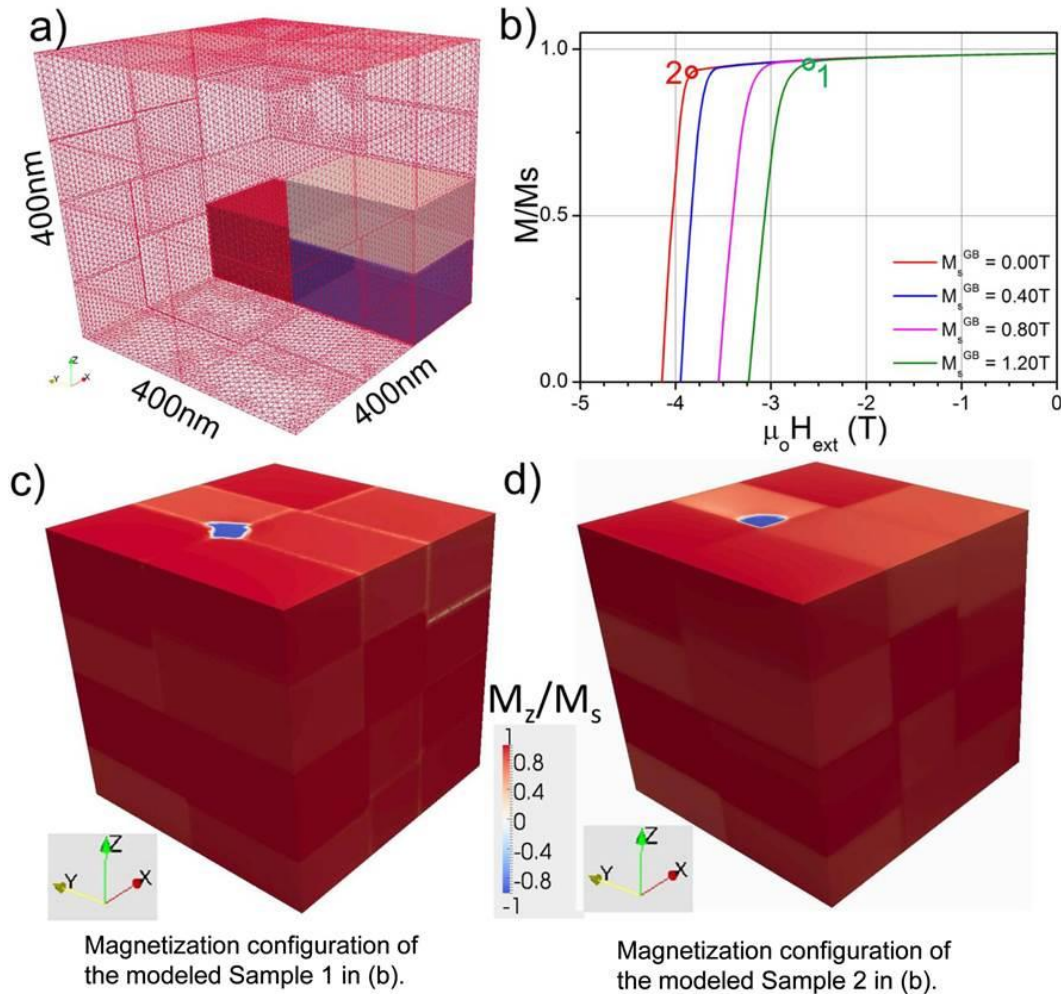


Figure 3. 12. (a) The microstructure of the finite element model with the applied meshes. The cuboid  $\text{Nd}_2\text{Fe}_{14}\text{B}$  grains are shown in different colors to make the individual grain clearly. (b) Magnetization reversal curves of the simulated samples in which the saturation magnetization of the grain boundary phase varies from 0.0 T to 1.2T. (c) The magnetization configuration of the modeled Sample 1 in (b) with GB magnetization of 1.2 T during reversal at  $\mu_0 H_{\text{ext}} = 2.65\text{T}$ . (d) The magnetization configuration of the modeled Sample 2 in (b) with GB magnetization of 0.0 T during reversal at  $\mu_0 H_{\text{ext}} = 3.75\text{T}$ . (Courtesy of Dr. H. Sepehri-Amin)

### 3.4 Discussion

As shown in Figure 3.1, the coercivity of the hot-deformed Nd-Fe-B increases as the overall Nd concentration of the alloys increases. The steep rise of the initial magnetization curve for 12.7Nd suggests that the domain walls are free to move and there is no strong pinning force for domain wall motion. This was proven by the domain wall movement in the Lorentz TEM observation in Figures 3.3c and e. The lower remanence irrespective of the lower Nd content is due to the lower degree of c-axis alignment as seen in Figure 3.2a and Figure 3.4. Due to the lean Nd content at the GB, the material flow along the GB for 12.7Nd is much more difficult than those of the others. The S-shape of the initial magnetization curves for 13.0Nd and 14.0Nd indicate a more complicated heterogeneous magnetization process. The domain wall displacements within the grains initially lead to a rapid rise of magnetization at a low magnetic field, thereby giving rise to the large susceptibility. Then they are pinned at the GBs, leading to partial magnetization by the free domain wall displacement. When a magnetic field higher than the pinning force is applied, the remaining magnetic reversal occurs by the depinning of the magnetic domain walls. The depinning field of the domain walls increases as the Nd-concentration in the GB phase increases. This can be understood from the atom probe result that the GB chemistry and the coercivity have a clear correlation (Figure 3.10).

BSE SEM and TEM results show that the microstructure of the GB changes by increasing the Nd content. There are very thin and discontinuous Nd-rich GBs in the low Nd content 12.7Nd. An HRTEM image of a GB in 12.7Nd shows a direct contact of two  $\text{Nd}_2\text{Fe}_{14}\text{B}$  grains at the GB (Figure 3.6d). The  $\text{Nd}_2\text{Fe}_{14}\text{B}$  grains must be exchange coupled, thus the magnetic domain would extend continuously to neighboring grains. By increasing the Nd content, the excess Nd element is rejected to the GBs, and a distinct Nd-rich layer is observed along the GB. This would cause a weaker ferromagnetic exchange among the  $\text{Nd}_2\text{Fe}_{14}\text{B}$  grains. Meanwhile, the coercivity can be improved by increasing the thickness of the Nd-rich layers in the GB [34]. The excess Nd also causes the smoothening of the interface, removing the local demagnetization field that may trigger the nucleation of a reversal domain.

A comparison of the chemical composition of the GBs shows that the concentration of Nd in the GBs is distinctly different among the three samples. The 3DAP results of 12.7Nd show that more than 70 at.% of the GB phase is composed of ferromagnetic elements; therefore, the GB phase is likely to be ferromagnetic as reported by Sepehri-Amin et al. [33]. As we have expected, the amount of Nd at the GBs in 14.0Nd is around 46 at.%, which is substantially higher than that in the other two samples. In such a case, the domain wall would be pinned strongly at the GBs, since its magnetocrystalline anisotropy is much smaller than that of the  $\text{Nd}_2\text{Fe}_{14}\text{B}$  grains. The pinning force for the magnetic domain wall motion at the GB is proportional to  $(KW/\delta_0)(A/A_D - K_D/K)$ , where  $K$  and  $K_D$  are the magnetocrystalline anisotropies of  $\text{Nd}_2\text{Fe}_{14}\text{B}$  and the GB phases, respectively,  $A$  and  $A_D$  are the exchange energy of the  $\text{Nd}_2\text{Fe}_{14}\text{B}$  and the

GB phases, respectively,  $W$  is the thickness of the GB phase, and  $\delta_0$  is the domain wall width [35]. According to the 3DAP results, by increasing the Nd content from 12.7Nd to 14.0Nd, the Nd concentration in the GB increases and the (Fe+Co) concentration decreases. Therefore,  $A_D$  and  $K_D$  will be reduced. In addition, the thickening of the GBs has been observed from the HRTEM image, thus  $W$  in the above formula increases. Hence, both would cause the enhancement of the pinning strength of the GB against domain wall motion.

The micromagnetic simulation results show that the existence of a ferromagnetic GB phase with reduced magnetocrystalline anisotropy causes the nucleation of reversed domains at the triple junctions at a low magnetic field. Thereafter, the reversed domain can propagate easily to all the neighboring grains and the GB phase has a weak pinning effect against the domain wall motion. However, by changing the chemistry of the GB phase to a non-magnetic phase, the required field for the nucleation of reversed magnetic domains during the magnetization reversal process increases. After the nucleation of the reversed domains, the existence of a non-magnetic GB phase can hinder the propagation of the reversed domains to the neighboring grains since the domain wall cannot cross the non-magnetic GB phase which would lead to coercivity enhancement.

The present work has shown that the reason for the enhanced coercivity in the Nd-rich hot-deformed magnets is the higher concentration of Nd in the GB phase. As the excess Nd content in the alloys increases, the volume fraction of the triple junction Nd-rich phase also increases. Note that the majority of the triple junction Nd-rich phases in the sintered magnets are Nd oxides such as fcc-NdO<sub>x</sub> and Nd<sub>2</sub>O<sub>3</sub> [31]; however, the triple junction phase in the hot-deformed magnet is metallic fcc-Nd free from oxygen. The Nd-concentration in the GB in 14.0Nd is about 40%, which is higher than the typical value for the GB phase in sintered magnets [31]. A recent work on the Nd-Cu diffusion process applied to hot-deformed anisotropic magnet reported a coercivity of  $\mu_0 H_c \sim 2.2$  T. By increasing the Nd content in the hot-deformed magnets, higher coercivity will be achievable at the expense of remanence.

The Lorenz microscopy shows that the stripe shaped magnetic domains are much larger than the grain size and contain a number of grains despite the presence of the Nd-rich grain boundary phase as shown in Fig. 3. Noted that the domain walls in 12.7Nd are continuous through the Nd-rich GB phase, but the domain walls in 14.0Nd disappear in the Nd-rich GB phase. This suggests that the Nd-rich GB phase in 14.0Nd is paramagnetic. Nevertheless, magnetic domains do not correspond with the Nd<sub>2</sub>Fe<sub>14</sub>B grain. This suggests that the Nd<sub>2</sub>Fe<sub>14</sub>B grains are magnetostatically coupled to form a large magnetic domain even if the grain size becomes smaller than the single domain size which is exchange decoupled by the presence of a nonmagnetic GB phase.

### 3.5 Summary

The coercivity of hot-deformed Nd-Fe-B magnets was enhanced to 1.79 T by increasing the Nd content. The pinning mechanism plays a dominant role in determining the coercivity. The areal fraction of the Nd-rich phase increased in the high Nd content sample. The excess Nd also led to the formation of a thick distinct Nd-rich phase along the GB. This would promote a magnetic isolation of the hard grains. The 3DAP analysis showed a clear increase in the Nd content and a decrease in the Fe and Co content in the GB, which would cause an enhanced pinning force against the domain wall motion, resulting in high coercivity. Micromagnetic simulation results showed that the change in the magnetization of the grain boundary phase to a non-magnetic phase by chemistry modification can have two main influences on the magnetization reversal process; first preventing the nucleation of reversed domains at a low magnetic field and second, hindering the propagation of reversed magnetic domain walls to the neighboring grains which are both contributing to the coercivity enhancement.

## Reference

- [1] R.W. Lee, Applied Physics Letter, 46, 790 (1985).
- [2] R.W. Lee, E.G. Brewer, N. A. Schaffel, IEEE Transactions on Magnetics, MAG-21,1958 (1985).
- [3] J.J. Croat, J.F. Herbst, R.W. Lee, F.E. Pinkerton, Applied Physics Letter, 44, 148 (1984).
- [4] J.J. Croat, J.F. Herbst, R.W. Lee, F.E. Pinkerton, Journal of Applied Physics, 55, 2078 (1984).
- [5] R.K. Mishra, T.Y. Chu, L.K. Rabenberg, Journal of Magnetism and Magnetic Materials, 84, 88 (1990).
- [6] R.K. Mishra, E.G. Brewer, R.W. Lee, Journal of Applied Physics, 63, 3528 (1988).
- [7] T.Y. Chu, L.K. Rabenberg, R.K. Mishra, Journal of Applied Physics, 69, 6046 (1991).
- [8] J. Liu, H. Sepehri-Amin, T. Ohkubo, K. Hioki, A. Hattori, T. Schrefl, K. Hono, Acta Materialia, 61, 5387 (2013).
- [9] H. Sepehri-Amin, Y. Une, T. Ohkubo, K. Hono, M. Sagawa, Scripta Materialia, 65, 396 (2011).
- [10] F. Vial, F. Joly, E. Nevalainen, M. Sagawa, K. Hiraga, K.T. Park, Journal of Magnetism and Magnetic Materials, 242, 1329 (2002).
- [11] T.G. Woodcock, O. Gutfleisch, Acta Materialia, 59, 1026 (2011).
- [12] A. Kirchner, J. Thomas, O. Gutfleisch, D. Hinz, K.H. Müller, L. Schultz, Journal of Alloys and Compounds, 365, 286 (2004).
- [13] L.H. Lewis, Y. Zhu, and D.O. Welch, Journal of Applied Physics, 76, 6235 (1994).
- [14] T.D. Nguyen, K.M. Krishnan, L.H. Lewis, Y. Zhu, D.O. Welch, Journal of Applied Physics, 79, 4848 (1996).
- [15] V.V. Volkov, Y. Zhu, Journal of Applied Physics, 85(6), 3254 (1999).
- [16] H. Sepehri-Amin, T. Ohkubo, T. Nishiuchi, S. Hirosawa, K. Hono, Scripta Materialia 62, 1124 (2010).
- [17] S. Sugimoto, H. Nakamura, K. Kato, D. Book, T. Kagotani, M. Okada, M. Homma, Journal of Alloys and Compounds, 293, 862 (1999).
- [18] W.B. Cui, Y.K. Takahashi, K. Hono, Acta Materialia, 59, 7768 (2011).
- [19] R.K. Mishra. J Mater Eng 11, 87 (1989).
- [20] R. Shioi, H. Miyawaki, T. Morita, Denki Seiko, 82, 31 (2011).
- [21] M. Sagawa, S. Fujimura, H. Yamamoto, Y. Matsuura, S. Hirosawa, Journal of Applied Physics, 57, 4094 (1985).

- [22] T. Schrefl, J. Fidler, *Journal of Applied Physics*, 83, 6262 (1998).
- [23] O. Gutfleisch, D. Eckert, R. Schäfer, K.H. Müller, V. Panchanathan, *Journal of Applied Physics*, 87, 6119 (2000).
- [24] M. Gronefeld, H. Kronmüller, *Journal of Magnetism and Magnetic Materials*, 88, L267 (1990).
- [25] J.D. Livingston, *Journal of Applied Physics*, 57, 4137 (1985).
- [26] H. Sepehri-Amin, W.F. Li, T. Ohkubo, T. Nishiuchi, S. Hirosawa, K. Hono, *Acta Materialia*, 58, 1309 (2010).
- [27] I. Ahmad, H.A. Davies, R.A. Buckley, *Materials Letter*, 20, 139 (1994).
- [28] D.T. Steel, M. Leonowicz, H.A. Davies, *Materials Letter*, 23, 43(1995).
- [29] H. Sepehri-Amin, T. Ohkubo, K. Hono, *Journal of Applied Physics*, 107, 09A745 (2010).
- [30] O. Gutfleisch, A. Bollero, A. Handstein, D. Hinz, A. Kirchner, A. Yan, K.H. Müller, L. Schultz, *Journal of Magnetism and Magnetic Materials*, 242, 1277 (2002).
- [31] W.F. Li, T. Ohkubo, K. Hono, *Acta Materialia*, 57, 1337 (2009).
- [32] R.K. Mishra, *Journal of Applied Physics*, 62, 967 (1987).
- [33] H. Sepehri-Amin, T. Ohkubo, T. Shima, K. Hono, *Acta Materialia*, 60, 819 (2012).
- [34] J.M. González, F. Cebollada, A. Hernando, *Journal of Applied Physics*, 73, 6943 (1993).
- [35] D.L. Paul, *Journal of Applied Physics*, 53, 1649 (1982).

# Chapter 4. The grain size dependence of coercivity of hot-deformed Nd-Fe-B magnets

## 4.1 Introduction

The reasons for the coercivity enhancement of the hot-deformed Nd-Fe-B magnets by increasing Nd content were explained in Chapter 3 to be the formation of the distinct grain boundary phase and high concentration of nonmagnetic element Nd at the grain boundary. Based on this result, the grain boundary diffusion process by introducing the Nd-transmission metal eutectic alloys such as Nd-Cu alloys into the grain boundary layer was proposed and employed on the hot-deformed processed magnets. When the magnets coated with Nd-Cu flakes were annealed at  $\sim 700\text{ }^\circ\text{C}$ , the Nd-Cu melts and diffuses into the magnets through GBs. As a result, the thickness of the GBs increases and microstructural isolation of the  $\text{Nd}_2\text{Fe}_{14}\text{B}$  phase becomes better as shown in Figure 4.1 [1-2]. In addition, the composition profiles measured by three dimensional atom probe (3DAP) indicate an almost completed depletion of ferromagnetic element Fe+Co in the grain boundary of the diffused magnets [1]. However, the coercivity is only 2.3 T, still lower than 2.5 T.

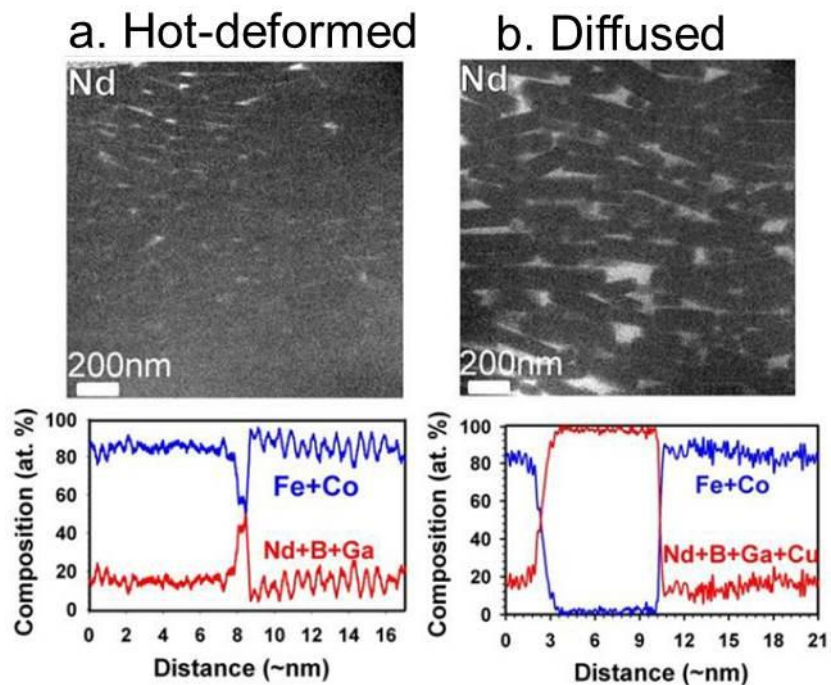


Figure 4.1 BSE SEM images and composition profile of grain boundary of (a) hot-deformed and (b) diffused Nd-Fe-B magnets [1].

It is known that besides the composition of the grain boundaries, the coercivity of Nd-Fe-B magnets is also strongly influenced by the grain size [3-5]. Recently, Hioki et al. reported that both the coercivity and thermal stability of coercivity can be improved by decreasing the average grain size [6]. Sepehri-Amin et al. demonstrated the decrease in the grain size of the anisotropic Nd-Fe-B magnets reduces the local demagnetization factor by using micromagnetic simulations [7]. Hence, if ultrafine  $\text{Nd}_2\text{Fe}_{14}\text{B}$  grains are better isolated by the presence of nonferromagnetic intergranular phase, much higher coercivity of above 2.5 T may be attained, which is comparable to that of Dy-containing sintered magnets. In fact, a high coercivity value of 2.95 T was achieved in a modeled microstructure that the elongated single domain sized  $\text{Nd}_2\text{Fe}_{14}\text{B}$  grains was magnetically isolated by the diffusion process of Nd-Ag capping layer [8]. The grain size is much smaller in this case compared to the real Nd-Fe-B magnets. In this study, the microstructure and magnetic properties of the hot-deformed Nd-Fe-B magnets with different grain sizes manufactured from the identical alloy composition at different processing temperatures were investigated to understand the microstructure-coercivity relationships. The microstructure was thoroughly characterized by scanning electron microscopy (SEM), transmission electron microscopy (TEM), and three dimensional atom probe (3DAP), and the origin of the coercivity is discussed based on finite element micromagnetic simulations and micromagnetic analysis of the experimentally observed microstructures.

## 4.2 Experiment

The nominal composition of the melt-spun ribbons used in this work was  $\text{Nd}_{13.5}\text{Fe}_{76.7}\text{Co}_{3.4}\text{B}_{5.6}\text{Ga}_{0.5}\text{Al}_{0.3}$  in atomic percent or  $\text{Nd}_{29.8}\text{Fe}_{65.6}\text{Co}_{3.1}\text{B}_{0.9}\text{Ga}_{0.5}\text{Al}_{0.1}$  in weight percent. Flakes produced by crushing the melt-spun ribbons were hot-pressed into a fully dense magnet at 750 ~ 800 °C in vacuum. The consolidated bulks were subsequently hot-deformed in an Ar atmosphere at different temperatures of 750, 775, 800, 825, 850, 875, and 900 °C with a strain rate of  $\sim 0.06 \text{ s}^{-1}$ . The magnetic properties of the samples were measured by a pulsed high field magnetometer and a BH loop tracer. Backscatter electron (BSE) SEM observations were made on the bulk samples using a Carl Zeiss CrossBeam 1540EsB at the acceleration voltage of 2.0 kV. TEM observations were performed using a Titan G2 80-200 TEM at the acceleration voltage of 200 kV. 3DAP analyses were conducted under ultrahigh vacuum  $< 10^{-8} \text{ Pa}$  at a base temperature of 25 K in the flux range of 0.003-0.01 atom/pulse with an UV laser (343 nm) using a laser power of  $\sim 0.12 \mu\text{J/pulse}$ .

The demagnetization process was studied using finite element micromagnetic simulations on a model microstructure containing platelet-shaped  $\text{Nd}_2\text{Fe}_{14}\text{B}$  grains with different sizes separated with the

intergranular phase with the thickness of 3 nm with various magnetizations. The models were  $300 \times 300 \times 300 \text{ nm}^3$  in size. The size of  $\text{Nd}_2\text{Fe}_{14}\text{B}$  grains was chosen as 60 and 150 nm in lateral direction and 30 and 75 nm in longitudinal direction, respectively. The saturation magnetization ( $\mu_0 M_s$ ), magnetocrystalline anisotropy ( $K_1$ ), and exchange stiffness ( $A$ ) of the  $\text{Nd}_2\text{Fe}_{14}\text{B}$  phase were chosen to be 1.61 T,  $4.3 \text{ MJ/m}^3$ , and  $12 \text{ pJ/m}$ , respectively [9]. The magnetocrystalline anisotropy ( $K_1$ ) of an intergranular phase was chosen to be  $0 \text{ MJ/m}^3$  for all the models. The saturation magnetization and exchange stiffness of the intergranular phase were varied from 1.20 T to 0.03 T and from  $12 \text{ pJ/m}$  to  $1.0 \text{ pJ/m}$ , respectively. Tetrahedron meshes with a size of 3.0 nm were applied for the intergranular phase. The Landau-Lifshitz-Gilbert (LLG) equation at each node was solved by the FEMME software [10].

## 4.3 Results

### 4.3.1 Magnetization behavior

Figure 4.2a shows the magnetization curves for the samples hot-deformed at different temperatures. The coercivity decreased from 1.91 T to 1.46 T by increasing the hot-deformation temperature. The shape of the initial magnetization curve, which shows two-step behavior, also changed with increasing the hot-deformation temperature. The initial magnetization with high susceptibility is believed to be due to the domain wall displacements within multi-domain grains, while the second magnetization at high field region is attributed to the magnetization reversal of the single domain grains [11]. The coercivity and nucleation field can be measured from the magnetization curves and the depinning field can be measured from the peak position of the first derivatives of the magnetization by magnetic field as shown in Figure 4.2a. Figure 4.2b is the plot of the measured coercivity, nucleation field, and depinning field versus the grain size of the hot-deformed magnets. The grain size of each sample was calculated based on the BSE SEM images. The figure shows that the  $\text{Nd}_2\text{Fe}_{14}\text{B}$  grain size in the lateral direction increased from  $210 \pm 40 \text{ nm}$  to  $970 \pm 220 \text{ nm}$  as the hot-deformation temperature increased. The coercivity, the nucleation field, and the depinning field show almost linear correlations. Figure 4.3c shows the absolute value of the temperature coefficient of coercivity ( $\beta = (\Delta H_c / H_c \Delta T) * 100\%$ ) as a function of the lateral grain size. The temperature coefficient is a very important parameter since the magnets are intended to be used at the elevated temperature, and the typical value for commercial Nd-Fe-B sintered magnets is around  $\sim 0.60\% / ^\circ\text{C}$ . Figure 4.2c shows that the absolute value of  $\beta$  increased from  $0.45\% / ^\circ\text{C}$  to  $0.50\% / ^\circ\text{C}$  with increasing grain size, which indicated that the thermal stability of coercivity improved as grain size decreased.

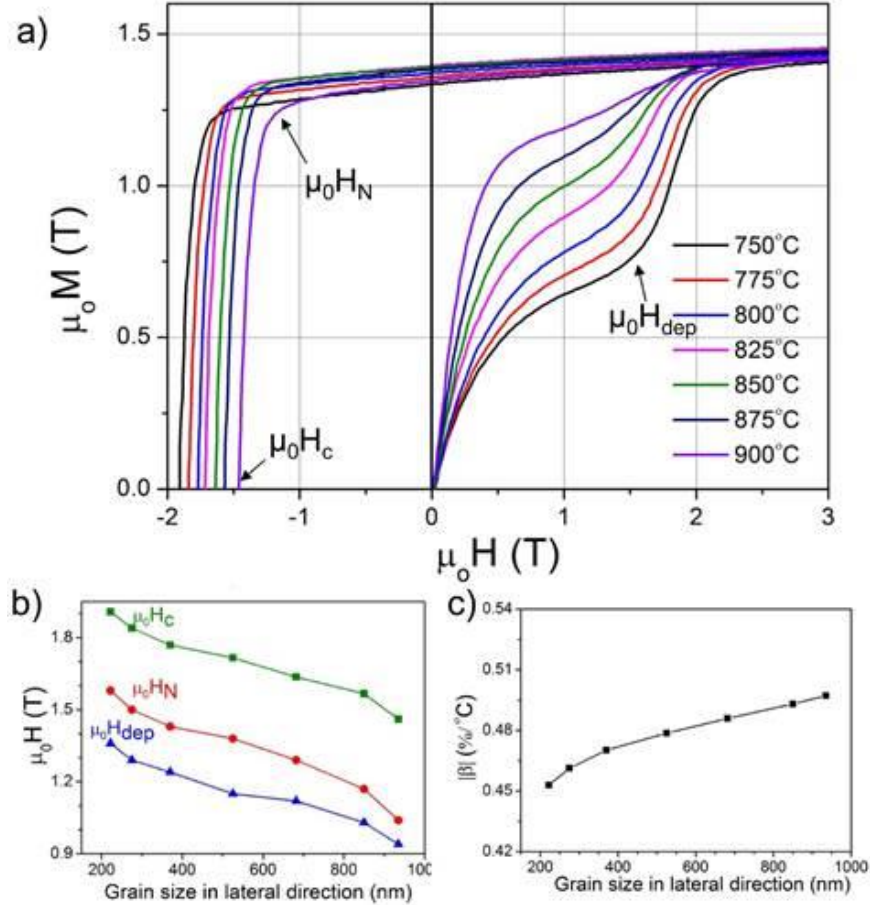


Figure 4.2 (a) Magnetization curves of the Nd-Fe-B magnets hot-deformed at temperature range from 750 to 900°C. (b) The plot of the coercivity, nucleation field, and depinning field versus the grain size of the hot-deformed magnets. (c) Absolute value of temperature coefficient of coercivity versus the grain size of the hot-deformed magnets.

### 4.3.2 Microstructure

To understand the contribution of the microstructure to the magnetic properties, the microstructures of the magnets hot-deformed at 750, 825, 900°C were characterized. Hereafter, these samples are denoted as HD750, HD825, and HD900. Figure 4.3 shows BSE SEM images with c-axis in-plane for (a) HD750, (b) HD825, and (c) HD900, and out of plane for (d) HD750, (e) HD825, and (f) HD900. The fine  $\text{Nd}_2\text{Fe}_{14}\text{B}$  grains with a dark contrast were separated by a thin intergranular phase with a bright contrast. Some large Nd-rich triple junction phases can be seen with the bright contrast, particularly in HD900. It is clear that the grains grew with increasing the hot-deformation temperature. Besides, the

distribution of Nd-rich phase also changed. In HD750 the tiny Nd-rich intergranular phases were observed along the grain boundaries uniformly, while they aggregated at the triple junctions in HD900. The areal fraction of Nd-rich phases was estimated to be 3.7% for HD750, 6.3% for HD825, and 7.7% for HD900.

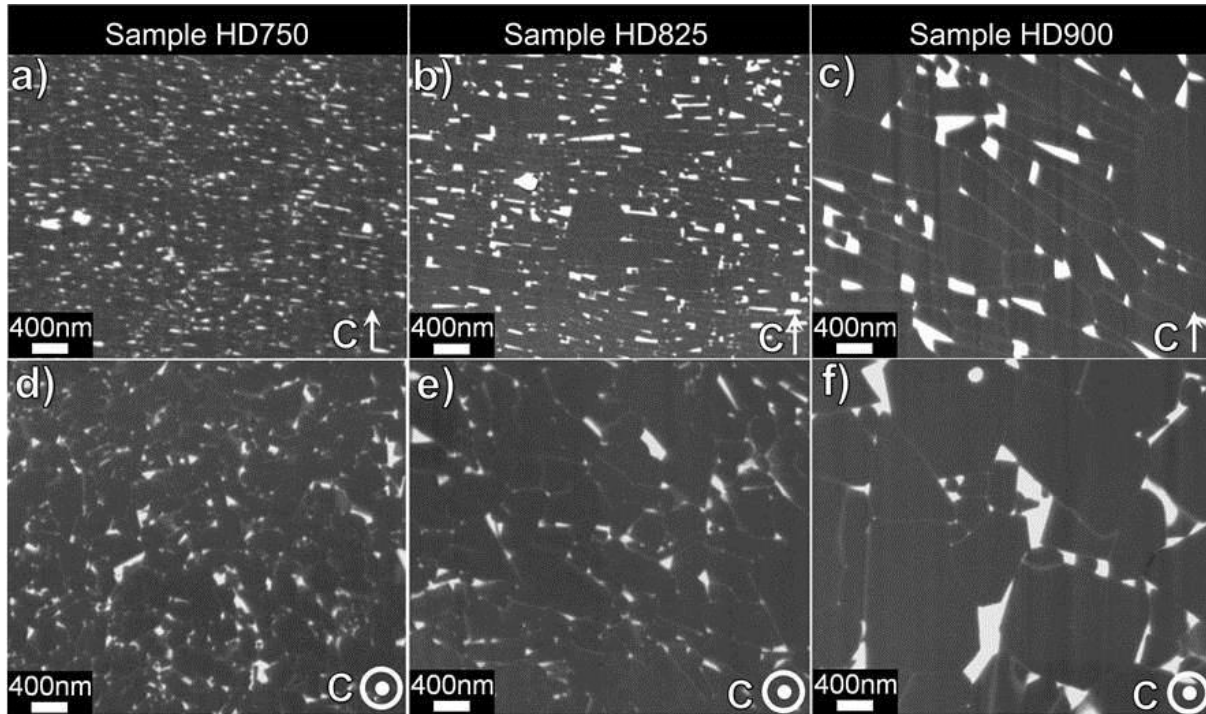


Figure 4.3 BSE SEM images with c-axis in plane for (a) HD750, (b) HD825, (c) HD900, and out of plane for (d) HD750, (e) HD825, (f) HD900.

To understand why the areal fraction of the Nd-rich phase was different in the samples with different hot-deformation temperatures regardless of the same alloy composition, we heat-treated the HD750 sample at 900°C in vacuum. Figures 4.4a-b show BSE SEM images of HD750 and heat-treated HD750, respectively. Besides the seriously coarsened grains, the Nd element was found to be aggregated at the triple junctions to form large Nd-rich phases and the contrast from the grain boundaries diminished. The areal fraction of the Nd-rich phase was estimated to be around 7.6% for the heat-treated HD750. This value is very close to that of HD900.

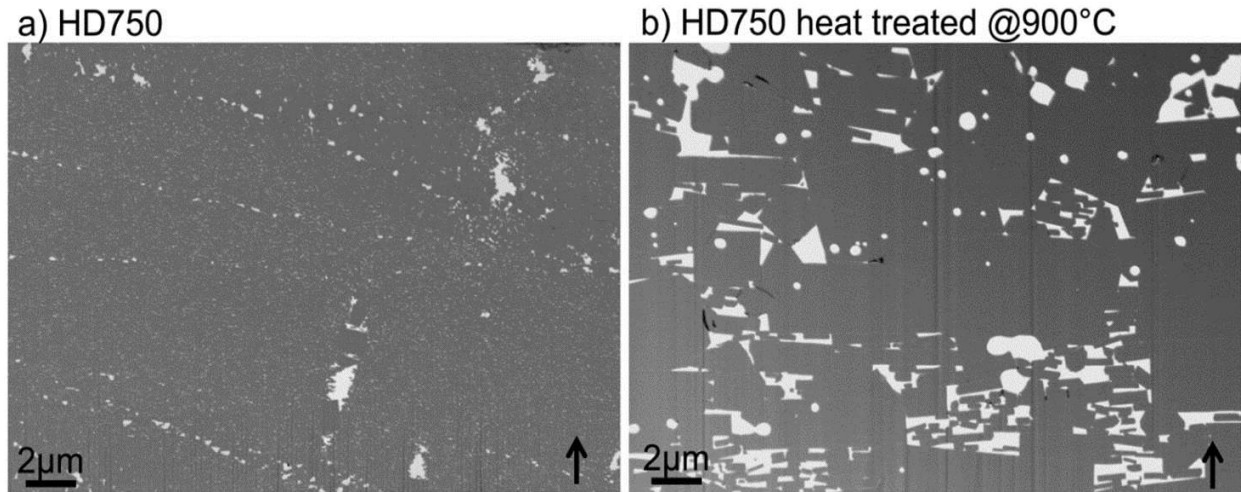


Figure 4.4 BSE SEM images of (a) HD750 and (b) HD750 heat-treated at 900°C.

Figures 4.5a-c show typical high resolution TEM images of the intergranular phase of (a) HD750, (b) HD825, and (c) HD900, respectively. All the intergranular layers are less than 2 nm in thickness with an amorphous structure. The thickness of the intergranular phase was comparable for HD750 and HD825. However, the intergranular layer became thinner in the case of HD900 probably because the Nd in the intergranular region was used up for the formation of the large Nd-rich triple junction phases.

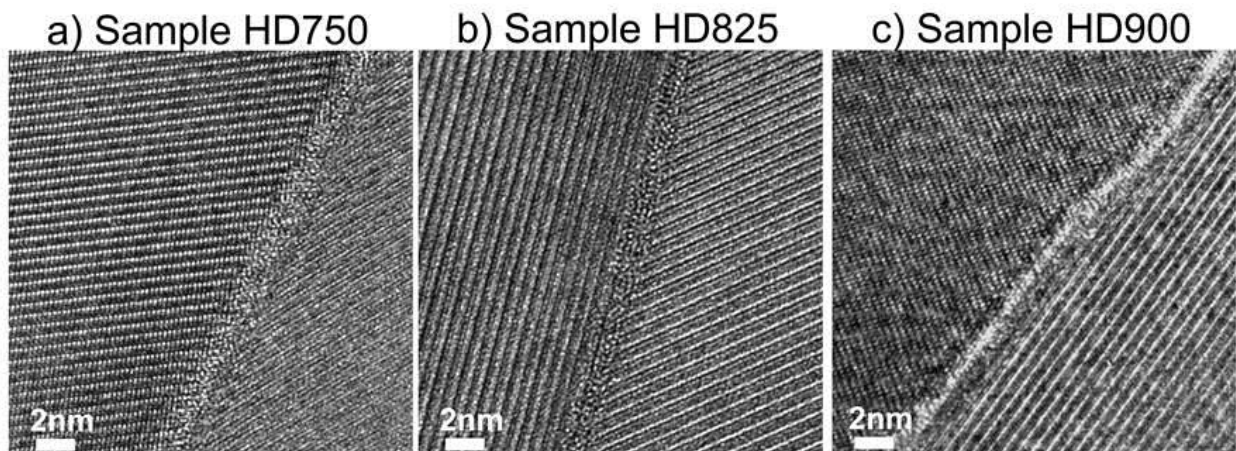


Figure 4.5 HRTEM images of the intergranular phase from (a) HD750, (b) HD825, (c) HD900.

In order to estimate the composition of the intergranular phase, 3DAP analyses were performed on these three samples. Figure 4.6a shows the 3DAP map of Nd obtained from HD750. Three intergranular

layers are observed in the atom probe tomography as Nd-enriched layers. The atom map within the inset volume perpendicular to the intergranular layer is shown in Figure 4.6b and the composition profiles calculated from the selected volume are shown in Figure 4.6c. A high enrichment of Nd and Ga and a depletion of Fe can be seen in the intergranular phase. The concentration of Nd and (Fe+Co) in the intergranular phase was  $58 \pm 3.9$  at.% and  $37 \pm 3.9$  at.%, respectively. Figure 4.7 shows a 3DAP result of an intergranular phase from HD825. The composition profiles (Figure 4.7c) calculated from the selected volume in Figure 4.7b show that the Nd concentration in the intergranular phase was  $36 \pm 3.3$  at.% and the amount of ferromagnetic elements (Fe+Co) was  $60 \pm 3.4$  at.% in the intergranular layer. Figure 4.8 shows the atom probe tomography from HD900, in which two intergranular layers were detected. The Nd concentration in the intergranular phase was only  $23 \pm 3.0$  at.%, which was much lower than that of HD750. The amount of (Fe+Co) dramatically increased to  $\sim 72 \pm 3.1$  at.%, suggesting the intergranular phase is ferromagnetic. The difference of the Nd concentrations in the intergranular phase of the three samples is consistent with the difference in the areal fraction of the Nd-rich phase; the Nd in the intergranular phase decreases when the volume fraction of the Nd-rich phases at the triple junctions increases at elevated temperature. This difference can be attributed to the phase equilibrium between the  $\text{Nd}_2\text{Fe}_{14}\text{B}$  and the Nd-rich liquid phase at the different temperatures; i.e. the Nd-concentration in the liquid phase increases as temperature decreases in the quasi  $\text{Nd}_2\text{Fe}_{14}\text{B}$ -Nd phase diagram [11]. Our previous study showed that higher concentration of Nd in the intergranular phase increase the pinning force for magnetic domain wall displacements [12].

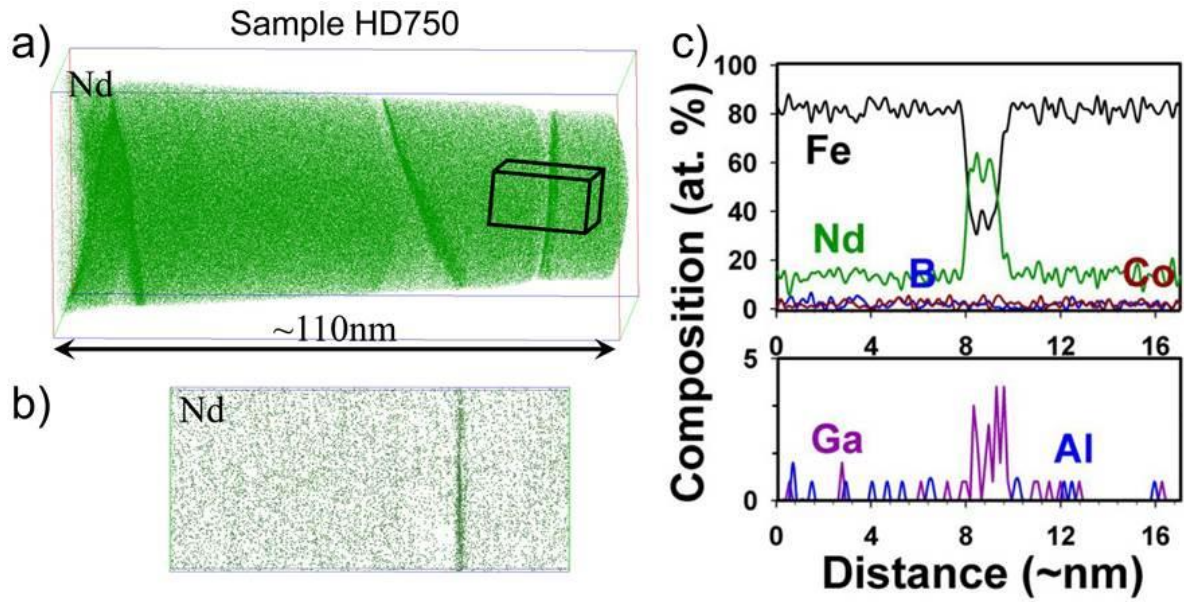


Figure 4.6 (a) 3DAP map of Nd obtained from HD750, (b) atom probe map of Nd of the selected volume perpendicular to intergranular phase, (c) concentration depth profiles for Fe, Nd, B, Co, Ga and Al determined from 3DAP analysis shown in (b).

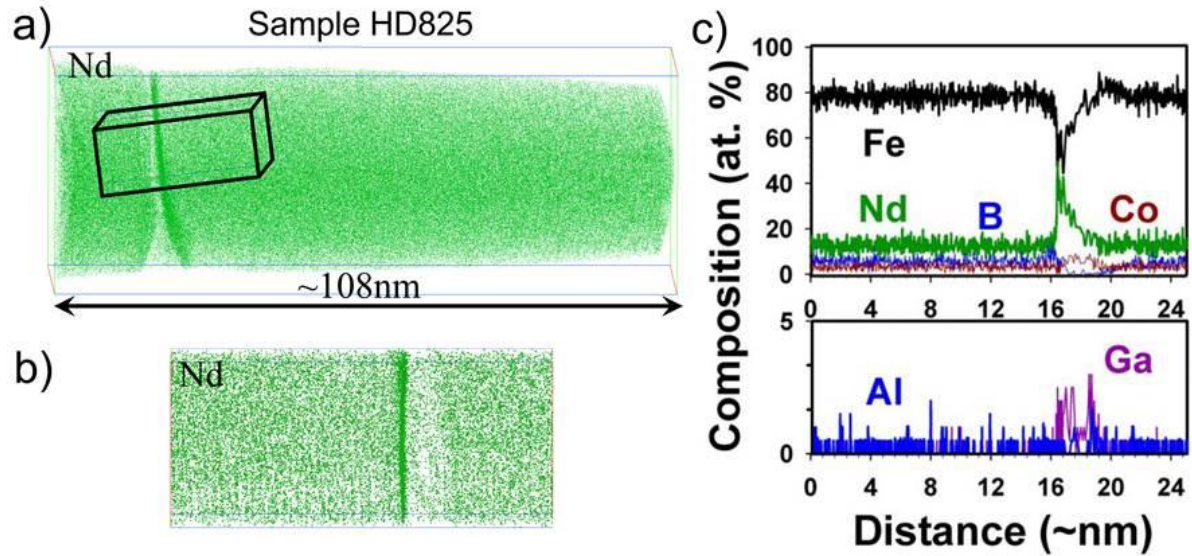


Figure 4.7 (a) 3DAP map of Nd obtained from HD825, (b) atom probe map of Nd of the selected volume perpendicular to intergranular phase, (c) concentration depth profiles for Fe, Nd, B, Co, Ga and Al determined from 3DAP analysis shown in (b).

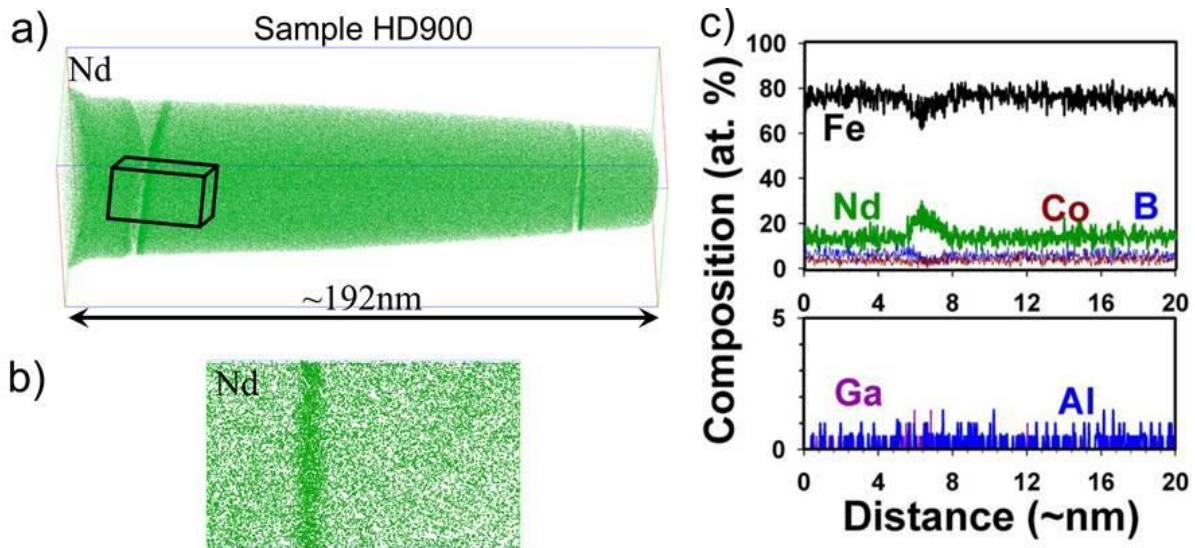


Figure 4.8 (a) 3DAP map of Nd obtained from HD900, (b) atom probe map of Nd of the selected volume perpendicular to intergranular phase, (c) concentration depth profiles for Fe, Nd, B, Co, Ga and Al determined from 3DAP analysis shown in (b).

To study how the magnetic domain structure of the hot-deformed magnets changes with these microstructure changes, TEM observations with Lorentz microscopy in Fresnel mode were performed on HD750 and HD900 with *c*-axis in-plane as shown in Figure 4.9. The light and dark stripes are magnetic domain walls. In thermally demagnetized state, the domain walls lie parallel to the *c*-axis of the  $\text{Nd}_2\text{Fe}_{14}\text{B}$  grains and extend through many grains, intersecting the grains or lying along the intergranular layers. In the case of HD750, with applying magnetic fields, the domain walls within the grains moved from their original positions within the grains towards the intergranular phases, while the domain walls along the intergranular layers remained unchanged. The stripe-shaped domain walls changed to zigzag shape due to the pinning effect at the intergranular phase. It can be seen that some domain walls still remained in the grains at the applied field of 0.05 T. In HD900, the multi-domain large  $\text{Nd}_2\text{Fe}_{14}\text{B}$  grains are observed in which the magnetic domain walls moved freely. Comparison of Figure 4.9a and Figure 4.9b explains the difference in the initial magnetization curves in Figure 4.2, that is, a small fraction of magnetization reversal occurs by the in-grain domain wall displacements in HD750, while a large fraction of magnetization reversal can occur by the magnetic domain wall displacements within the grains in HD900. The larger depinning field observed in the initial magnetization curve for HD750 in Figure 4.2 is due to the higher Nd concentration in the intergranular phase in HD750 as shown in Figure 4.6 and 4.8.

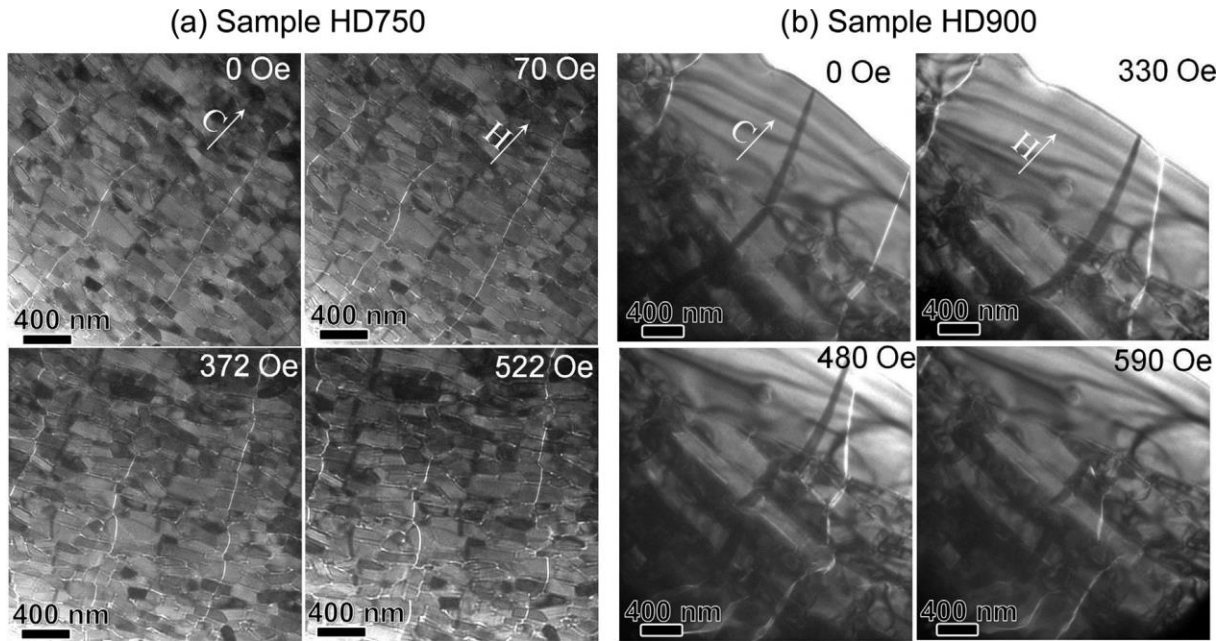


Figure 4.9 In situ Lorentz TEM observations in Fresnel mode on (a) HD750 and (b) HD900 with c-axis in-plane.

### 4.3.3 Micromagnetic simulations

We simulated the contribution of the grain size and grain boundary composition to the coercivity of the modeled hot-deformed Nd-Fe-B magnets. Figures 4.10a and b show the modeled hot-deformed Nd-Fe-B magnets with grain sizes of 60 and 150 nm in the lateral direction. The  $\text{Nd}_2\text{Fe}_{14}\text{B}$  grains are separated with a 3 nm thin intergranular layer in all the models. The saturation magnetization ( $\mu_0M_s$ ) and exchange stiffness (A) of the intergranular phase was chosen as 1.2 T and 12 pJ/m for the 150 nm grain-sized model to simulate the exchange coupled  $\text{Nd}_2\text{Fe}_{14}\text{B}$  grains for HD900. The saturation magnetization ( $\mu_0M_s$ ) and exchange stiffness (A) of the intergranular phase was varied as  $\mu_0M_s = 1.2$  T and  $A = 12$  pJ/m and  $\mu_0M_s = 0.03$  T and  $A = 1$  pJ/m for the 60 nm grain-sized model to simulate exchange coupled and weakly exchange coupled small grain-sized hot-deformed magnets. The simulated demagnetization curves for the hot-deformed models with grain sizes of 150 and 60 nm are shown in Figure 4.10c. The exchange coupled model with grain sizes of 150 nm and 60 nm showed the same coercivity of 3.19 T. However, the coercivity of the weakly exchange coupled 60 nm grain-sized model was increased to 4.05 T. This result indicates that the role of the intergranular phase is more pronounced in the smaller grain-sized hot-deformed Nd-Fe-B magnets, i.e., minimizing the ferromagnetic exchange coupling in a smaller grain-sized magnet is more effective to achieve a high coercivity. Note that the unrealistically high coercivity in the simulation is mainly due to the ignorance of the defects that reduce the anisotropy field

at surface and grain boundaries in the real magnets. The micromagnetic simulation result showed that the ferromagnetic exchange coupling among  $\text{Nd}_2\text{Fe}_{14}\text{B}$  grains must be reduced to get a higher coercivity by the reduction of grain size. This means that the larger coercivity observed in HD750 is not only because of the reduction of the grain size, but also because of the increase in the Nd concentration in the intergranular phase at the low processing temperature.

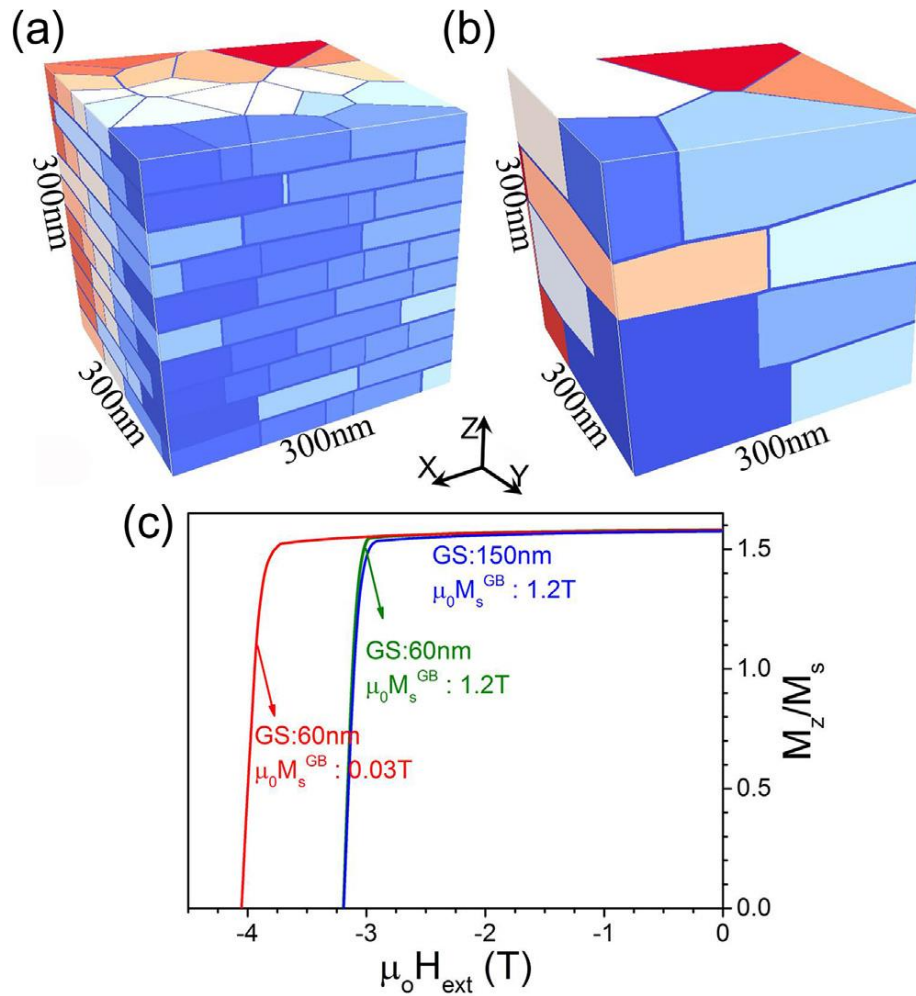


Figure 4.10 Modeled hot-deformed Nd-Fe-B magnets with average grain size in lateral direction of (a) 60 nm, (b) 150 nm. (c) Demagnetization curve of simulated hot-deformed Nd-Fe-B magnets with the average grain size in lateral direction of 150 nm and 60 nm. The saturation magnetization of intergranular phase ( $\mu_0 M_s^{\text{GB}}$ ) was chosen as 1.2 T for 150 nm grain-sized model while it was 1.2 T and 0.03T for 60 nm grain-sized model. (Courtesy of Dr. H. Sepehri-Amin)

Figure 4.11 shows the magnetic configuration at the nucleation point and during subsequent domain wall propagation in the 60 nm grain-sized model for different saturation magnetizations of the intergranular phase ( $\mu_0 M_s^{\text{GB}}$ ) of (a) 1.2 T and (b) 0.03 T. The applied external magnetic field is shown in the inset of the figures. In the exchange coupled 60 nm grain-sized model, the multiple nucleations of reversed domains are observed at the intergranular phases, which propagate to the neighboring grains. On the other hand, a reversed magnetic domain nucleates at the corner of the platelet-shaped  $\text{Nd}_2\text{Fe}_{14}\text{B}$  grains for the weakly exchange coupled 60 nm grain-sized magnet. We also compared the domain wall motion of the models during the domain wall propagation. There is no evidence for the domain wall pinning in the exchange coupled 60 nm grain-sized model. A similar domain wall propagation behavior was also observed for the exchange coupled 150 nm grain-sized model. However, in the weakly exchange coupled 60 nm grain-sized model, a zigzag domain wall configuration at the intergranular phase is observed, indicating a strong pinning strength at the intergranular phase. However, in the case of exchange coupled 60 and 150 nm grain-sized models, no pinning by intergranular phase was observed, indicating that the depinning field at the ferromagnetic intergranular phase is smaller than the nucleation field in these models.

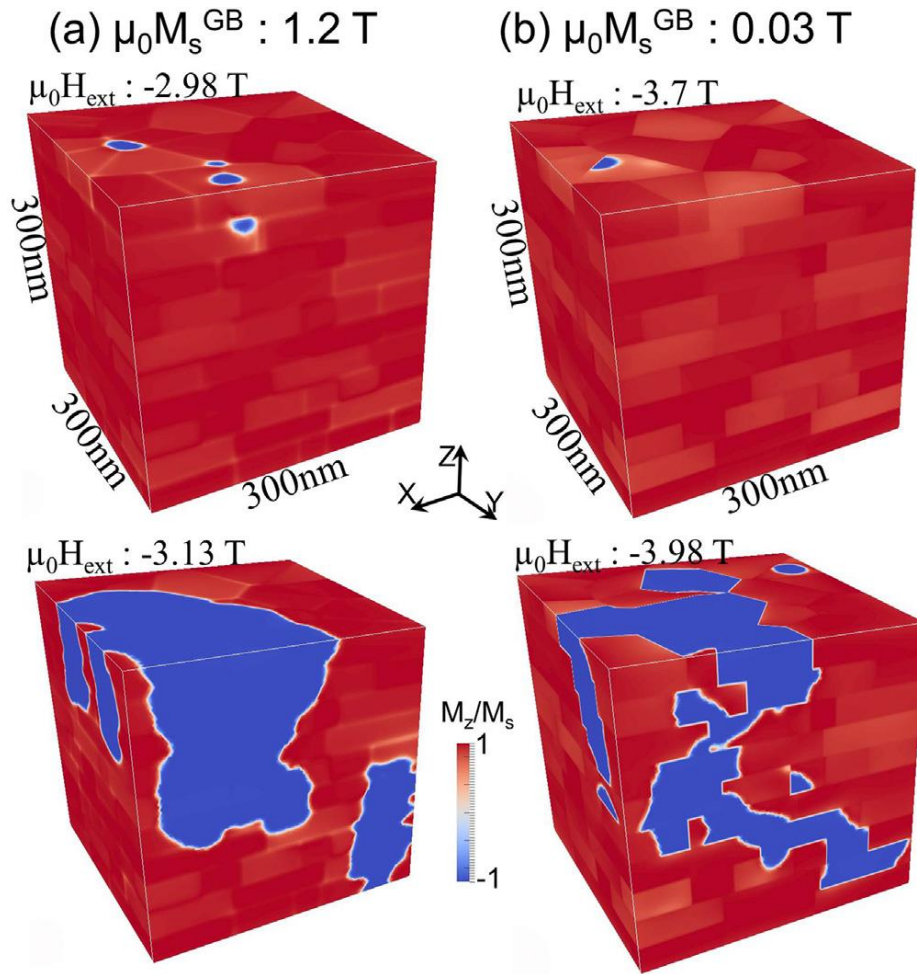


Figure 4.11 Magnetization configuration at nucleation field and during domain wall propagation of modeled hot-deformed magnets with grain size in lateral direction of 60 nm and different intergranular phase saturation magnetization ( $\mu_0 M_s^{GB}$ ) of (a) 1.2 T and (b) 0.03 T. Red and blue colors correspond to  $M_z/M_s = +1$  and  $-1$  respectively. (Courtesy of Dr. H. Sepehri-Amin)

#### 4.4 Discussion

This work has convincingly shown that  $\mu_0 H_c$  and  $\beta$  strongly depend on the grain size. The  $\mu_0 H_c$  increases and the absolute value of  $\beta$  decreases as the grain size decreases. A phenomenological approach is employed to study the relationship between microstructure and coercivity as described by the following equation:

$$H_c(T) = \alpha H_A(T) - N_{\text{eff}} M_s(T), \quad (4.1)$$

where  $H_A$  is the anisotropy field,  $M_s$  is the saturation magnetization,  $\alpha$  describes the reduction in the anisotropy field at defects such as grain boundaries, and  $N_{\text{eff}}$  describes an effective demagnetization factor [13,14]. By using Equation (4.1) and plotting  $H_c/M_s$  vs  $H_A/M_s$  for different temperatures, parameters  $\alpha$  and  $N_{\text{eff}}$  were deduced by fitting the data to a straight line. Parameter  $\alpha$  was calculated to be 0.59, 0.60, and 0.55, and  $N_{\text{eff}}$  was 0.87, 1.23, and 1.23 for HD750, HD825, and HD900, respectively. The value of  $\alpha$  is almost the same for the three samples, while the change in  $N_{\text{eff}}$  is around 41%, which gives a main effect on the coercivity. Major factors influencing  $N_{\text{eff}}$  is the grain size, grain shape, existence of nonferromagnetic Nd-rich triple junction phases and intergranular exchange as these influence the stray field to neighboring grains. The aspect ratios (longitudinal/lateral of grain) of the samples were 0.38, 0.26 and 0.26 for HD750, HD825 and HD900, respectively. A larger longitudinal/lateral aspect ratio of the  $\text{Nd}_2\text{Fe}_{14}\text{B}$  grains in the hot-deformed magnets leads to a lower  $N_{\text{eff}}$  value as grain size decreases [8,15]. The change of the aspect ratio was 32%; therefore it should affect  $N_{\text{eff}}$  strongly. In addition, BSE SEM observations show that the areal fraction of the Nd-rich phases increases as the grain size increases. The presence of these nonferromagnetic particles is expected to cause stray field, thereby increasing  $N_{\text{eff}}$  [13,15]. Thus, the reduction of grain size decreases the demagnetizing field, leading to the increase in coercivity. Decreasing  $N_{\text{eff}}$  by grain size refinement is also responsible for the reduction in the absolute value of temperature coefficient of coercivity. The distribution of the stray field in the modeled magnets with grain size of 1.0, 2.0, and 2.7  $\mu\text{m}$  is plotted in Figure 4.12b [7], which shows that the stray field decreases as the reduction of the grain size. Therefore, the  $N_{\text{eff}}$  value in the smaller grain sized magnets should be smaller. If we assume  $\alpha$  is same and vary the  $N_{\text{eff}}$  value, by using the Equation (4.1) the plot of the coercivity vs. temperature of the modeled Nd-Fe-B magnets with different  $N_{\text{eff}}$  can be obtained as shown in Figure 4.12d. The absolute value of temperature coefficient of coercivity can be calculated from Figure 4.12d and this value is found to be decreased as the reduction of  $N_{\text{eff}}$ . This phenomenon can be explained by the different temperature dependence of the anisotropy field and saturation magnetization of Nd-Fe-B. The anisotropy field decreases sharply while the saturation magnetization decreases slowly from room temperature to  $\sim 200$  °C. Therefore,  $N_{\text{eff}}M_s$  is less temperature dependent than  $\alpha H_A$  at elevated temperature and it suppress the thermal degradation of coercivity [16]. As a result, absolute value of temperature coefficient of coercivity is smaller in the smaller grain sized Nd-Fe-B magnets. Note that the Nd concentration in the intergranular phase is higher in smaller grain magnets because of lower processing temperature and this also increases the nucleation field as well as the pinning force at the grain boundaries as was shown in the micromagnetic simulation results (Figure 4.11).

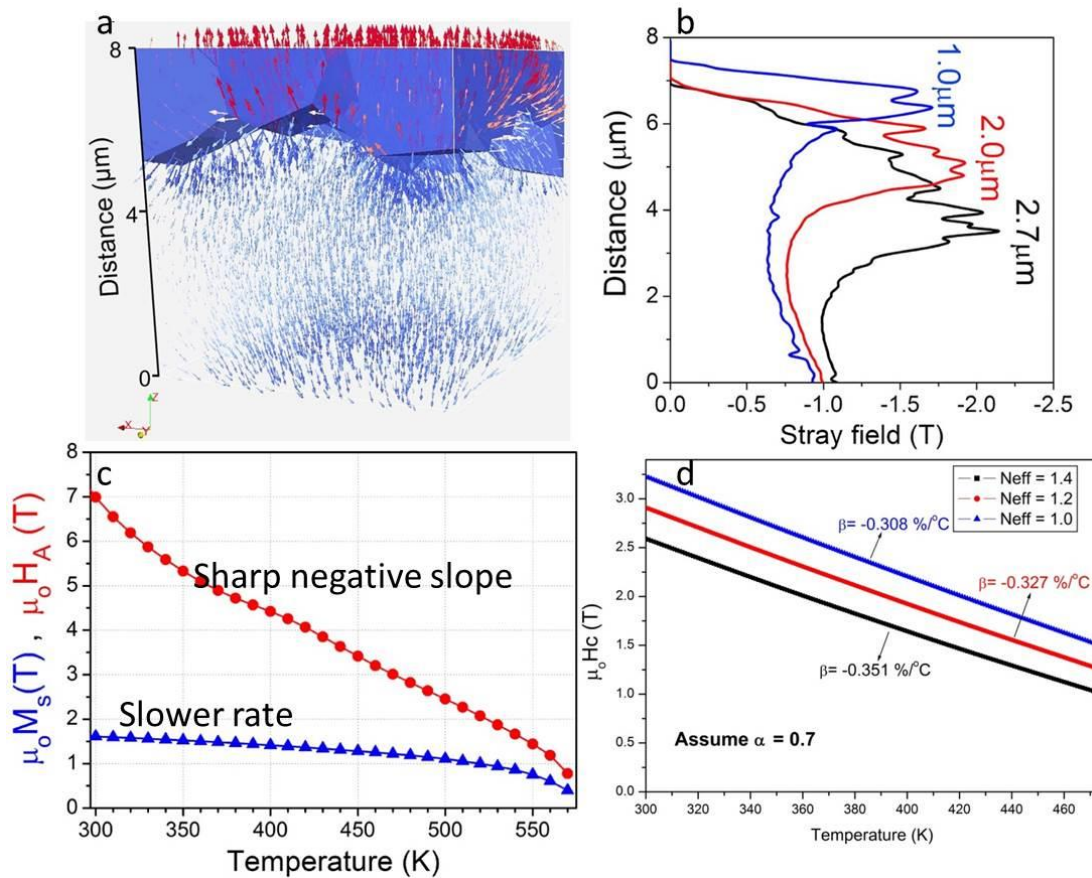


Figure 4.12 (a) Distribution of demagnetization vectors in the 2.0 μm grain sized model. (b) Distribution of the maximum stray field calculated from surface slices from Z=0 μm to Z=8 μm for models with grain size of 1.0, 2.0, and 2.7 μm. (c) Temperature dependence of anisotropy field and saturation magnetization of Nd-Fe-B. (d) Coercivity vs. temperature of modeled Nd-Fe-B magnets with different demagnetization factors [7].

This work has shown that there are linear correlations among the coercivity, nucleation field, and depinning field (Figure 4.2b). This suggests that the coercivity can be enhanced by increasing the depinning field. The microstructure studies reveal that the Nd<sub>2</sub>Fe<sub>14</sub>B grains are well surrounded by the thin layers of the intergranular phase in the smaller grain size magnets, which means there are more pinning sites that restrain domain wall motion. Increasing the hot-deformation temperature not only causes excessive grain growth, but also leads to aggregation of the Nd-rich phase at triple junction and the reduction in the Nd concentration in the intergranular phase. The reduced Nd concentration in the intergranular phase can be explained from the phase equilibrium between the Nd<sub>2</sub>Fe<sub>14</sub>B grains and the liquid Nd-rich phase at elevated temperature; then the excess Nd forms the large Nd-rich triple junction

phases. This explains the thinner intergranular phase (Figure 4.5c) and the lower Nd content in the intergranular phase of HD900 (Figure 4.8c). Our previous micromagnetic simulations have shown that the nonferromagnetic grain boundary phase can prevent the nucleation of reversed domains at low magnetic fields [12]. The micromagnetic simulations in this study suggest that the depinning field also increases as the magnetization of the intergranular phase reduces. Besides, a fine and homogeneously distributed Nd-rich phase provides a higher number of pinning sites in the smaller grain-sized magnets.

In spite of the much smaller grain-sized compared to that of the sintered magnets, the coercivity of hot-deformed Nd-Fe-B magnets is only comparable to that of the highest value of the sintered magnets [17,18]. Figure 4.2b shows that the depinning field is smaller than the nucleation field in all the cases, which is consistent with the simulation result in Figure 4.10c. So, the coercivity is controlled by the nucleation of reverse domains at the weakest points in the microstructure. These weak points could be the oxides and larger grain regions that are present in the former flake boundaries (e.g. Figure 4.4(a)). Once the nucleation of reversed domains occurs at such weak points, they propagate cooperatively and the pinning effect cannot control the coercivity. To further increase the coercivity, we need to enhance the pinning strength of the intergranular phase against the domain walls motion by changing the intergranular phase to be non-ferromagnetic with an optimum thickness. In such case, the magnetic exchange coupling among the  $\text{Nd}_2\text{Fe}_{14}\text{B}$  grains also decreases due to very low magnetization of the intergranular phase, and the domain walls cannot propagate to neighboring grains as the ideal case shown in Figure 4.11b. In fact, recent investigations on the grain boundary diffusion process using low melting temperature eutectic alloys such as Nd-Cu and Pr-Cu have shown that the decoupling of the grains by the infiltration of these nonferromagnetic phase substantially enhance the coercivity of hot-deformed magnets [2,19,20].

## 4.5 Summary

We investigated hard magnetic properties and microstructures of the hot-deformed Nd-Fe-B magnets with an identical alloy composition but were processed at different temperatures. Lower processing temperature led to a finer grain size with a higher Nd-content in the intergranular phase, resulting in a higher coercivity. We found good correlation among depinning fields in the initial magnetization curves and the nucleation field and coercivity, suggesting that domain wall pinning plays some role in the coercivity. Grain size reduction also improved the temperature dependence of the coercivity, which is beneficial for high temperature applications. Micromagnetic simulations showed that the reduction of grain size decreased the demagnetizing field, leading to the increase in coercivity and the improvement of the temperature dependence of the coercivity. While Nd-rich intergranular phases form

uniformly in the fine-grained sample processed at low temperature, the large Nd-rich triple junction phases are more frequently observed in the sample at a higher temperature. Micromagnetic simulations showed that the nucleation of reversed magnetic domain starts at the intergranular phase. The number of nucleation sites decreases and the pinning strength increases with the decreasing Fe content in the grain boundary phase.

## Reference

- [1] H. Sepehri-Amin, T. Ohkubo, S. Nagashima, M. Yano, T. Shoji, A. Kato, T. Schrefl, K. Hono, *Acta Materialia*, 61 6622 (2013).
- [2] T. Akiya, J. Liu, H. Sepehri-Amin, T. Ohkubo, K. Hioki, A. Hattori, K. Hono, *Journal of Applied Physics*, 115 17A766 (2014).
- [3] R. Ramesh, G. Thomas, B.M. Ma, *Journal of Applied Physics*, 64, 6416 (1988).
- [4] P. Nothnagel, K.H. Müller, D. Echert, A. Handstein, *Journal of Magnetism and Magnetic Materials*, 101, 379 (1991).
- [5] K. Uestuener, M. Katter, W. Rodewald, *IEEE Transactions on Magnetics*, 42, 2897 (2006).
- [6] K. Hioki, A. Hattori, T. Iriyama, *Journal of Magnetics Society of Japan*, 38(3), 79 (2014).
- [7] H. Sepehri-Amin, T. Ohkubo, M. Gruber, T. Schrefl, K. Hono, *Scripta Materialia*, 89, 29 (2014).
- [8] W.B. Cui, Y.K. Takahashi, K. Hono, *Acta Materialia*, 59, 7768 (2011).
- [9] M. Sagawa, S. Fujimura, H. Yamamoto, Y. Matsuura, S. Hirosawa, *Journal of Applied Physics*, 57, 4094 (1985).
- [10] T. Schrefl, J. Fidler, *Journal of Applied Physics*, 83, 6262 (1998).
- [11] D.S. Tsai, T.S. Chin, S.E. Hsu, M.P. Hung, *IEEE Transactions on Magnetics*, 23, 3607 (1987).
- [12] J. Liu, H. Sepehri-Amin, T. Ohkubo, K. Hioki, A. Hattori, T. Schrefl, K. Hono, *Acta Materialia*, 61, 5387 (2013).
- [13] H. Kronmüller, *Physics Status Solidi B: Basic Research*, 144, 385 (1987).
- [14] S. Hock, PhD thesis, Max-Planck-Institute for Metals Research, Institute of Physics, p118 (1988).
- [15] K. Hono, H. Sepehri-Amin, *Scripta Materialia*, 67, 530 (2012).
- [16] H. Kronmüller, M. Fähnle, “Micromagnetism and the Microstructure of Ferromagnetic Solids”, Cambridge University Press, 2003.
- [17] H. Sepehri-Amin, Y. Une, T. Ohkubo, K. Hono, M. Sagawa, *Scripta Materialia*, 65, 396 (2011).
- [18] Y. Une, M. Sagawa, Paper presented at the 21st International Workshop on Rare-Earth Permanent Magnets and Their Applications, Bled, Slovenia (2010).

[19] H. Sepehri-Amin, D. Prabhu, M. Hayashi, T. Ohkubo, K. Hioki, A. Hattori, K. Hono, *Scripta Materialia*, 68, 167 (2013).

[20] T. Akiya, J. Liu, H. Sepehri-Amin, T. Ohkubo, K. Hioki, A. Hattori, K. Hono, *Scripta Materialia*, 48, 81 (2014).

## Chapter 5. The microstructure evolution of hot-deformed Nd-Fe-B magnets

### 5.1 Introduction

Although the hot-deformed Nd-Fe-B magnets have advantages over the sintered ones on the aspect of small grain and free of Nd-oxide phase, their coercivity is disappointingly low for the single-domain sized grains and is only comparable to that of the highest value of the sintered magnets [1,2]. In the Chapter 4 we found good correlation among depinning fields and the nucleation field and coercivity. Although the pinning field may play some role in determining the coercivity, its value is lower than the nucleation field as shown in Figure 4.2b. Therefore, once the nucleation of reversed domains occurs at such weak points like the oxides and larger grain regions that are present in the former flake boundaries (Figure 4.4a), they propagate cooperatively and the pinning effect cannot control the coercivity. To further increase the coercivity, we need to enhance the pinning strength of the intergranular phase. It is known that the pinning force is strongly dependent on the energy difference of the hard magnetic  $\text{Nd}_2\text{Fe}_{14}\text{B}$  grains and the second phase Nd-rich grain boundary phase [3]. In other word, it is closely related to the microstructure and chemical composition of the two phases. The study on the microstructural evolutions and the chemical composition of the intergranular phase of hot-deformed Nd-Fe-B magnets in each processing stage may provide some useful information to improve the pinning force.

Grünberger et al. proposed a model of interface-controlled solution-precipitation creep to explain the formation of the texture [4]. Mishra et al. reported that the alignment of  $\text{Nd}_2\text{Fe}_{14}\text{B}$  grains results from a combination of plastic deformation, grain boundary migration, and grain boundary sliding [5,6]. The presence of the liquid Nd-rich intergranular phase during the hot-deformation process was known to be essential for the formation of the crystallographic c-axis texture of  $\text{Nd}_2\text{Fe}_{14}\text{B}$  grains parallel to the pressing direction. In addition, the Nd-rich intergranular phase makes an important role in the coercivity of the hot-deformed Nd-Fe-B magnets. The Nd-rich intergranular phases was reported to work as pinning sites against magnetic domain wall motion [7,8]. However, Lewis et al. found a high amount of Fe within the intergranular phase and suggested that the dominant coercivity mechanism is the nucleation of reversed domains in the Fe-rich intergranular region with reduced anisotropy [9,10]. Although plenty of work reported the role of intergranular phase on the development of c-axis texture and their correlations with coercivity, how the unique morphology of the platelet grains develops and the anisotropic nature of the chemical compositions of the intergranular phase is not thoroughly understood. In this study, we investigated the microstructural evolutions and the chemical composition of the intergranular phase of hot-deformed Nd-Fe-B magnets by using scanning electron microscopy (SEM), transmission electron

microscopy (TEM), and three dimensional atom probe (3DAP) in order to obtain a guideline to enhance the coercivity further.

## 5.2 Experiment

Alloy with nominal composition of  $\text{Nd}_{10.0}\text{Pr}_{3.4}\text{Fe}_{76.4}\text{Co}_{3.8}\text{B}_{5.6}\text{Ga}_{0.5}\text{Al}_{0.2}\text{Si}_{0.1}$  (at%) was melt-spun onto a rotating copper wheel. Flakes (MQ powders) produced by crushing the melt-spun ribbons were hot-pressed (MQ2) at 750 °C in vacuum and subsequently hot-deformed (MQ3) at 750 °C in an Ar atmosphere. Part of MQ powders was heated at 750 °C (MQHT) for 30 min in vacuum without pressing. The details of the hot-deformation process were described in Chapter 3 Part 2. Backscatter electron (BSE) SEM observations were performed using a Carl Zeiss CrossBeam 1540EsB. TEM observations were performed using a Titan G2 80-200 TEM. 3DAP analyses were conducted using a locally built laser-assisted wide angle three dimensional atom probe (LA-3DAP) under ultrahigh vacuum  $< 10^{-8}$  Pa at a base temperature of  $\sim 25$  K in the flux range of 0.003-0.010 atom/pulse using an UV laser (343 nm) with a power of 0.12  $\mu\text{J}/\text{pulse}$ .

## 5.3 Results and discussion

The magnetization curves of MQ powders, MQ2 and MQ3 magnets are shown in Figure 5.1a. The remanence ( $\mu_0 M_r$ ) was enhanced from 0.75 T for MQ powders to 0.85 T for MQ2, and 1.35 T for MQ3, while the coercivity ( $\mu_0 H_c$ ) decreased from 2.06 T to 1.76 T. Note that the initial magnetization curve of MQ3 shows a two-step behavior, which is a typical feature for the fine-grained Nd-Fe-B anisotropic magnets with grain size comparable to the single domain size of  $\text{Nd}_2\text{Fe}_{14}\text{B}$  grain [2,11-12]. Figure 5.1b shows the XRD patterns of MQ powders, MQ2 and MQ3. The intensity of (004), (105) and (006) peaks are very weak in the MQ powders and MQ2, while the intensity of these peaks are strengthened in MQ3. The XRD result is consistent with the change of measured remanence, which indicates that the enhanced (001) texture leads to a sharp increase in remanence of the hot-deformed magnets with a slightly reduced coercivity.

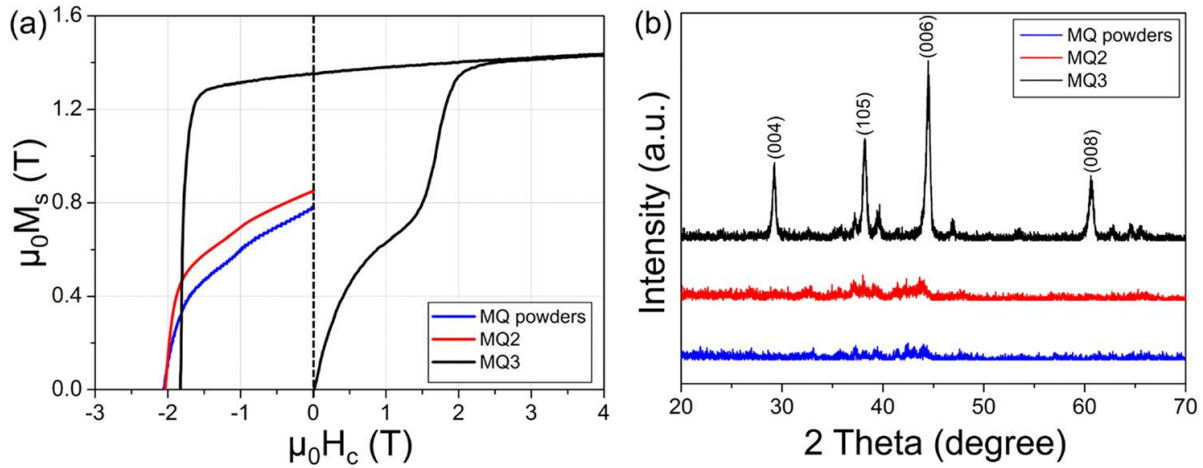


Figure 5.1(a) The demagnetization curves and (b) XRD patterns of MQ powders, MQ2 and MQ3.

Figures 5.2a-b show cross-sectional BSE SEM images of MQ and MQHT powders, respectively. The MQ powders show a uniform contrast in this magnification. After annealing at 750°C for 30 min, a dark gray layer with a thickness of  $\sim 7 \mu\text{m}$  appears at one surface of the flake. This is due to the serious surface crystallization of the MQ powder from the free surface of melt-spun sample that is often observed in melt-spun ribbons [13]. Chu et al. also reported that the degree of crystallinity and texture increase from the wheel side to the free side of the ribbons [14]. In addition, a weak white contrast from the Nd-rich intergranular phase can be seen inside of the layer. The white dotted contrasts observed on the surface of the flake are oxide particles. These surface oxides remain along the particles boundaries after the hot-deformation process. Bright field TEM images taken from Region 1 and Region 2 in Figure 5.2b are shown in Figures 5.2c and d, respectively. The surface layer consists of large equiaxed grains while  $\text{Nd}_2\text{Fe}_{14}\text{B}$  grains inside the flake are platelet shaped with flat surface on the (001) plane, but the platelets are randomly oriented. The average grain size in the surface layer is  $\sim 520 \text{ nm}$ . These large grains are hard to deform, forming unaligned regions near the particle boundaries in MQ3 [5,14]. Although the heat treatment was applied on powders without applying any force, the platelet growth of initially spherical grains in MQ powders was observed, suggesting that no force is required for the platelet growth of the  $\text{Nd}_2\text{Fe}_{14}\text{B}$  grain (Figure 5.2d). The platelet shaped morphology with c-plane as broad face suggests that the growth direction normal to the broad surface is much slower than that along the plate direction. This is because the (001) plane of the  $\text{Nd}_2\text{Fe}_{14}\text{B}$  phase is the most closely packed with layered structure (Nd rich planes every four layers). For the growth normal to the c-plane, ledge nucleation is required. This makes the growth direction normal to the c-planes very sluggish compared to the normal to the c-axis, thus the  $\text{Nd}_2\text{Fe}_{14}\text{B}$  grains spontaneously grow to platelets with c-plane as a broad surface. This indicates that compressive stress is not required for the evolution of the platelet shape morphology.

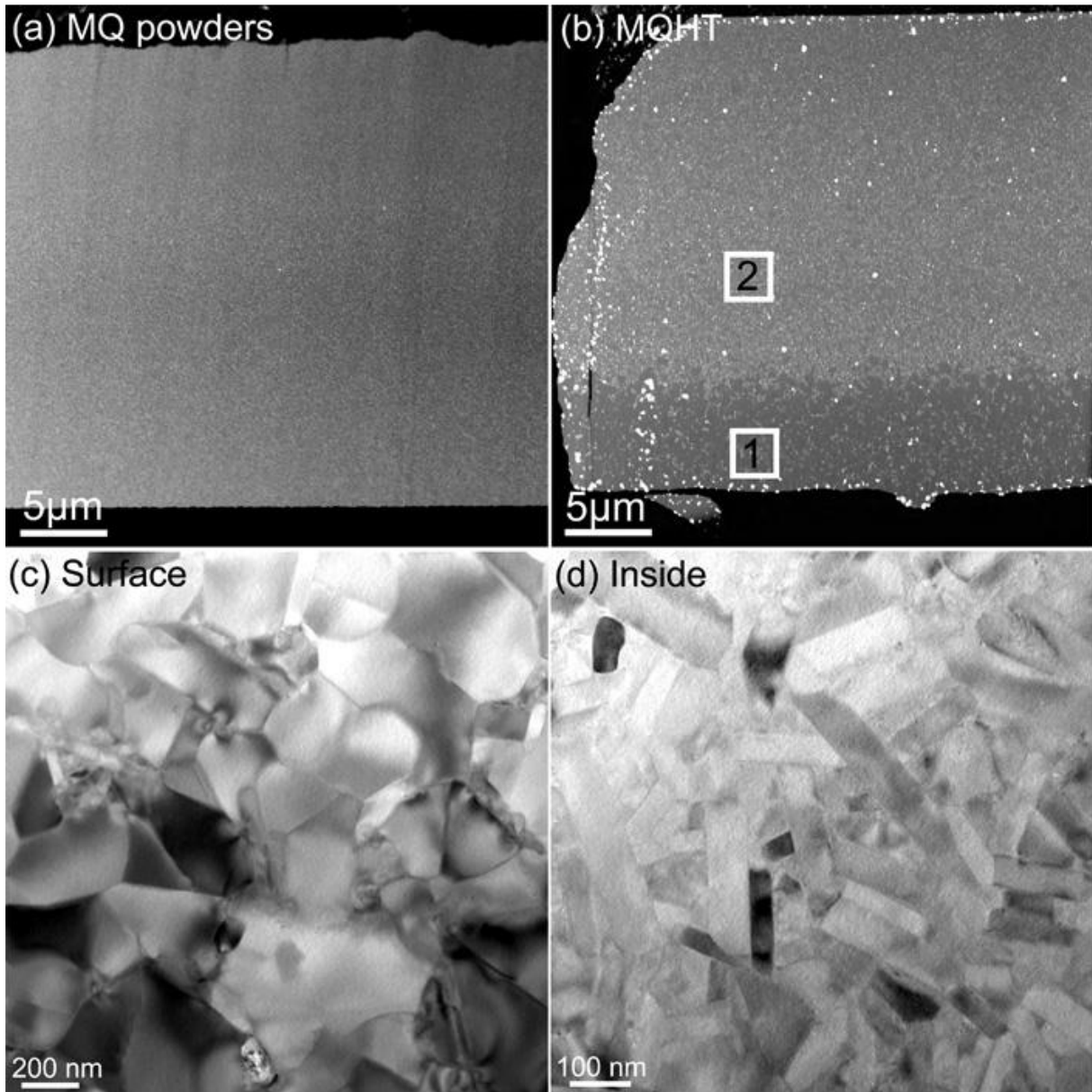


Figure 5.2 Cross-sectional BSE SEM images of (a) MQ powders and (b) MQHT. Bright field TEM images from (c) Region 1 and (d) Region 2 in Fig. 2(b).

Figure 5.3a shows bright field TEM images of MQ powders. The average size of polygonal isotropic  $\text{Nd}_2\text{Fe}_{14}\text{B}$  grains in MQ powders is  $\sim 40$  nm. There are fine precipitates dispersed in some  $\text{Nd}_2\text{Fe}_{14}\text{B}$  grains as indicated by the arrows in Figure 5.3a. The chemical composition of these precipitates was found to be around  $(\text{Nd,Pr})\text{Fe}_2$  by 3DAP measurement. High magnification TEM image of MQ powders in Figure 5.3b shows the existence of the amorphous intergranular phase while some of the  $\text{Nd}_2\text{Fe}_{14}\text{B}$  grains directly contact with each other. The Fe and Nd jump ratio images in Figures 5.3c-d

shows the depletion of Fe and a weak contrast of Nd at the intergranular phase. Some Nd-rich phases exist in the MQ powders. The composition profile of the intergranular phase calculated from 3DAP show a slight enrichment of Nd+Pr and a depletion of Fe, and the Nd+Pr concentration at the intergranular phase is ~26 at.% as shown in Figure 5.3e. This suggests that the intergranular phase is ferromagnetic and the grains are ferromagnetically coupled as reported by Sepehri-Amin et al [15]. If the ultrafine  $\text{Nd}_2\text{Fe}_{14}\text{B}$  grains in MQ powders are well isolated and magnetically decoupled by introducing nonferromagnetic elements into the intergranular layer, the coercivity would be improved further [16].

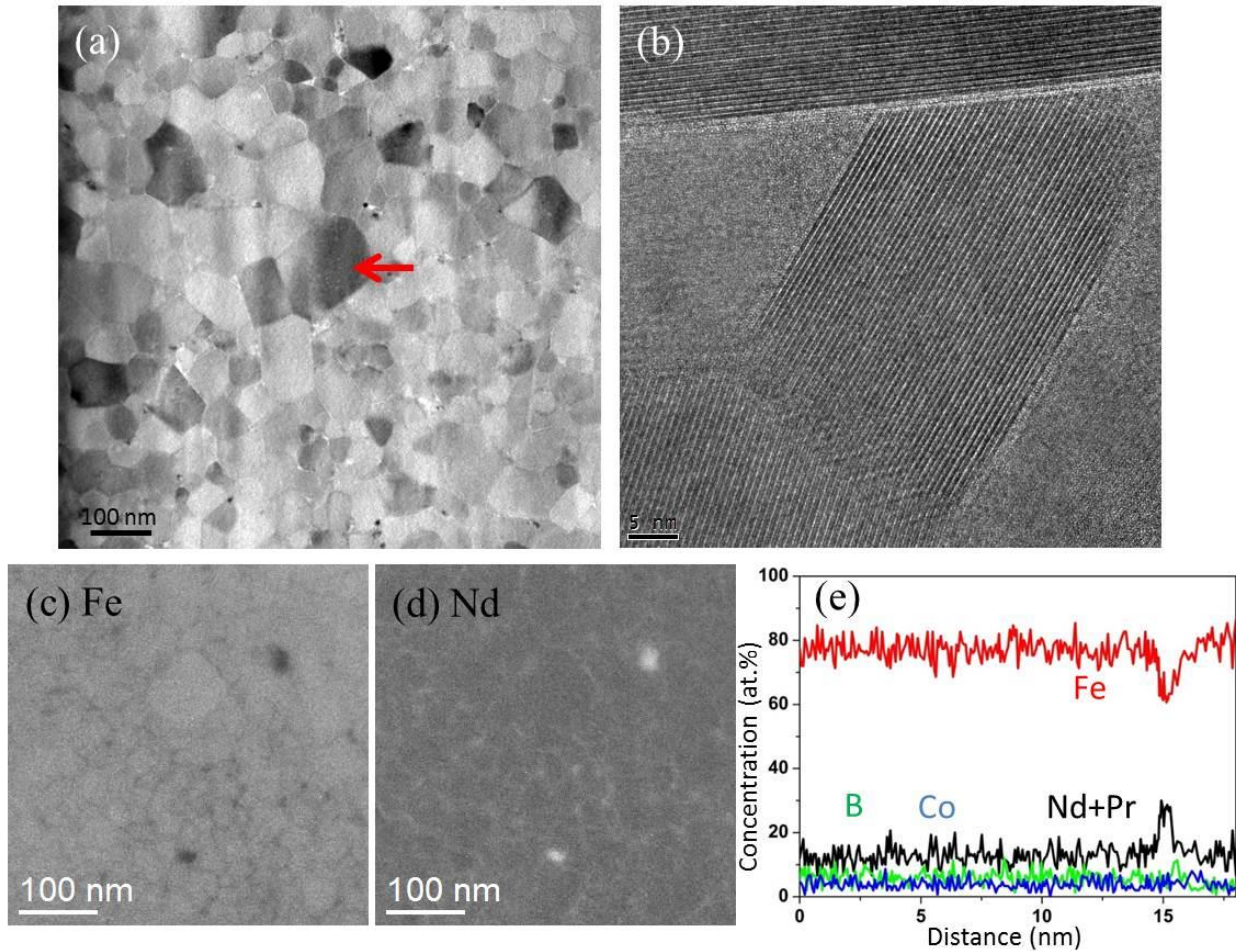


Figure 5.3 (a) Bright field TEM image, (b) HRTEM image, (c) Fe and (d) Nd jump ratio images and (e) composition profile of intergranular phase from MQ powders.

Bright field TEM image of MQ2 shows randomly oriented elongated  $\text{Nd}_2\text{Fe}_{14}\text{B}$  grains (Figure 5.4a), which is similar to that of inside of MQHT (Figure 5.2d). So, the change in grain shape already occurs during the hot-pressing process. High magnification TEM image in Figure 5.4b shows a sharp thin

layer of the intergranular phase along the broad surface of the  $\text{Nd}_2\text{Fe}_{14}\text{B}$  platelet ( $c$  IGF), while there is no clear intergranular layer in the short side of the platelet ( $a$  IGF) and the lattice fringes from the two grains are in direct contact each other at the  $a$  IGF. The elemental mapping of Fe and Nd in the Figures 5.4c-d show that the Fe is depleted and Nd is enriched along the  $c$  IGF while it looks like uniform across the  $a$  IGF. The composition profile of  $c$  IGF of the MQ2 magnet shows the Nd+Pr concentration of 34 at.% (Figure 5.4e), while the Nd+Pr profile is almost uniform across the  $a$  IGF (not shown). Higher amount of Nd+Pr was found in  $c$  IGF of the MQ2 sample compared to the Nd+Pr content of IGF in MQ powders. During the hot pressing at  $750^\circ\text{C}$ , the intergranular phase is considered to be liquid. Since the  $\text{Nd}_2\text{Fe}_{14}\text{B}$  grains are coarsened in the normal directions to the  $c$ -axis at the expense neighboring smaller grains, grain boundaries normal to the  $c$ -axis are expected to in direct contact with the neighboring grains. This is the reason why the Nd-rich intergranular phase cannot be observed in the interface parallel to the  $c$ -axis.

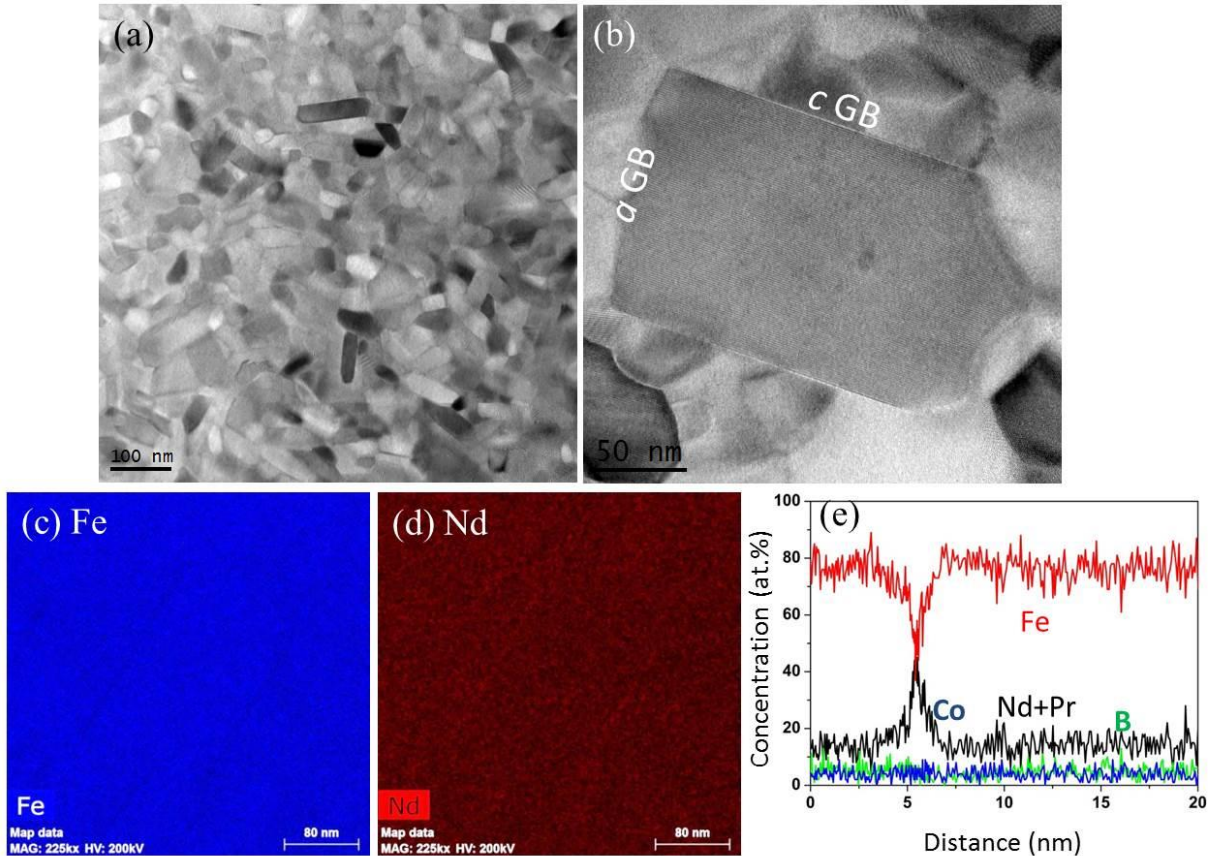


Figure 5.4 (a) Bright field TEM image, (b) high magnification image, (c) Fe and (d) Nd elemental mapping and (e) composition profile of intergranular phase from MQ2.

A good alignment of the platelet grains can be observed in MQ3 as shown in Figure 5.5a. HRTEM images from *c* IGF and *a* IGF of MQ3 sample are shown in Figures 5.5b and d, respectively. Although both *a* IGF and *c* IGF show amorphous structure, *c* IGF seems to be slightly thicker than that of *a* IGF. Composition profile of *c* IGF and *a* IGF obtained using 3DAP are shown in Figures 5.5c and e, respectively. The Nd+Pr content at *c* IGF is ~55 at.%, while that at *a* IGF is only ~25 at.%. These results indicate that not only the grain shape but also the segregation of rare-earth elements shows an anisotropic behavior, i. e. higher Nd+Pr at intergranular phase parallel to the broad surface of the Nd<sub>2</sub>Fe<sub>14</sub>B platelets (*c* IGFs) compare to those intergranular phase at the short side of Nd<sub>2</sub>Fe<sub>14</sub>B platelets (*a* IGFs). The presence of these amorphous phases would have made it possible for the platelets align during the hot-deformation process, as they viscously flow above the glass transition temperature. Under the presence of viscous glassy intergranular phase, the platelet would align with the broad surface normal to the compressive flow.

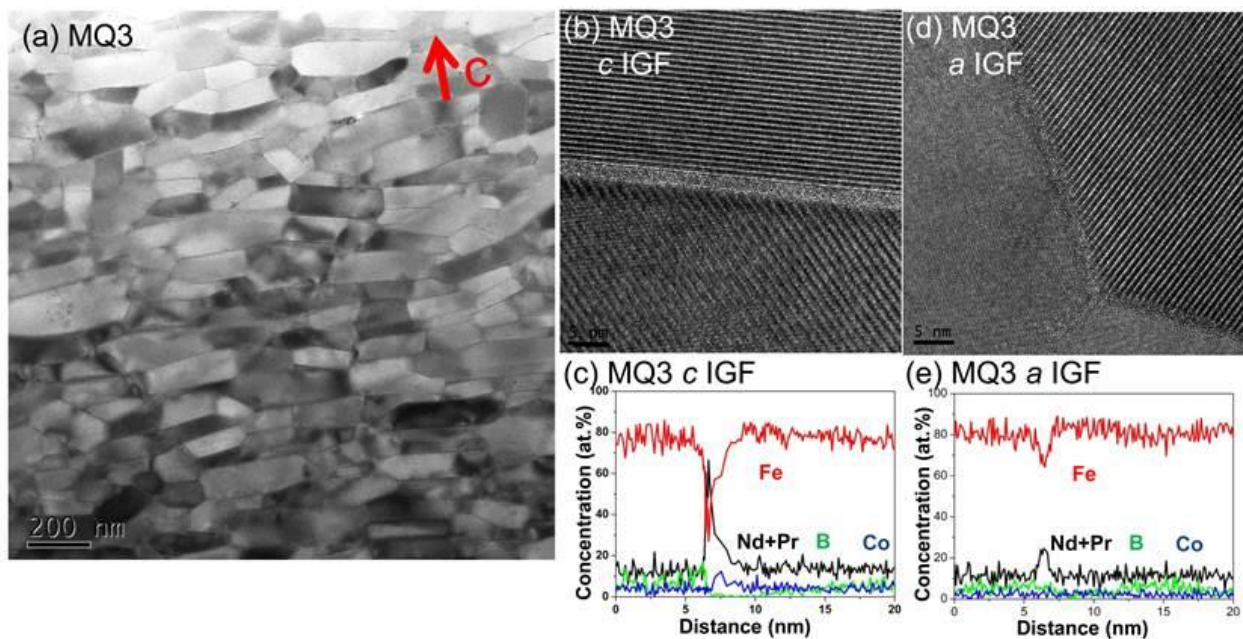


Figure 5.5 (a) Bright field TEM image of MQ3. HRTEM images of (b) *c* IGF and (b) *a* IGF of MQ3.

Composition profiles of (c) *c* IGF and (e) *a* IGF of MQ3 calculated from 3DAP analysis.

The two-step initial magnetization behavior of MQ3 magnets indicates the existence of the pinning site at the intergranular phase. In order to improve the pinning strength and magnetically decouple the neighboring grains, the post-treatment to introduce the nonmagnetic elements to *a* IGF and form a uniform intergranular phase is necessary.

The non-aligned equiaxial coarse  $\text{Nd}_2\text{Fe}_{14}\text{B}$  grains near the interface between the original flakes stem from the free surface of the rapidly solidified melt-spun ribbons. These regions with equiaxial coarse  $\text{Nd}_2\text{Fe}_{14}\text{B}$  grains make an inhomogeneous microstructure of the hot-deformed magnets and they were unfavorable for getting a high coercivity and deteriorate the squareness of the magnetic hysteresis. Recently, a two-stage deformation was reported by Mouri et al. to realize a grain refinement and improved texture of the  $\text{Nd}_2\text{Fe}_{14}\text{B}$  grains [17]. They introduced a low temperature pre-straining at 450-550 °C to suppress the formation of coarse grains. Then the hot-forging at 700 °C was used to accelerate the formation of the anisotropic grains and grain rotation. Both the coercivity and the squareness of the magnetization curves were improved as shown in Figure 5.6.

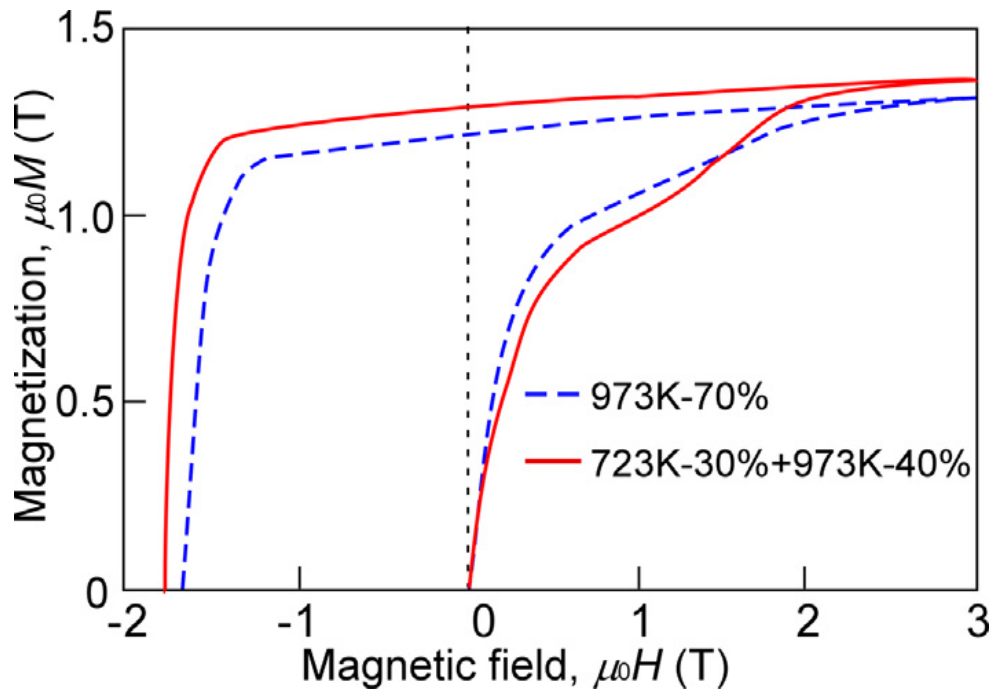


Figure 5.6 Magnetization curves of Nd-Fe-B alloys with and without pre-straining [17].

## 5.4 Summary

In summary, the anisotropic growth of the initially isotropic grains in the rapidly solidified powders occurred by the heat treatment without applying any compressive stress. A layer with large equiaxed grains appeared at the free surface of the heat-treated rapidly solidified flakes, which is the origin of the unaligned regions often observed in hot-deformed Nd-Fe-B magnets. In addition, 3DAP analyses of the intergranular phase revealed that the concentration of rare-earth elements shows an

anisotropic behavior with a higher concentration of the rare-earth elements in the intergranular phases parallel to the flat surface of the platelet shaped  $\text{Nd}_2\text{Fe}_{14}\text{B}$  grains compared to that of intergranular phases at the short side of platelets.

## Reference

- [1] Y. Une, M. Sagawa, Paper presented at the 21st International Workshop on Rare-Earth Permanent Magnets and Their Applications, Bled, Slovenia (2010).
- [2] H. Sepehri-Amin, Y. Une, T. Ohkubo, K. Hono, M. Sagawa, *Scripta Mater.* 65, 396 (2011).
- [3] D.I. Paul, *Journal of Applied Physics*, 53 1649 (1982).
- [4] W. Grünberger, D. Hinz, A. Kirchner, K.H. Müller, L. Schultz, *Journal of Alloys and Compounds*, 257, 293 (1997).
- [5] R.K. Mishra, T.Y. Chu, L.K. Rabenberg, *Journal of Magnetism and Magnetic Materials*, 84, 88 (1990).
- [6] R.K. Mishra, *J. Mater. Eng.* 11, 87 (1989).
- [7] R.K. Mishra, R.W. Lee, *Applied Physics Letter*, 48, 733 (1986).
- [8] V.V. Volkov, Y. Zhu, *Journal of Applied Physics*, 85, 3254 (1999).
- [9] L.H. Lewis, Y. Zhu, D.O. Welch, *Journal of Applied Physics*, 76, 6235 (1994).
- [10] T.D. Nguyen, K.M. Krishnan, L.H. Lewis, Y. Zhu, D.O. Welch, *Journal of Applied Physics*, 79, 4848 (1996).
- [11] O. Gutfleisch, D. Eckert, R. Schäfer, K.H. Müller, V. Panchanathan, *Journal of Applied Physics*, 87, 6119 (2000).
- [12] M. Gronefeld, H. Kronmüller, *Journal of Magnetism and Magnetic Materials*, 88, L267 (1990).
- [13] Y. Q. Wu, T. Bitoh, K. Hono, A. Makino, A. Inoue, *Acta Materialia* 49, 4069 (2001).
- [14] T.Y. Chu, L. Rabenberg, R.K. Mishra, *Journal of Applied Physics*, 69, 6046 (1991).
- [15] H. Sepehri-Amin, T. Ohkubo, T. Shima, K. Hono, *Acta Materialia*, 60, 819 (2012).
- [16] H. Sepehri-Amin, D. Prabhu, M. Hayashi, T. Ohkubo, K. Hioki, A. Hattori, K. Hono, *Scripta Materialia*, 68, 167 (2013).
- [17] T. Mouri, M. Kumano, H.Y. Yasuda, T. Nagase, T. Kato, Y. Nakazawa, H. Shimizu, *Scripta Materialia*, 78, 37 (2014).

## Chapter 6. Microstructure study of Nd-Fe-B thin films with different levels of coercivity

### 6.1 Introduction

How the morphology of the platelet  $\text{Nd}_2\text{Fe}_{14}\text{B}$  grains develops and chemical composition of the intergranular phase changes in the hot-deformed Nd-Fe-B magnets in each stage were studied in the Chapter 5. It is found that the enrichment of rare-earth element shows an anisotropic behavior at the intergranular phase, i.e. a higher concentration of rare-earth elements in the intergranular (c IGF) phases parallel to the flat surface of platelet shaped  $\text{Nd}_2\text{Fe}_{14}\text{B}$  grains compared to that of intergranular phases (a IGF) at the short side of platelets. Therefore, the dominant coercivity mechanism might be the nucleation of the reversed domains in the Fe-rich intergranular region with reduced anisotropy, as suggested by Lewis et al [1]. Even though there are pinning effects from the grain boundaries, the pinning field should be lower than the nucleation field due to the existence of high amount of Fe as shown in Figure 4.2b. It is though that the grain boundary diffusion process could make the grain boundary uniform non-ferromagnetic. Unfortunately, only c IGF becomes a non-ferromagnetic thick GB while a IGF still contains high amount of ferromagnetic elements in the GBDP Nd-Fe-B magnets as shown in Figure 6.1 [2]. The other evidence is the finding of the expansion of the GBDP Nd-Fe-B magnets along the c-axis direction, which suggests much more Nd diffused into the intergranular phases parallel to the flat surface of platelet shaped  $\text{Nd}_2\text{Fe}_{14}\text{B}$  grains [3]. Recently, a so-called Nd-Cu eutectic diffusion under expansion constraint was developed to optimize the volume fraction of Nd-rich intergranular layer and the diffused magnets exhibit a coercivity of  $\sim 2.0$  T, remanence of 1.36 T, and  $(\text{BH})_{\text{max}}$  of  $358 \text{ kJm}^{-3}$  at room temperature [4]. Even though  $(\text{BH})_{\text{max}}$  of this diffused magnets was reported to outperform the 4% Dy-containing sintered magnets at  $200 \text{ }^\circ\text{C}$ , this coercivity value is still lower than the ultimate goal 3 T, which seems a barrier for the bulk Dy-free Nd-Fe-B magnets. The study of the modeled microstructure may provide some clues to leap over the barrier.

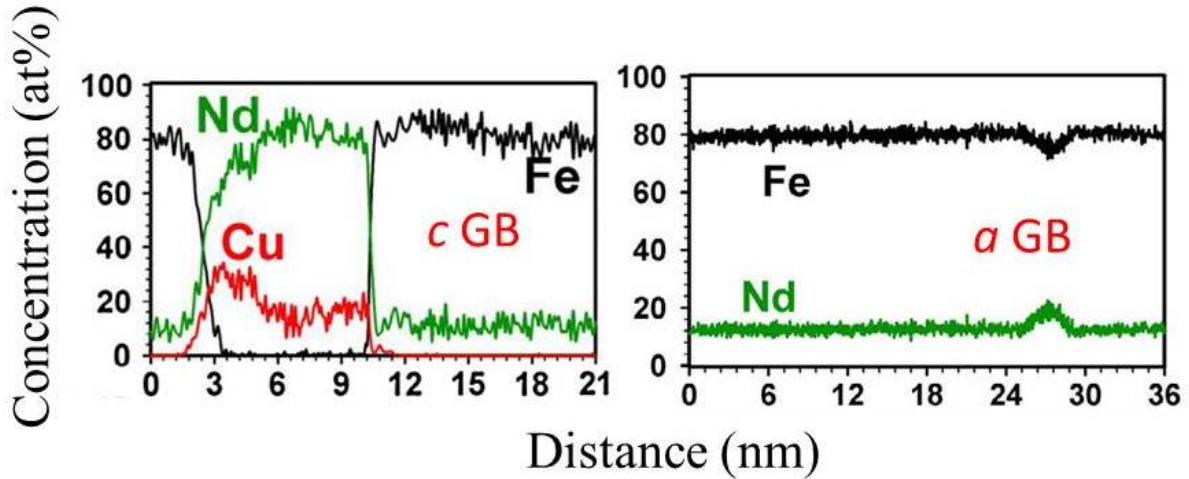


Figure 6.1 Composition profiles of c IGF and a IGF from the grain boundary diffusion processed Nd-Fe-B magnets [2].

Considering the microstructure of the thin film can be easily controlled, thin film fabrication technique is a powerful tool to study the relationship of microstructure and coercivity by creating models for the bulk Nd-Fe-B magnets. Recently, an ideal microstructure model that the elongated single domain sized  $\text{Nd}_2\text{Fe}_{14}\text{B}$  grains was magnetically isolated by the diffusion process of Nd-Ag capping layer was realized in the thin film and the coercivity was reported to be as high as 2.95 T [5]. Compared with the relatively low coercivity of the bulk Nd-Fe-B magnets, this report suggests that there is much room for the coercivity enhancement in the bulk magnets via optimizing the microstructure [6]. Therefore, the aim of this work is to establish the microstructure feature required for high coercivity of 3.0 T by comparing the microstructure of Nd-Fe-B thin films with different levels of coercivity and serve in the development of Dy-free bulk Nd-Fe-B magnets.

## 6.2 Experiment

The samples were prepared by using an ultrahigh vacuum compatible magnetron sputtering system. The base pressure is below  $5 \times 10^{-8}$  Pa, and the Ar gas pressure was kept at 1.3 Pa during deposition. The composition of the Nd-Fe-B layer was controlled by co-sputtering with Fe,  $\text{Fe}_{80}\text{B}_{20}$  (at. %), and Nd targets. First of all, a Mo buffer layer of 20 nm was deposited onto MgO (100) single crystal substrates at room temperature (R.T.), then the samples were annealed at 750 °C for 30 min for the promotion of the epitaxial growth of Mo buffer layer. Subsequently, the substrates were cooled down to

500 °C and the Nd-Fe-B layer and the Nd-Cu cap layer were deposited. In order to see the effect of film thickness, the nominal thickness of the Nd-Fe-B layer ( $t_{\text{Nd-Fe-B}}$  nm) was selected as 16 and 100 nm, while the thickness of Nd-Cu layer ( $t_{\text{Nd-Cu}}$  nm) was selected as 0, 0.75 and 4.7 nm, respectively. After the deposition of both Nd-Fe-B and Nd-Cu layers, the samples were annealed at 550 °C for 60 min. Finally, a Mo layer of 10 nm was deposited at R.T. for the prevention of oxidation. The stack structure was shown in Figure 6.2. The structural analysis was performed by X-ray diffraction (XRD) with Cu K $\alpha$  radiation. The magnetization curves were measured using a superconducting quantum interference device (SQUID) magnetometer in the field up to  $\pm 70$  kOe at R.T. The microstructure of the films was characterized by transmission electron microscopy (TEM; FEI Titan G2 80-200 operating at 200 kV) with energy dispersive X-ray spectroscopy (EDS). TEM specimens were prepared by focused ion beam (FIB; FEI Helios NanoLab 650).

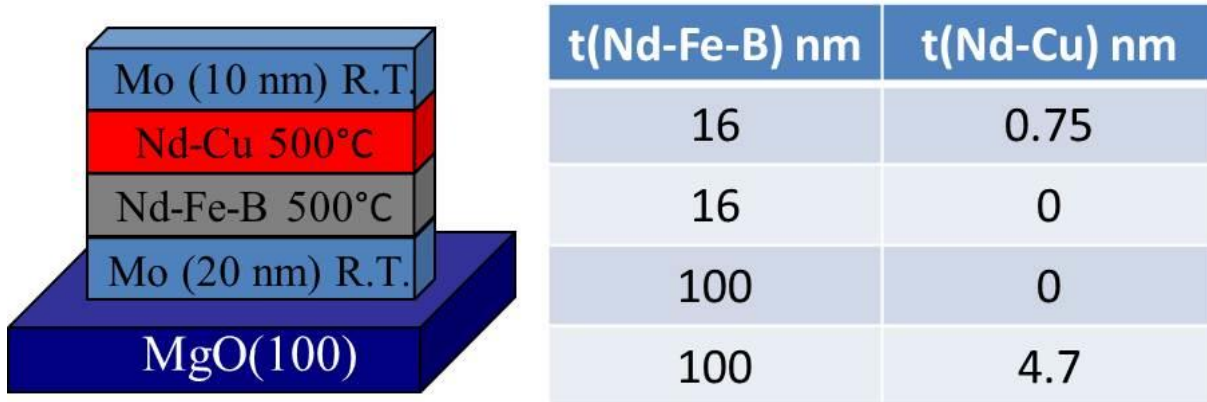


Figure 6.2 The stack structure and thickness information of Nd-Fe-B and Nd-Cu layers.

### 6.3 Results

Figures 6.3a-d show the magnetization curves of the Nd-Fe-B films with different levels of coercivity. A high coercivity of  $\sim 3.06$  T was obtained in the Nd-Fe-B film of 16 nm with Nd-Cu capping layer of 0.75 nm as shown in Figure 6.3a. This coercivity value is the highest one reported in the field of Dy-free Nd-Fe-B films and bulk magnets [6]. Without the Nd-Cu capping layer, the coercivity dropped to a level of  $\sim 1.90$  T in the NdFeB16 film (Figure 6.3b). Note that the initial magnetization curves of these two films show a two-step behavior, indicating the existence of the pinning sites and it is clear that the depinning field of NdFeB16/NdCu0.75 is much higher than that of NdFeB16. When the Nd-Fe-B layer

was increased to 100 nm, the coercivity decreased to 0.96 T in the NdFeB100 film (Figure 6.3c). To keep the thickness ratio of Nd-Fe-B and Nd-Cu layer constant with NdFeB16/NdCu0.75, a Nd-Cu capping layer of 4.7 nm was sputtered onto Nd-Fe-B layer of 100 nm. However, the coercivity dropped to ~0.2 T unexpectedly (Figure 6.3d). Note that the initial magnetization curves of the latter two films are saturated easily at relatively low external fields.

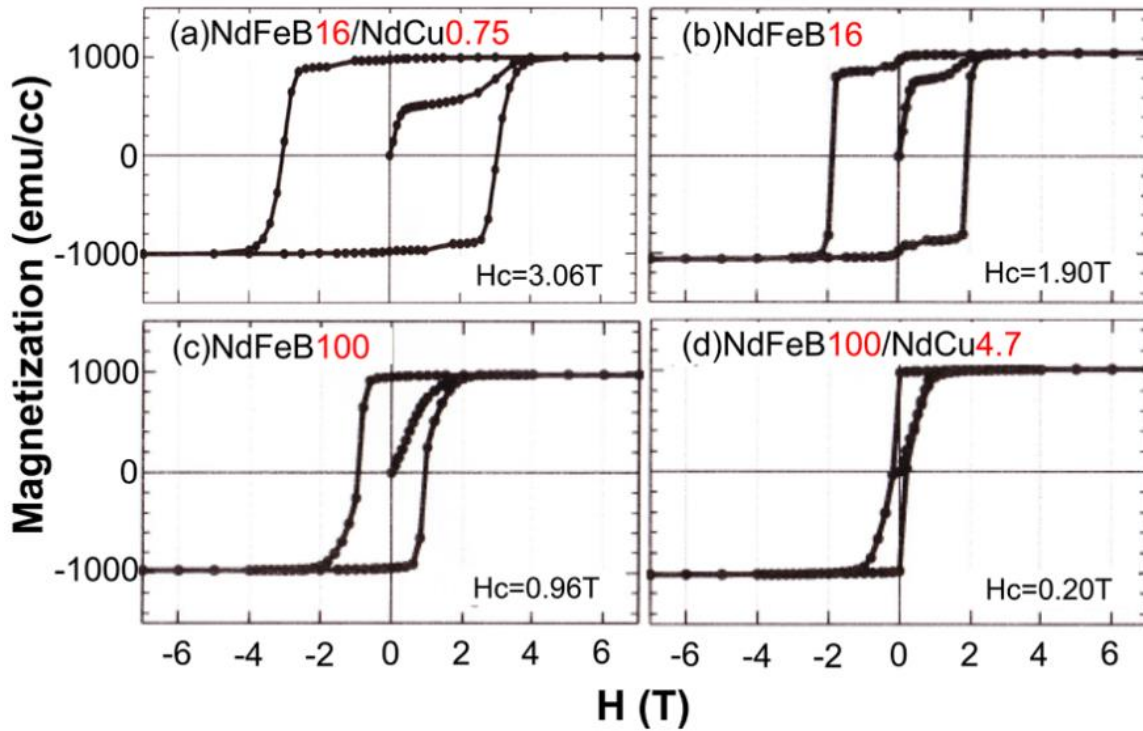


Figure 6.3 Magnetization curves of the Nd-Fe-B films of (a) NdFeB16/NdCu0.75, (b) NdFeB16, (c) NdFeB100, and (d) NdFeB100/NdCu4.7.

Figure 6.4 shows the cross-sectional bright field TEM images of the Nd-Fe-B films. The two thinner films show a single Nd-Fe-B layer comprising platelet shaped grains (Figures 6.4a-b). The grain size was  $\sim 53 \pm 8$  nm, which is much smaller than the single domain size of  $\text{Nd}_2\text{Fe}_{14}\text{B}$  grains [7]. When the thickness of Nd-Fe-B layer was increased to 100 nm, the grains piled up irregularly as shown in Figures 6.4c-d. The shape of grains varied from platelet to column, and even irregular shape due to the constraint from neighboring grains. The grains became coarsened in both lateral and vertical directions and the grain size was ranged from 80 to 130 nm.

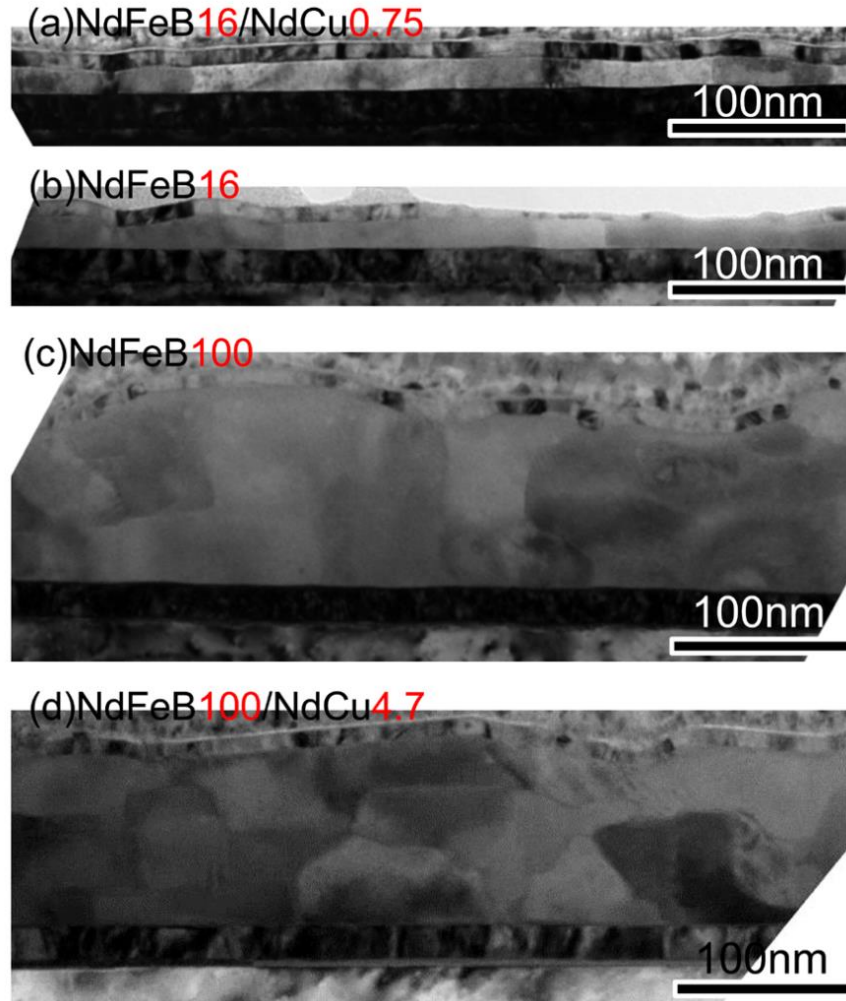


Figure 6.4 Cross-sectional bright field TEM images of the Nd-Fe-B films of (a) NdFeB<sub>16</sub>/NdCu<sub>0.75</sub>, (b) NdFeB<sub>16</sub>, (c) NdFeB<sub>100</sub>, and (d) NdFeB<sub>100</sub>/NdCu<sub>4.7</sub>.

Figure 6.5 shows the STEM-EDS analyses of NdFeB<sub>16</sub>/NdCu<sub>0.75</sub> and NdFeB<sub>16</sub> films. In the HAADF images, we can observe a single layer of platelet anisotropic grains. The selected peaks in the EDS spectrum for elemental mappings are Fe-K, Nd-L and Cu-K. Comparing the elemental mappings of the two films, we can clearly see Fe was depleted and Nd was enriched at the GBs in the NdFeB<sub>16</sub>/NdCu<sub>0.75</sub> film, while the GBs were hard to discern from Fe and Nd mappings in the NdFeB<sub>16</sub> film. Cu was also enriched at the GB phase in the NdFeB<sub>16</sub>/NdCu<sub>0.75</sub> film. The formation of the platelet Nd<sub>2</sub>Fe<sub>14</sub>B grains isolated by Nd-rich GBs in the single layer film leads to the enhanced coercivity at the level of 3.0 T.

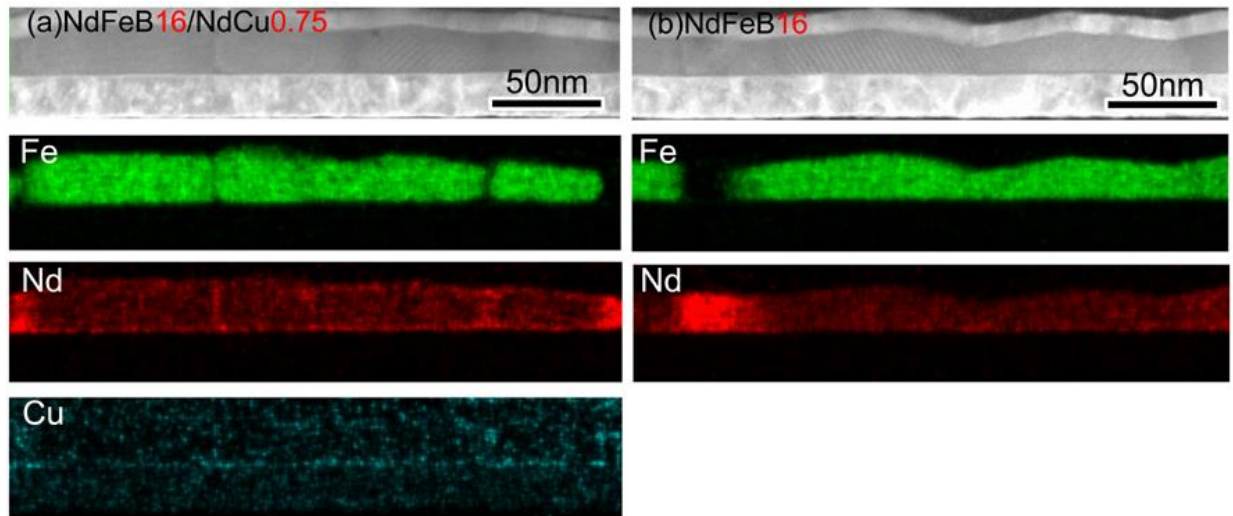


Figure 6.5 Cross-sectional STEM-EDS elemental mapping images of (a) NdFeB16/NdCu0.75 film and (b) NdFeB16 film.

Figures 6.6a-b show the cross-sectional STEM-EDS images of NdFeB100 and NdFeB100/NdCu4.7 films, respectively. The multilayer  $\text{Nd}_2\text{Fe}_{14}\text{B}$  grains with irregular shape corners can be observed in the HAADF images of the two films. These irregular shape corners caused large local stray fields and resulted in the decrease in the coercivity. Elemental mappings for Fe-K, Nd-L and Cu-K taken from the same region of the two films are shown below the HAADF images. The EDS mappings show that except the segregation of Nd-rich grains, there was no clear Nd enrichment at the GB phase in the two films. High magnification Fe mappings revealed part of thin GBs in the NdFeB100 film from the depletion of Fe (Figure 6.6c) while there were no clear trace from GBs in the NdFeB100/NdCu4.7 film (Figure 6.6d). Therefore, the  $\text{Nd}_2\text{Fe}_{14}\text{B}$  grains in the NdFeB100/NdCu4.7 film were much poorer isolated, which led to a much lower coercivity.

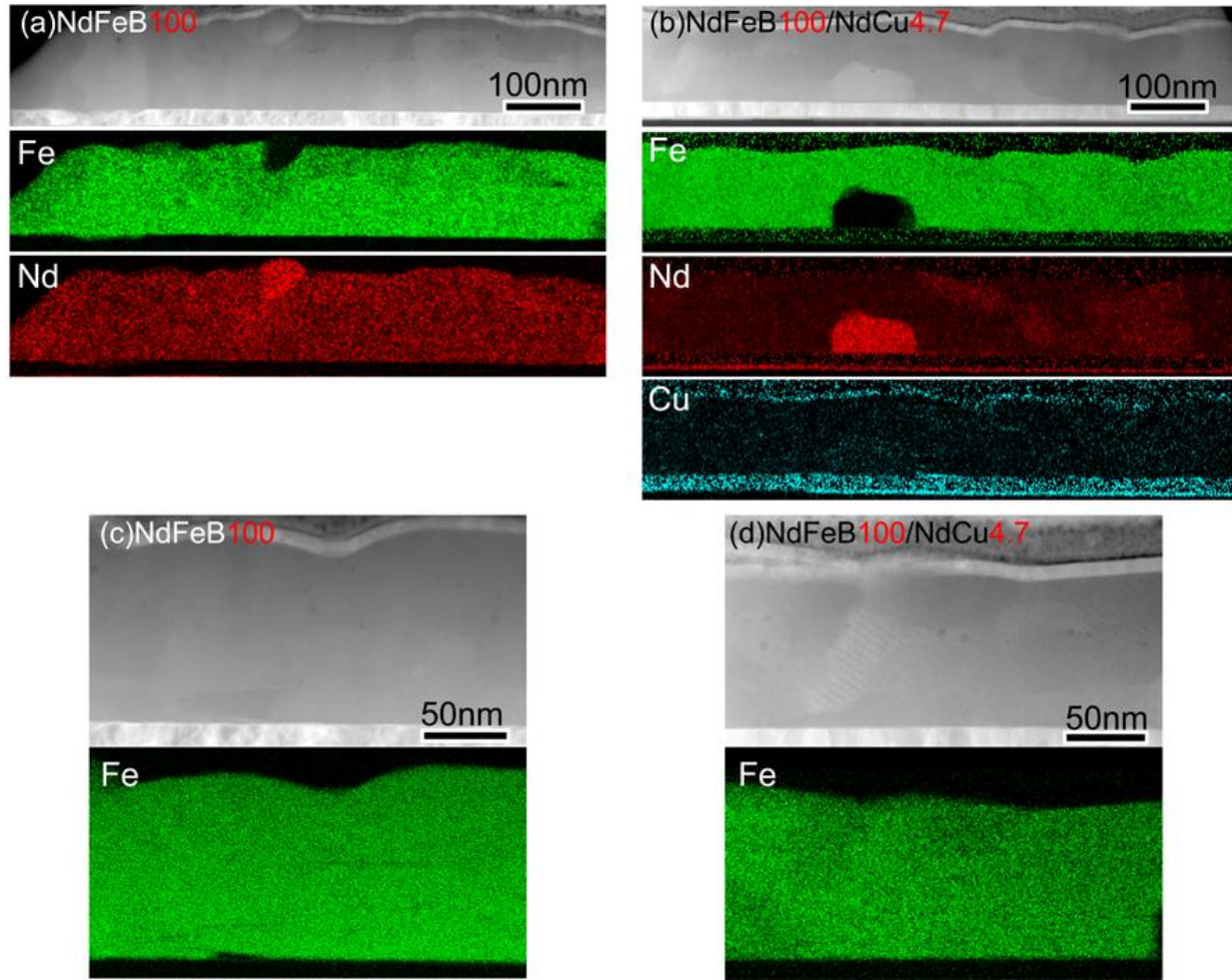


Figure 6.6 Cross-sectional low magnification STEM-EDS elemental mapping images of (a) NdFeB100 film and (b) NdFeB100/NdCu4.7 film, high magnification images of (c) NdFeB100 film and (d) NdFeB100/NdCu4.7 film.

## 6.4 Discussion

To describe how the coercivity performs at the elevated temperature, the temperature dependence of the coercivity ( $\beta$ ) of these films was shown in Figure 6.7a. The definition of  $\beta$  is as follows:

$$\beta = [H_c(T) - H_c(300)] / [H_c(300) * (T-300)] * 100\%, \quad (6.1)$$

where  $H_c(T)$  and  $H_c(300)$  are the coercivity measured at temperature  $T$  and room temperature 300 K, respectively. The calculated values of  $\beta$  for different Nd-Fe-B thin films are shown in Figure 6.7. The thermal stability of coercivity of the thinner films is much better than that of thicker ones, indicating the coercivity can maintain a relatively high value in the thinner films at the elevated temperature. The

absolute value of  $\beta$  of NdFeB16 film (-0.39 %/K) was slightly lower than that of NdFeB16/NdCu0.75 film (-0.42 %/K) unexpectedly. Note that these values are much lower than that of commercial sintered Nd-Fe-B magnets, typical around -0.6 %/K, because of very small grain size in the thin films.

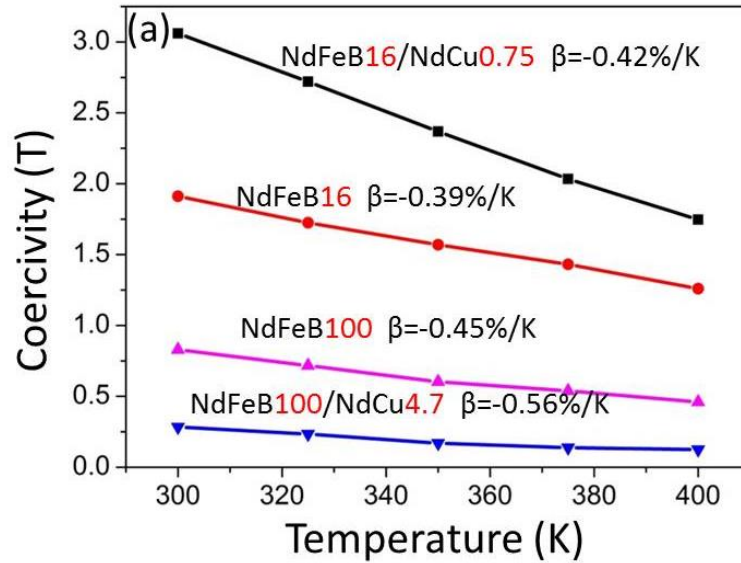


Figure 6.7 Temperature dependence of the coercivity of the Nd-Fe-B films with different levels of coercivity.

This work investigated the microstructure of the Nd-Fe-B thin films with different levels of coercivity, which could be used as a model for achieving high coercivity in the bulk Nd-Fe-B magnets, especially for hot-deformed ones, because of their similar grain feature. Lack of the continuous Nd-rich GBs leads to a relatively low coercivity in NdFeB100 thin film. This simply resembles the as-hot-deformed Nd-Fe-B magnets, in which the GBs are enriched with Fe and show ferromagnetic feature and the typical coercivity level is around 1.0~1.3 T [8]. The NdFeB16 film only consists of a single layer of the platelet Nd<sub>2</sub>Fe<sub>14</sub>B grains. The effect of the exchange coupling from vertical direction can be ignored. Due to the lack of clear Nd-rich GBs between the lateral neighboring grains, the coercivity only reaches to 1.9 T. This is similar to the Nd/Cu diffused hot-deformed Nd-Fe-B magnets. After diffusion process, the thick GBs more than 3 nm with high amount of Nd enrichment appear along the broad surface of Nd<sub>2</sub>Fe<sub>14</sub>B grains while the GBs locating at the short side of platelet grains is much thinner and highly enriched with Fe and Co [2]. This microstructure can be regarded as that it was comprised by a lot of film structure like NdFeB16. Therefore, the coercivity level is expected to be around 2.0~2.5 T. The

composition difference at different types of GBs is attributed to the anisotropic segregation of rare-earth element during the hot-deformation process and it also happens in the diffusion process considering the obvious expansion along *c*-axis of the diffused hot-deformed Nd-Fe-B magnets [3,4]. A high coercivity of 3.06 T is achieved in the NdFeB16/NdCu0.75 film, in which a single layer of the platelet Nd<sub>2</sub>Fe<sub>14</sub>B grains are isolated by Nd-rich GBs. In such a case, the exchange coupling from both vertical and lateral directions is substantially suppressed. It demonstrates that the coercivity level higher than 3 T is achievable without using heavy rare-earth element if the single-domain-sized grains are completely magnetically isolated. To realize the coercivity of 3 T in the hot-deformed Nd-Fe-B magnets, how to isolate the grains between the short sides of platelet grains is a crucial issue. Another one is the non-aligned coarse Nd<sub>2</sub>Fe<sub>14</sub>B grains at the interface between the original flakes. A recent investigation on the two-stage deformation of the hot-deformed Nd-Fe-B magnets have shown that the suppression of the formation of non-aligned coarse Nd<sub>2</sub>Fe<sub>14</sub>B grains and the reduction in the grain size by a pre-straining process prior to the hot-deformation effectively enhanced the coercivity and texture of the hot-deformed Nd-Fe-B magnets [9].

## 6.5 Summary

This work compared the microstructure of the Nd-Fe-B thin films with different levels of coercivity and established the microstructure feature required for the coercivity of high than 3 T for the bulk hot-deformed Nd-Fe-B magnets. A high coercivity of 3.06 T was firstly reported using the Nd-Fe-B thin films without the heavy rare-earth element. A thin single layer of the platelet Nd<sub>2</sub>Fe<sub>14</sub>B grains were well isolated by Nd-rich GBs after the diffusion of a Nd-Cu layer. This microstructure significantly reduced the exchange coupling between neighboring grains from both vertical and lateral directions.

## 6.6 Extension

The addition of Al is known to lower the melting temperature of the Nd-rich phase and improve the wetting ability of the liquid phase during the processing [10-11]. The substitution of slight amount of Al for Fe is also reported to increase the anisotropy fields [12]. Based on these advantages, an Al layer ~0.6 nm was deposited on the Nd-Cu layer in the NdFeB16/NdCu0.75 film as shown in Figure 6.8(a). The NdFeB16/NdCu0.75/Al0.6 film shows a coercivity value as high as 3.15 T (Figure 6.8(b)). The planview observation from the Fe elemental mapping in Figure 6.8(c) shows the grain size is ~25 nm. The

cross-sectional STEM-EDS elemental mapping images (Figure 6.8(d)) clearly show that the individual  $\text{Nd}_2\text{Fe}_{14}\text{B}$  grain is well isolated by a (Nd,Cu)-rich the grain boundary phase. The behavior of Al is not discernable at this magnification due to its very low content.

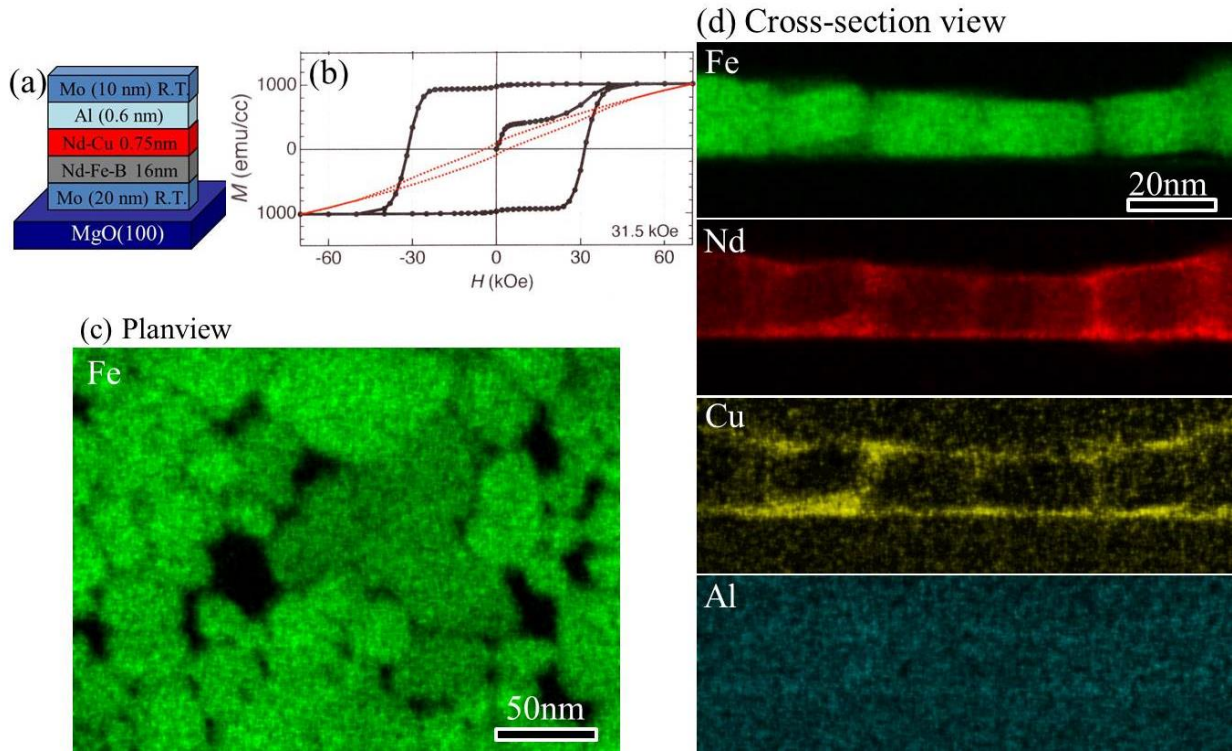


Figure 6.8 (a) The stack structure of the Nd-Fe-B thin film with Nd-Cu and Al layers. (b) Magnetization curve of the  $\text{NdFeB}_{16}/\text{NdCu}_{0.75}/\text{Al}_{0.6}$  film. (c) Planview and (d) cross-sectional STEM-EDS elemental mapping images of the  $\text{NdFeB}_{16}/\text{NdCu}_{0.75}/\text{Al}_{0.6}$  film.

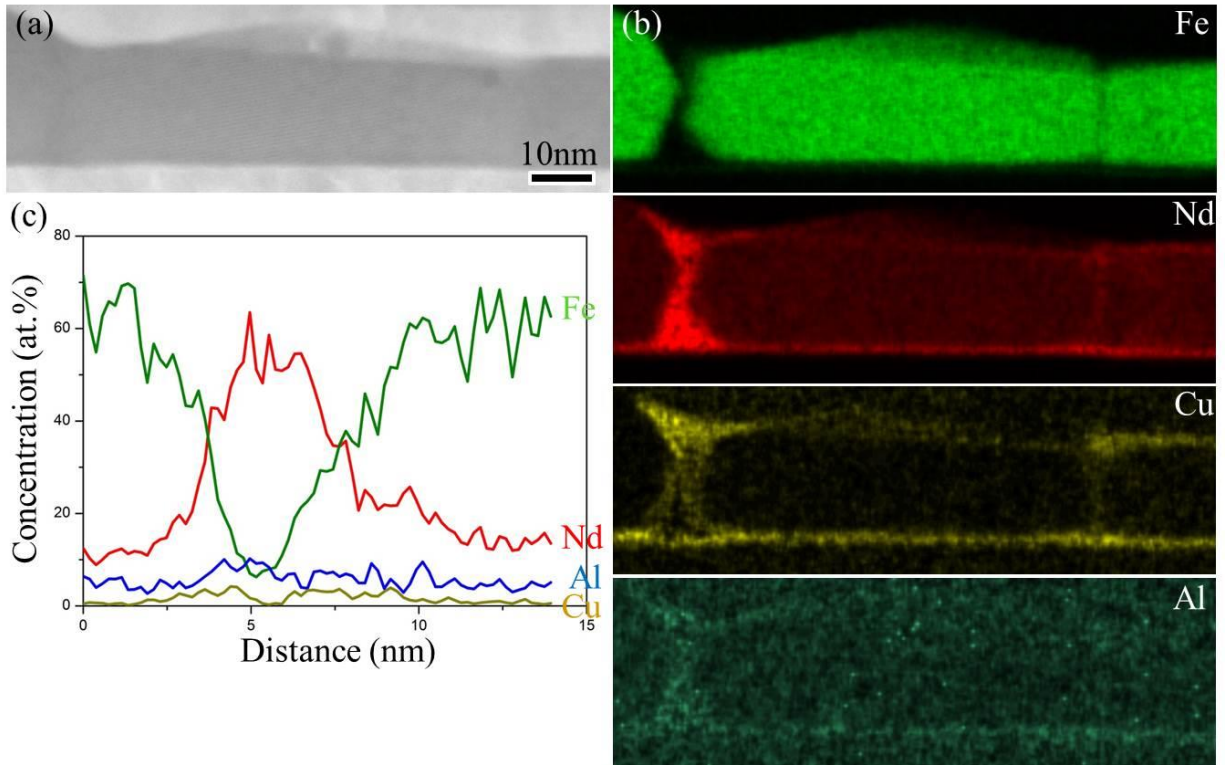


Figure 6.9 (a) High magnification HAADF-STEM image and (b) EDS elemental mapping images of the NdFeB<sub>16</sub>/NdCu<sub>0.75</sub>/Al<sub>0.6</sub> film. (c) Composition profile of the grain boundary calculated from the EDS analysis.

The high magnification HAADF-STEM images and the composition profile from the grain boundary are shown in Figure 6.9. It can be seen that a thick Nd-rich grain boundary phase separates the neighboring grains. Cu was found to be present at the interface between the Nd<sub>2</sub>Fe<sub>14</sub>B grains and the grain boundary phase. Al shows clear enrichment at the grain boundary phase and a very low content at the Nd<sub>2</sub>Fe<sub>14</sub>B phase. Composition profile of the grain boundary shows the nonferromagnetic elements Nd and Al are high enriched and Fe is almost depleted at the grain boundary phase. So the grain boundary should be nonferromagnetic phase. The improved isolation of the individual Nd<sub>2</sub>Fe<sub>14</sub>B grain and improved intrinsic property of the Nd<sub>2</sub>Fe<sub>14</sub>B phase by slight substitution of Al for Fe in the single layer of Nd-Fe-B film enhanced the coercivity further.

## Reference

- [1] L.H. Lewis, Y. Zhu, D.O. Welch, *Journal of Applied Physics*, 76, 6235 (1994).
- [2] H. Sepehri-Amin, T. Ohkubo, S. Nagashima, M. Yano, T. Shoji, A. Kato, T. Schrefl, K. Hono, *Acta Materialia*, 61, 6622 (2013).
- [3] T. Akiya, J. Liu, H. Sepehri-Amin, T. Ohkubo, K. Hioki, A. Hattori, K. Hono, *Journal of Applied Physics*, 115 17A766 (2014).
- [4] T. Akiya, J. Liu, H. Sepehri-Amin, T. Ohkubo, K. Hioki, A. Hattori, K. Hono, *Scripta Materialia*, 48, 81 (2014).
- [5] W.B. Cui, Y.K. Takahashi, K. Hono, *Acta Materialia*, 59, 7768 (2011).
- [6] K. Hono, H. Sepehri-Amin, *Scripta Materialia*, 67, 530 (2012).
- [7] J.D. Livingston, *Journal of Applied Physics*, 57, 4137 (1985).
- [8] J. Liu, H. Sepehri-Amin, T. Ohkubo, K. Hioki, A. Hattori, T. Schrefl, K. Hono, *Acta Materialia*, 61, 5387 (2013).
- [9] T. Mouri, M. Kumano, H.Y. Yasuda, T. Nagase, T. Kato, Y. Nakazawa, H. Shimizu, *Scripta Materialia*, 78, 37 (2014).
- [10] K.G. Knoch, G. Schneider, J. Fidler, E.T. Henig, H. Kronmüller, *IEEE Transactions on Magnetics* 25, 3426 (1989).
- [11] L. Legras, J. Delmare, D. Lemarchand, J. Vu Dinh, P. Vigier, *Journal of Alloys and Compounds*, 218, 17 (1995).
- [12] E. Burzo, *Reports on Progress in Physics*, 61, 1099 (1998).

## Chapter 7. Summary of the thesis

The thesis aims to investigate the microstructure and coercivity relationship of the hot-deformed Nd-Fe-B permanent magnets to give a guideline for the development of Dy-free Nd-Fe-B magnets with high coercivity and high remanence for the applications of hybrid electrical vehicles, wind power generators, and electric power compressor motors by conducting detailed microstructure characterizations in multiscale dimensions. For this purpose, we have employed micromagnetic simulations and various advanced materials characterization techniques, including scanning electron microscope, transmission electron microscope, and three dimensional atom probe.

Multiscale characterization results in Chapter 3 have shown that the effect of increasing Nd content in the hot-deformed Nd-Fe-B magnets is to form a distinct Nd-rich phase at the grain boundary, and this grain boundary phase containing high amount of nonmagnetic elements Nd can effectively weaken the exchange coupling between the neighboring hard magnetic  $\text{Nd}_2\text{Fe}_{14}\text{B}$  grains. Micromagnetic simulations demonstrate that the non-ferromagnetic grain boundary can prevent the nucleation of reversed domains at a low magnetic field and hinder the propagation of the reversed magnetic domain walls to the neighboring grains which are both contributing to the coercivity enhancement.

Chapter 4 investigates another important factor affecting coercivity, that is, grain size. The Nd-rich intergranular phases distribute uniformly in the fine-grained sample processed at low temperature, while the large Nd-rich triple junction phases are more frequently observed in the sample at a higher temperature. Micromagnetic simulations showed that the reduction in grain size decreased the demagnetizing field, leading to the increase in coercivity and the improvement of the temperature dependence of the coercivity.

The study of microstructure evolution of hot-deformed Nd-Fe-B magnets in Chapter 5 provides some hints to improve the coercivity further, i.e. the hard magnetic  $\text{Nd}_2\text{Fe}_{14}\text{B}$  grains should be isolated by a uniform grain boundary phase both in morphology and chemical composition. But the approach to realize it is still under exploring.

Chapter 6 demonstrates a coercivity of more than 3.0 T can be achieved in the Dy-free Nd-Fe-B magnets by using a thin film modeled structure if the hard magnetic  $\text{Nd}_2\text{Fe}_{14}\text{B}$  grains are completely magnetically isolated.

## Publications

1. J. Liu, H. Sepehri-Amin, T. Ohkubo, K. Hioki, A. Hattori, T. Schrefl, K. Hono, “Grain size dependence of coercivity of hot-deformed Nd-Fe-B anisotropic magnets”, *Acta Materialia*, 82, 336-343 (2015).
2. J. Liu, H. Sepehri-Amin, T. Ohkubo, K. Hioki, A. Hattori, K. Hono, “Microstructure evolution of hot-deformed Nd-Fe-B anisotropic magnets”, *Journal of Applied Physics*, 115, 17A744 (2014).
3. J. Liu, H. Sepehri-Amin, T. Ohkubo, K. Hioki, A. Hattori, T. Schrefl, K. Hono, “Effect of Nd content on the microstructure and coercivity of hot-deformed Nd-Fe-B permanent magnets”, *Acta Materialia*, 61, 5387 (2013).
4. Hwachol Lee, Hiroaki Sukegawa, Jun Liu, Tadakatsu Ohkubo, Shinya Kasai, Seiji Mitani, and Kazuhiro Hono, “Ferromagnetic MnGaN<sub>1-x</sub> thin films with perpendicular magnetic anisotropy for spintronics applications”, submitted.
5. T. Akiya, J. Liu, H. Sepehri-Amin, T. Ohkubo, K. Hioki, A. Hattori, K. Hono, “High-coercivity hot-deformed Nd-Fe-B permanent magnets processed by Nd-Cu eutectic diffusion under expansion constraint”, *Scripta Materialia*, 81, 48 (2014).
6. T. Akiya, J. Liu, H. Sepehri-Amin, T. Ohkubo, K. Hioki, A. Hattori, K. Hono, “Low temperature diffusion process using rare earth-Cu eutectic alloys for hot-deformed Nd-Fe-B bulk magnets”, *Journal of Applied Physics*, 115, 17A766 (2014)
7. H. Sepehri-Amin, J. Liu, T. Ohkubo, K. Hioki, A. Hattori, K. Hono, “Enhancement of coercivity of hot-deformed Nd-Fe-B anisotropic magnet by low-temperature grain boundary diffusion of Nd<sub>60</sub>Dy<sub>20</sub>Cu<sub>20</sub> eutectic alloy”, *Scripta Materialia*, 69, 647 (2013).

## Acknowledgements

First and foremost, I would like to express my sincerest appreciation to my advisor, Professor Kazuhiro Hono, for giving me the opportunity to pursue my research in Magnetic Materials Unit, National Institute for Materials Science, and continually giving me valuable advice and interesting projects.

I am especially grateful to Professor Tadakatsu Ohkubo, who has taught me many experimental techniques generously and given me helpful suggestions.

I would like to thank Dr. Atsushi Hattori and Dr. Keiko Hioki from Daido Steel, and Professor Toshiyuku Shima from Tohoku Gakuin University for providing the interesting samples and having useful discussions.

I express my deep gratitude to Dr. Sepehri Amin Hossein, Dr. Weibin Cui, Dr. Masaya Kodzuka, and Dr. Yimen Chen for their valuable advice and meaningful discussions in the coercivity mechanism and atom probe data analysis.

I sincerely thank my friends and colleagues for making my research life smooth and pleasure.

I would like to acknowledge the Graduate Research Assistantship of National Institute for Materials Science for providing me the financial support during my degree candidature.

Many thanks to my wife, Jie Chen, for her patience, consideration and encouragement, and my little princess, Yuchen Liu, for the happiness and hope. Finally, I would like to express my deepest gratitude to my mother, who makes many sacrifices and continuously gives me support and encouragement on the way to pursue my dream.